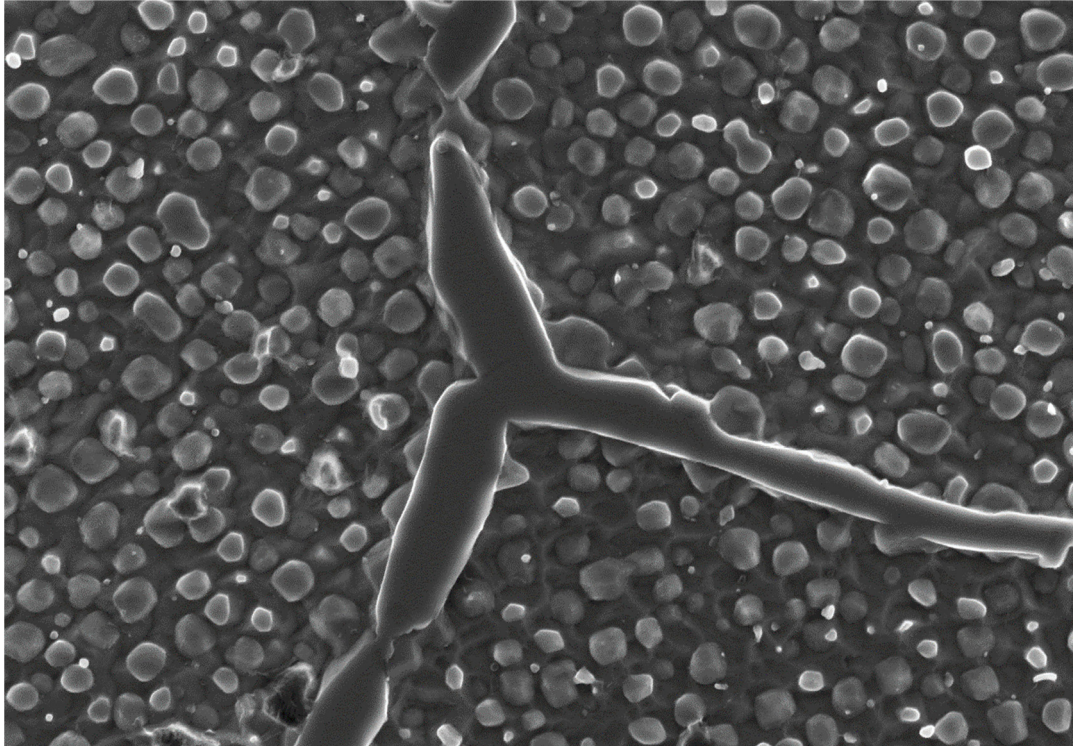




CHALMERS



Development of a γ' Precipitation Hardening Ni-Base Superalloy for Additive Manufacturing

Abdul Shaafi Shaikh

Department of Industrial and Materials Science
CHALMERS UNIVERSITY OF TECHNOLOGY
Gothenburg, Sweden 2018

Development of a γ' Precipitation Hardening Nickel-Base Superalloy for Additive Manufacturing

ABDUL SHAAFI SHAIKH

© Abdul Shaafi Shaikh, 2018

Department of Industrial and Materials Science
Chalmers University of Technology
SE-412 96 Gothenburg
Sweden
Telephone + 46 (0)31-772 1000

Thesis was performed in the framework of the Centre for Additive Manufacturing – Metal (CAM²) in collaboration with EOS Finland Oy.

Cover image:

[Grain_boundary_triple_point_in_heat_treated_IN939_showing_carbides_and_gamma_prime]

Printed by Chalmers Reproservice

Gothenburg, Sweden, 2018.

Development of a γ' Precipitation Hardening Nickel-Base Superalloy for Additive Manufacturing

ABDUL SHAAFI SHAIKH

Department of Industrial and Materials Science
Chalmers University of Technology

Abstract

The performance of superalloy materials at high temperatures is what makes gas turbine technology possible. Continual improvement in superalloy properties and resultant elevation of operating temperatures drives higher efficiency and reduced environmental impact in both aerospace and energy applications. Given the technological and commercial significance of superalloys, their adoption into Additive Manufacturing is of vital importance.

The Additive Manufacturing of nickel-base superalloys aims to optimize function through geometric complexity of engineered parts, while reducing product development and marketing times. However, there are challenges to overcome before these materials can be used in serial production. Most superalloys are susceptible to cracking when processed in laser-powder bed fusion processes, and cracking mechanisms must be understood and mitigated in order to produce fully-dense parts. Another challenge is in the post-processing stage. Additively manufactured microstructures are unlike cast or wrought microstructures, and heat treatment regimens must be re-formulated based on the different starting microstructure.

Inconel 939 is a cast Ni-base superalloy for service above 800°C and is widely used in hot-sections of industrial gas turbine engines. This thesis presents a study of the cracking behaviour of IN939, and based on fractographic results, shows solidification cracking to be the primary mechanism responsible. The design of heat-treatment necessitated a comprehensive study of the starting microstructure. This was performed by thermal analysis and metallography and equated to simulation results. Heat treatment trials were conducted and the resulting microstructure and room temperature mechanical properties were characterized. Results showed significant differences in the fractions and morphologies of strengthening phases, compared to the conventionally cast material, while room temperature mechanical properties were better or comparable. The obtained results form a basis for proceeding with high-temperature and creep testing of the material to prove its viability in AM.

Keywords: Nickel-base superalloy, cracking, IN939, additive manufacturing, DMLS, laser sintering, laser melting, laser powder bed fusion, heat treatment, microstructural evaluation.

Preface

This thesis work was performed partly at the Department of Industrial and Materials Science, Chalmers University of Technology, Gothenburg, Sweden, and partly at Electro Optical Systems Finland Oy, Turku. I am grateful to all my colleagues and collaborators in both organisations for their assistance and encouragement. Special thanks are due to Kevin Minet and Dr. Eduard Hryha for their supervision and enthusiastic involvement throughout this project.

A. Shaafi Shaikh

Turku, June 2018

“Nickel superalloy metallurgy is showing significant scientific enlightenment after years of existence as an art.”

- *Earl W. Ross and Chester T. Sims, Ch 4, Superalloys II, 1987*

Abbreviations and Symbols

FCC = Face-centered-cubic

VAR = Vacuum Arc Remelting

VIM = Vacuum Induction Melting

DMLS = Direct Metal Laser Sintering

TCP = Topologically Close-Packed

FOD / DOD = Foreign Object Damage / Domestic Object Damage

LMD = Laser Metal Deposition

RT = Room Temperature

AM = Additive Manufacturing

RP = Rapid Prototyping

PBF = Powder Bed Fusion

L-PBF = Laser Powder Bed Fusion

EB-PBF = Electron Beam Powder Bed Fusion

VIGA = Vacuum Inert Gas Atomization

EIGA = Electrode Induction Gas Atomization

EOS = Electro Optical Systems GmbH

BSE = Back-Scattered Electron

HIP = Hot Isostatic Pressing

TIG = Tungsten Inert Gas

HAZ = Heat Affected Zone

SAC = Strain-Age Cracking

DDC = Ductility Dip Cracking

TEM = Transmission Electron Microscopy

SEM = Scanning Electron Microscopy

EBSD = Electron Backscattered Diffraction

APT = Atom Probe Tomography

FAC = Fast Air Cooling

AC = Air Cooling

FEG-SEM = Field Emission Gun Scanning Electron Microscope

EDX = Energy Dispersive X-ray Spectroscopy

BSE = Back-Scattered Electron

DSC = Differential Scanning Calorimetry

H / LAGB = High / Low Angle Grain Boundaries

Contents

1.	Introduction	8
2.	Literature Review	9
2.1	Materials in Gas Turbines	9
2.2	IN939: Historical Perspective.....	11
2.3	Chemical Composition and Microstructure of IN939	12
2.4	Mechanical Properties of IN939.....	18
2.5	Heat Treatments for Cast and Additively-Manufactured IN939	21
2.7	Weldability Issues and Cracking Phenomena	28
2.7.1	Solidification Cracking.....	29
2.7.2	Liquation Cracking.....	30
2.7.3	Strain-Age Cracking.....	30
2.7.4	Ductility Dip Cracking	31
2.8	Studies on AM of difficult-to-weld Nickel-base superalloys.....	32
3.	Experimental Methods	36
3.1	Scheme of Experiments.....	36
3.2	DMLS builds	38
3.3	Powder.....	39
3.4	Heat Treatment	39
3.5	Metallographic preparation	40
3.6	Microscopy.....	41
3.7	Mechanical Testing	41
3.8	Thermal Analysis	42
3.9	Simulations.....	42
3.10	Sources of Error and Uncertainty in Results	42
4.	Results	44
4.1	Metallography and fractography of cracking	44
4.2	Scheil Solidification Simulation.....	47
4.3	Thermal Analysis of As-Built and Standard Heat-Treated Microstructure.....	51
4.4	Phase Transformations in IN939 – JMatPro Simulation	53
4.5	Microstructures of As-Built and Heat Treated IN939 in Metallography	54
4.5.1	HT-A: As-Built.....	54
4.5.2	HT-B: Solution Treated 4 hrs / 1160°C.....	60
4.5.3	HT-C: 4 hrs / 1160°C + 6 hrs / 1000°C	61

4.5.4	HT-D: 4 hrs / 1160°C + 6 hrs / 1000°C + 24 hrs / 900°C	64
4.5.5	HT-E: 4 hrs / 1160°C + 6 hrs / 1000°C + 24 hrs / 900°C + 16 hrs / 700°C	67
4.5.6	HT-F: 4 hrs / 1160°C + 16 hrs / 845°C	67
4.5.7	HT-G: 4 hrs / 1100°C	70
4.5.8	HT-J: 4 hrs / 1160°C + 6 hrs / 1000°C + 16 hrs / 700°C.....	71
4.5.9	HT-P: 6 hrs / 1000°C + 16 hrs / 700°C	71
4.5.10	HT-M: 40 hrs / 1160°C	72
4.6	Powder Microstructure	72
4.7	Tensile Testing Results	75
5.	Discussion	78
5.1	Identification of cracking mechanism	78
5.2	Rationale for selection of trial heat treatments.....	81
5.3	Phase Transformation Temperatures in As-Built IN939.....	81
5.4	Optimization of Solution Treatment Temperature	83
5.4.1	Precipitation of γ' after solution treatment.....	83
5.4.2	Effect of Solution Treatment on η -phase.....	84
5.5	Development of Microstructure and Mechanical Properties through HT Steps.....	85
5.6	Mechanical Performance and Creep Considerations.....	86
5.7	Future Work	88
6.	Conclusions	89
7.	References	90
8.	Appendix 1 – Thermal Analysis Results	94
9.	Appendix 2 – Tensile Testing Results.....	101

1. Introduction

The push for greater efficiency and improved performance in industrial and aerospace gas turbine engines has driven turbine-entry temperatures to impossible levels. The materials used in gas turbines are required to endure temperatures up to 90% of their melting temperature, and the technology to ensure performance is continuously evolving. Additive Manufacturing is an important leap in manufacturing technology which allows geometries to be manufactured that were never before possible.

Despite many decades having passed since their introduction, understanding of the metallurgy of Ni-base superalloys is still a work-in-progress. An area of considerable debate and recent advancement is weldability and mechanisms responsible for crack formation in these alloys. IN939 is one such superalloy which is considered “non-weldable” but is highly desirable for additive manufacturing due to its impressive properties in hot-gas path applications. Understanding the metallurgical phenomena and cracking mechanisms at play in IN939 is a major goal of this thesis.

Another challenge when introducing Ni-base alloys to additive manufacturing processes is development of heat treatments and testing of resultant properties. IN939 in cast form is conventionally given a long multi-stage heat treatment which results in a complex and stable microstructure. As the starting microstructure in an additively manufactured version of the alloy is bound to be different, the conventional heat treatment must be re-evaluated to determine whether it is practicable for the additively manufactured material. This is another issue the thesis aims to address.

The high cooling rates and fine solidification structures resulting from the additive manufacturing process have been demonstrated to be advantageous in mechanical performance. It is envisaged that this may allow optimization of the conventional heat treatments to achieve an edge in alloy performance, and the realization of this advantage is another objective of the thesis.

The research questions that the thesis aims to answer are stated so:

1. What mechanism or mechanisms cause cracking in IN939, and how can cracking be mitigated?
2. Are the heat treatments designed for conventionally cast IN939 effective for additively manufactured IN939?
3. Can conventional heat treatments be made more efficient or more effective?

2. Literature Review

2.1 Materials in Gas Turbines

Modern gas turbine engines are complex machines constructed from specialised materials to withstand the most severe service conditions. Figure 1 shows a simplified illustration of such an engine. The compressor section sucks in air (hence the name “gas” turbine) and compresses it to a high density. The air is also heated to approximately 400°C due to compression. This compressed and heated gas then enters the combustor section, where it is mixed with fuel and ignited. This is the hottest part of the engine, where the temperature may exceed 2000°C. The hot gases expand upon combustion and try to escape towards the downstream part of the engine, through the turbine section. In the most modern engines the upstream turbine components must endure temperatures as high as 1600°C [1]. The turbine is driven by the kinetic energy of the escaping gases, and further drives the compressor through a system of concentric shafts. In turbo-fan type aero-engines, the low-pressure turbine typically drives the turbo-fan, which generates the majority of the thrust. Thrust is also supplemented by the exhaust gases. In power generation applications the turbine is often coupled to a generator through a gearbox, while the exhaust gases are typically utilized for steam-generation.

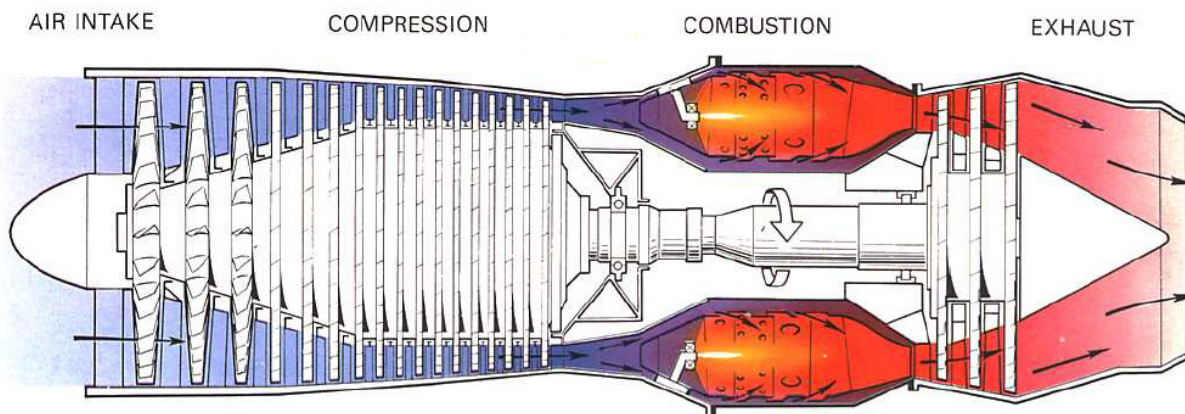


Figure 1: Overview of a gas turbine engine. Reprinted with permission from Rolls-Royce plc. Source: [2]

Materials for gas-turbine engines vary depending on application. Weight for aero-engines must be kept low, so lower-density materials are typically selected where possible. The criteria for industrial and power generation gas turbines is different; the focus is on efficient and continuous operation, and denser more robust materials can be used. In both cases the materials are often specifically developed for the intended application. Whether a component is rotary or stationary, typical requirements are: high temperature tensile strength, creep resistance, high temperature corrosion resistance, dimensional stability, and high fatigue strength. Naturally the aforementioned temperatures in the hot sections cannot be endured by any

alloy unaided, and cooling of the metallic components using air or steam, along with application of coatings, is necessary to ensure performance. Figure 2 shows the evolution of turbine blade cooling technology over several decades [2].

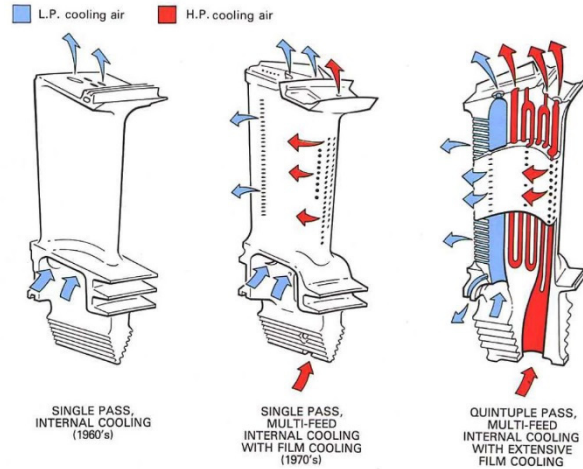


Figure 2: Evolution of blade cooling technology. Reprinted with permission from Rolls-Royce plc. Source: [2]

The specific materials used in various parts of gas turbine engines are often kept confidential by the respective manufacturers, however an example of material categories is given in Figure 3 for the GT-26 industrial gas turbine by Alstom [3]. The lower-temperature sections are constructed from ferritic and austenitic steels, while nickel-base alloys clearly dominate the combustor and turbine sections. The first stage of the high-pressure turbine is manufactured from a single crystal nickel-base alloy, to provide creep strength and high mechanical properties in the longitudinal axis. Directionally solidified alloys are used for similar reasons in the second stage turbine, though the material demands here are less extreme.

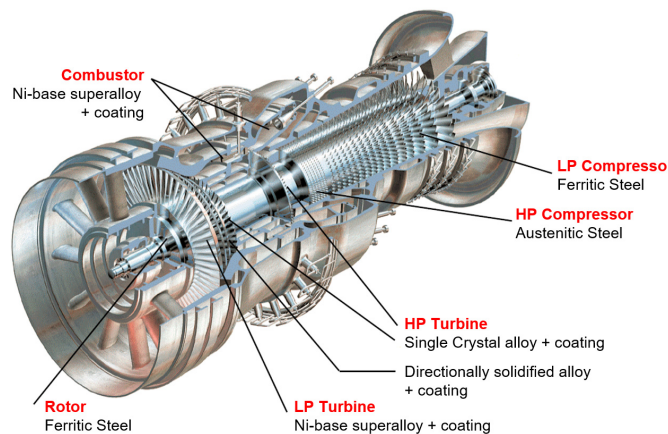


Figure 3: Material types used in different sections in an Alstom gas turbine engine. Re-drawn from [3]
 Link: www.modernpowersystems.com/uploads/pictures/web/h/y/p/gt26_for_article.jpg

The complicated nature of a gas turbine necessitates many components with precise and complex geometry, and manufacturing processes are in turn required to produce these components. Superalloy parts

in gas turbines are typically cast or wrought, and large assemblies are often welded together. In addition, welding is often used as a repair method for defects in castings. Hence the manufacturability of a high-temperature material plays a significant role in its adoption for use in gas turbines [4].

Nickel-base superalloys are generally defined as materials for service at 650°C and above, having a face-centered-cubic (FCC) crystal structure, and being strengthened by precipitation of a coherent intermetallic phase [5]. These alloys are generally complex in composition, typically having at least 8 major and minor alloying elements apart from the base element nickel. They can be manufactured as cast or wrought alloys, and specifications may differ depending on processing route. The complex alloying means that techniques such as vacuum arc remelting (VAR) and vacuum induction melting (VIM) are essential to produce the desired and uncontaminated composition of the alloy. The multitude of alloying elements also means that the material can respond unexpectedly to thermal and/or mechanical processing, as in the various cracking phenomena seen in welding. Alloys for use at 650°C or thereabouts, such as the ubiquitous Alloy 718, generally have lower volume fractions (18 to 20% for alloy 718 [5]) of hardening phase, and may be wrought and joined by conventional welding processes. With increase in hardening phase volume fraction to around 50% (e.g. IN100), the alloys must be cast to near-net shape and weldability is poor [5]. Single crystal alloys such as CMSX-4 with ~75% volume fraction hardening phase have even more limited processability. Given the high initial cost of these materials (CMSX-4-Re can cost \$9500/kg [3]) it is necessary that they be manufactured, repaired, and maintained at reasonable cost throughout their life-cycle.

2.2 IN939: Historical Perspective

The prolific growth and technology-pull of the aviation industry during and after the Second World War was a major driver for superalloy development. New alloys were developed and tested at many centres in Europe and Asia, but many of the most adopted alloys came out of the International Nickel Company (INCO) in the United States. IN939 was developed as a cast alloy with higher volume fraction of precipitation-hardening phase and superior corrosion resistance compared to the incumbent IN738LC, allowing service at ~850°C. Blades and vanes in land-based turbine engines were the intended application. A common trade name for IN939 is Nimocast Alloy 739 [6]. Performance targets for the new alloy included: stable microstructure free from σ -phase precipitation after 10,000 hrs; corrosion resistance comparable to wrought Nimonic 101; at least 4% elongation to failure in tensile and creep tests at all temperatures; suitable impact properties after long service; stress rupture life of 1750 hrs at 816°C and 276 MPa; castability similar to IN738LC [7]. Characterization and testing done on the alloy showed that these targets were achieved or exceeded, and that the alloy also possessed weldability superior to IN738LC [7][8].

In more recent work [9] IN939 was modified by the Cannon-Muskegon Corporation to have improved weldability. The content of precipitation hardening elements had to be lowered and thus the volume of precipitation hardening phase also decreased. The alloy was designated CM 939 Weldable® and was said to have comparable properties to IN939 through modified heat treatment regimes. Sjöberg et al. assessed the original IN939 for use in constructing large structures in aero-engines in the conventionally cast, welded, and spray-formed conditions [10]. With repair welding of overaged castings in mind, the weldability by electron-beam and laser methods was generally considered acceptable. Static mechanical properties were generally acceptable, however fatigue tests showed mixed results.

	Cr	Co	C	Fe	W	Mo	Nb	Ta	Ti	Al	Zr	B	Ni	Others
IN939	22,5	19,0	0,15	-	2,0	-	1,0	1,4	3,7	1,9	0,1	0,01	Bal	-
	Developed for long exposure at temperatures upto 850°C, corrosion resistance, and stable microstructure.													
IN718	19,0	-	0,04	18,5	-	3,0	5,1	-	0,9	0,5	-	-	Bal	-
	γ' strengthened superalloy, weldable, restricted to temperatures < 650°C – Offered for AM.													
IN738	16,0	8,5	0,1	-	2,6	1,7	0,9	1,7	3,4	3,4	0,1	0,01	Bal	-
	High temperature creep and corrosion resistance, used in hot gas path, not considered weldable due to high Al and Ti content.													
Hast X	22,0	1,5	0,1	18,5	0,6	9,0	-	-	-	-	-	-	47,0	
	Primarily solid-solution strengthened alloy used in wet-corrosion applications – Offered for AM.													
Mar-M247	8,0	10,0	0,15	-	10,0	0,6	-	3,0	1,0	5,50	0,03	0,015	Bal	1,5 Hf
	High γ' volume fractions, good creep and corrosion at high temperatures and good castability.													

Table 1: All figures in wt%. Source for IN939: [7]. Source for other alloys: [11]

2.3 Chemical Composition and Microstructure of IN939

The INCO specification for the chemical composition of IN939 is shown in Table 1, along with the chemical compositions of several other closely related Nickel-base superalloys. The composition includes highest content of Ni which results in the FCC crystal structure matrix. High amounts of Cr (22.5%) and Co (19.0%) are present in the alloy, along with several other major and minor alloying elements. In addition to the elements listed in Table 1, there can be several trace elements [12] in the alloy such as silicon, phosphorus, sulphur, lead, bismuth, tellurium, selenium, and silver. Even parts-per-million levels

of these elements can have a significant impact on the superalloy properties, so advanced analysis techniques must be utilized by alloy manufacturers to detect them. Table 2 presents a summary of the effects different elements have on the properties of Ni-base superalloys. Note that not all effects may be observable in a given alloy.

The microstructure of superalloys can be complex, containing many constituent phases. Nickel-base superalloys have a matrix of FCC Nickel, designated the γ phase, which acts as the base or solvent for many other elements in the alloy. One reason nickel is particularly suited for this role is that it has a reasonably high melting point of 1455°C, and forms no allotropes upto this temperature, i.e. the FCC crystal structure is stable until the melting point. This is in contrast to Fe and Co which change their structures at high temperatures while still solid. In addition to this, Ni is favoured as the main matrix constituent because it has a high tolerance for alloying without becoming physically unstable, on account of its nearly filled third electron shell. Ni also forms chromia (Cr_2O_3) and (at high temperatures) alumina (Al_2O_3) under certain conditions when alloyed with Cr and Al respectively, and this gives the resulting alloy excellent corrosion resistance properties [11].

Effect	Alloying Elements
Solid-solution strengtheners	Co, Cr, Fe, Mo, W, Ta, Re
Carbide formers:	
MC	W, Ta, Ti, Mo, Nb, Hf
M ₇ C ₃	Cr
M ₂₃ C ₆	Cr, Mo, W
M ₆ C	Mo, W, Nb
Carbonitrides: M(CN)	C, N
Forms γ' Ni ₃ (Al, Ti)	Al, Ti
Raises solvus temperature of γ'	Co
Hardening precipitates and/or intermetallics	Al, Ti, Nb, Ta
Oxidation resistance	Al, Cr, Y, La, Ce
Improve hot corrosion resistance	La, Th
Sulfidation resistance	Cr, Co, Si
Improves creep properties	B, Ta
Increases rupture strength	B
Grain-boundary refiners	B, C, Zr, Hf
Retard γ' coarsening	Re

Table 2: Roles of alloying elements in Ni-base superalloys [12]

Chromium alloying plays a multi-pronged role in the microstructure of superalloys. The main motivation for alloying Cr to high amounts (22,5% in the case of IN939) is to promote formation of the protective Cr_2O_3 oxide layer that gives the alloy its hot corrosion resistance. Chromium is mainly found in the γ matrix, it is a potent solid-solution strengthener, and also appears in the form of carbides and topologically close-packed (TCP) phases.

The role of cobalt alloying content on microstructure and properties of Nickel-base superalloys has long been a subject of debate. According to literature Co goes into solid solution and increases volume fractions of “favourable secondary precipitates” [12], while another source claims that low-temperature solubility of titanium and aluminium (the chief γ' forming elements) is decreased in the matrix by the addition of cobalt [11]. A study conducted for NASA in 1983 by researchers at Columbia University concluded that the net effect of Co on mechanical properties of wrought Ni-base superalloys is very subtle and difficult to quantify, and that the alloys would retain their functionality if the Co content was completely replaced by Ni [13]. Indeed, Co was heavily added to superalloys in the 60s, but its usage was reduced when Co prices spiked in the early 1970s [5]. A study by Wang et al in 2016 shows that for a single crystal alloy, increasing Co content actually does not affect the volume fraction of strengthening precipitates. However, it does decrease the coefficients of diffusion in the matrix, thereby reducing the precipitates' coarsening rate [14]. Morphology of the precipitates also becomes less cuboidal with increasing Co content. Adding Co widens the alloy's solidification range, and this can result in increased segregation on solidification. For cast alloys this can be a significant problem. Wang et al also claimed that Co reduces the solvus temperature of precipitation hardening phases, which leads to finer precipitates after solution heat treatment. These effects may or may not be valid for conventional polycrystalline alloys (such as IN939), and there does not yet appear to be a real consensus on the effects of Co on superalloys in general.

Molybdenum and tungsten are both solid solution strengtheners, since they are refractory elements. They are found in the matrix, and are also strong carbide formers [11]. They may not be particularly desirable elements in alloys for aerospace applications, since they tend to increase the overall density of the material. However, it is important to note that solid-solution strengthening persists at high temperatures, which makes it an important strengthening mechanism in view of the intended application conditions of superalloys.

Aluminium and titanium serve as the basis for the precipitation hardening mechanism in nickel-base superalloys. They are commonly found in many nickel-based superalloys in combined concentration of 6 to 10 wt.%. They combine with Ni to form the ordered intermetallic compound Ni_3Al and Ni_3Ti , which is called the γ' precipitate. In addition to this most important role, Al also produces an oxide scale (Al_2O_3) which is far more stable than the Cr_2O_3 oxide scale at high temperatures. Al has a significantly different atomic radius to Ni (6% difference) and has a considerable solid solution strengthening effect when dissolved in the matrix [11]. Titanium has only a weak solid-solution strengthening effect, but can also be present as a carbide. Tantalum is another refractory element that has a solid-solution strengthening effect when in the matrix and is found in ~2 wt % in some alloys, including IN939. Ta also promotes γ'

precipitation but has an affinity for carbon and thus forms carbides as well. A similar role is played by niobium, which forms the Ni_3Nb precipitate called γ'' . Alloys such as IN718 that have lower amounts of Al and Ti have more Nb content, and are mainly strengthened by precipitation of γ'' [5],[11].

It is a common misconception that elements added as γ' and γ'' formers are the only ones found in the precipitates' lattices. While Al, Ti, Nb, and Ta are certainly the most likely precipitate-formers, studies have shown that Mo, W, Cr, and Co atoms can all be present in the γ' lattice [11].

The role of carbon, boron, and zirconium in the microstructure of superalloys is not yet clearly understood. Carbon in the form of carbides has been shown to have beneficial effects on creep and rupture strength. In the early years of superalloy development researchers observed that carbides on grain boundaries had deleterious effects on ductility, and so reduced the carbon levels to as low as possible. They soon learnt that reduction of carbon to below 0,03% drastically reduced creep life [11]. Carbon also reacts with the carbide forming elements in the matrix and this influences the chemical stability of the matrix, but can also have undesirable effects such as sensitization (intergranular corrosion). Therefore, the carbon content needs to be carefully formulated and controlled for optimum properties in the alloy.

Boron and zirconium are both found in minute concentrations but have remarkable effect on creep properties: among other benefits, creep life can be increased 13 times, and rupture stress up to 1.9 times. The mechanisms by which this is achieved is still unclear. B and Zr have odd atomic radii in that they are 21 to 29% oversized or undersized, and thus segregate to the grain boundaries, which are the most vulnerable areas to rupture cracks. Several mechanisms have been proposed to explain their effects, however the most general explanation is that B is filling vacancies and thus reducing grain boundary diffusion, and Zr is playing the role of a "getter" and minimizing elemental sulphur at the grain boundaries by forming $\text{Zr}_4\text{C}_2\text{S}_2$ [11]. A recent study on phases formed at grain boundaries in the same alloy different B content showed that the element has an undoubtedly positive affect on creep life [15].

Figure 4 shows the microstructure of cast IN939 which was exposed to 790°C for 1500 hours. Prior to exposure the alloy was given a solution heat treatment of 1150°C for 4 hours and an ageing of 850°C for 24 hours. The figure highlights some of the important phases that are present in the alloy.

Figure 4(a) represents the grain structure of the alloy, which is characterized by equiaxed grains roughly 0.5 mm in diameter. Such a course grain size would be expected in a conventionally cast part, especially after solution and ageing heat treatment. Carbide particles with dimensions in the range of tens of microns, as shown in Figure 4(b), can be seen at the grain boundaries and within grains. Since IN939 contains a nominal 0.15 wt % of carbon, carbides of the reactive and refractory elements would be expected to form as the MC-type. After exposure at high temperatures during heat treatment and service, these carbides

decompose to $M_{23}C_6$ and M_6C forms. The $M_{23}C_6$ form carbides are often located at grain boundaries and can have a diverse morphology. The M_6C carbides are more randomly distributed in the microstructure [12]. Carbides in such concentrations are thought to be essential for the ductility of the alloy, as well as for creep resistance at high temperatures [11].

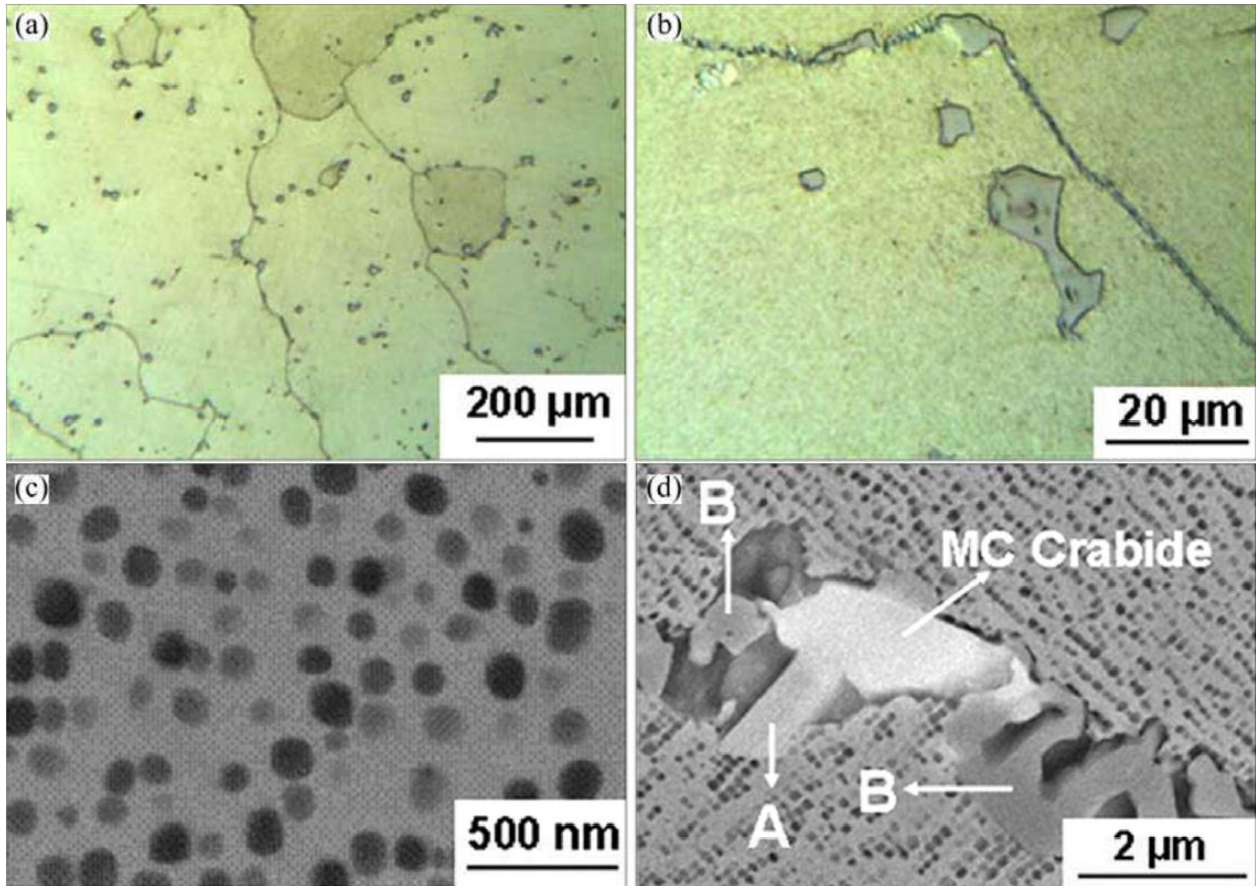


Figure 4: Microstructure of cast IN939 after 1500 hrs at 790°C [16]. Reprinted with permission from Elsevier B V

In Figure 4(c) the γ' phase appears as dark grey circles. The light grey background is the γ matrix. Perhaps it would not be incorrect to say that the “super” in “superalloy” refers to γ' . It is the principle strengthening phase that allows these materials to be used at temperatures up to even 90% of their melting point. The γ' phase is an intermetallic phase of the form A_3B , where $A = (Ni, Co)$ and $B = (Al, Ti)$. The γ' phase precipitates out of the austenitic FCC matrix, and also has an FCC crystal structure (ordered $L1_2$ structure). It has a lattice parameter (0.3561 nm for pure Ni_3Al) which has approximately 0.1 to 1% mismatch with the γ -austenite phase, meaning it is coherent with the matrix. The coherency has positive implication for mechanical properties, but also means that the precipitate can nucleate homogeneously, having low surface energy and excellent long-term stability. The γ' interacts with dislocations and impedes the deformation process. The amount of energy required for a dislocation to pass through a precipitate is increased because of the ordered structure. The γ' can be spherical in morphology, as seen in

Figure 4, or it can have a cuboidal morphology. The morphology is dependent on lattice mismatch, with 0 to 0.2% mismatch showing spherical morphology and 0.5 to 1.0% mismatch forming cubes. Cuboidal morphology can be advantageous as it means that more γ' can be contained in the same amount of material, i.e. higher volume fraction. Some single crystal alloys have γ' volume fractions of up to 75%. Above 1.25% mismatch the γ' becomes plate-like. The γ' phase is inherently ductile and hence does not cause embrittlement or loss of fracture toughness. The precipitates strength in fact increases as temperature increases. γ' is found within grains but often nucleates at grain boundaries in high strength alloys. This is believed to help improve rupture properties [11], [12].

The characteristic microstructure of cast IN939 after standard heat-heat treatment is described given as below [7]:

- Coarse grains sizing 0.5 to 1.5 mm
- γ -matrix with coarse (~150 to 200 nm) and fine (~20 nm) γ' particles [17] –overall 32 wt% of γ'
- MC and $M_{23}C_6$ carbides – having ~1.4 wt% of total phases

As is the case with most precipitation hardening alloy-systems, the optimum precipitate is a meta-stable phase. Similarly, Ni-base superalloys can form so-called “Topologically Close-Packed” (TCP) phases, examples of which can be seen as the particles marked “A” and “B” in Figure 4(d). TCP phases include σ , Laves, and μ phases among others, and are intermetallic compounds of the transition elements. The μ phase has a rhombohedral crystal structure, and most often occurs in alloys with high W or Mo content. The Laves-phase has a hexagonal structure and the general formula A_2B , where B is often a heavy atom such as Ta, Nb, or Mo. The TCP phases generally form after extended high temperature exposure. They may not be a problem in small amounts but can have detrimental effects in high volume fractions. They can have varied morphology, e.g. globules or platelets. In particular, a platelet-like morphology can have severe embrittling effects on the alloy [11], [12]. A detailed list of phases observed in various conditions of IN939, as presented in [7], is recreated in Table 3 below:

Phase	Condition	Composition
γ/γ' eutectic islands	As-cast	
γ - matrix	4-step HT	(Ni, Cr, Co, Al, Ti, W, Ta, Nb)
γ' - coarse	4-step HT	(Ni, Co, Al, Ti, Cr, W, Nb, Ta)
γ' - fine	4-step HT	(Ni, Al, Ti, Co, Cr, W, Nb, Ta)
MC	4-step HT	MC _{0.88} (Ti, Nb, Ta, W) (C, N, Si, S, Zr)
MC	4-step HT	Nb-rich, Ti-rich
M ₂₃ C ₆	4-step HT + service exposed	Cr ₂₁ (Mo, W, Ni, Co, Ti, Zr) ₂ (C, B) ₆
σ	4-step HT + service exposed	(Ni, Co, Cr, Al, Ti, W, Ta, Nb)
η	As-cast	Ni ₃ (Ti, Ta, Nb, Al)
H	All conditions	(Zr, Ti) ₂ (C, S)
ϵ	4-step HT + service exposed	Elemental Cr (Ni, Co, Cr, Ti, W, Ta, Nb)

Table 3: Phases found in various conditions of IN939 [7]

Several other phases or relatively less significance are also found in superalloy microstructures, and an extremely useful reference detailing phases commonly observed in superalloys can be found as Table 3.1 in Donachie and Donachie [12], and similarly as Table 4.1-1 in Durand-Charre [5].

2.4 Mechanical Properties of IN939

The properties that make superalloys uniquely suitable for use at high loads and temperatures are exceptional corrosion resistance and exceptional mechanical performance. A summary of the mechanical properties of IN939 is given in Table 4. It is important to note that the precipitation-hardening nature of the alloy means that mechanical properties can vary depending on the processing history: as-cast material will have a different set of properties to solution-treated or aged-hardened material. The properties will also change with time when the alloy is exposed to high temperatures, as the γ' precipitates will coarsen, and other thermodynamically stable phases will form in the microstructure.

As evidenced by Table 4, room temperature tensile properties of IN939 are considerably high, and the alloy shows adequate ductility as well. However, for gas turbine engine components such as blades, disks, and vanes, stress rupture and fatigue are also extremely important properties. Moreover, the material is required to perform at high temperatures, where deformation mechanisms for static as well as cyclic loading act much faster. Indeed, the 0.2% yield strength at 870°C is only half of the room temperature yield strength, and the 1000-hr rupture strength decreases from 425 MPa at room temperature to only 60

MPa at 760°C. Another important property which is less talked about is fracture toughness, which is defined as a materials resistance to propagation of an existing crack, or brittle fracture. This can be important since gas turbine components are prone to fatigue cracks, and a material with a high fracture toughness will be less likely to fail catastrophically. The same applies for impact toughness, in order to protect engines from failure by Foreign or Domestic Object Damage (FOD or DOD) i.e. loose object in the gas flow that may collide with the internal engine components at great velocity [2].

Mechanical Properties of IN939					
	21°C	650°C	760°C	870°C	980°C
Yield Strength 0.2% Offset (MPa)	800	695	635	400	205
Ultimate Tensile Strength (MPa)	1050	985	915	640	325
Tensile Elongation (%)	5	7	7	18	25
1000-hr Rupture Strength (MPa)	425	195	60		
Youngs Modulus (GPa)	195 to 205				
Compressive Strength (MPa)	700 to 880				
Flexural modulus (GPa)	195 to 205				
Modulus of Rupture (MPa)	700 to 880				
Shear Modulus (GPa)	75 to 85				
Bulk Modulus (GPa)	140 to 165				
Poisson's Ratio	0.27 to 0.29				
Fatigue strength at 10 ⁷ cycles (MPa)	340 to 535				
Fracture toughness (MPa√m)	26 to 28.9				
Hardness (H _v)	250 to 350				
All values are given for tests at RT unless otherwise stated. Values given in ranges account for aging condition of alloy.					

Table 4: Mechanical Properties of IN939. Source: [6], [11]

Cost is always an important factor when considering materials for production, and Figure 5 shows an Ashby chart that compares the cost and yield strength among many common superalloys. The Ashby chart was prepared using the CES Edupack 2017 software by Granta Design [6]. Note that only room temperature yield strength data is available in this software.

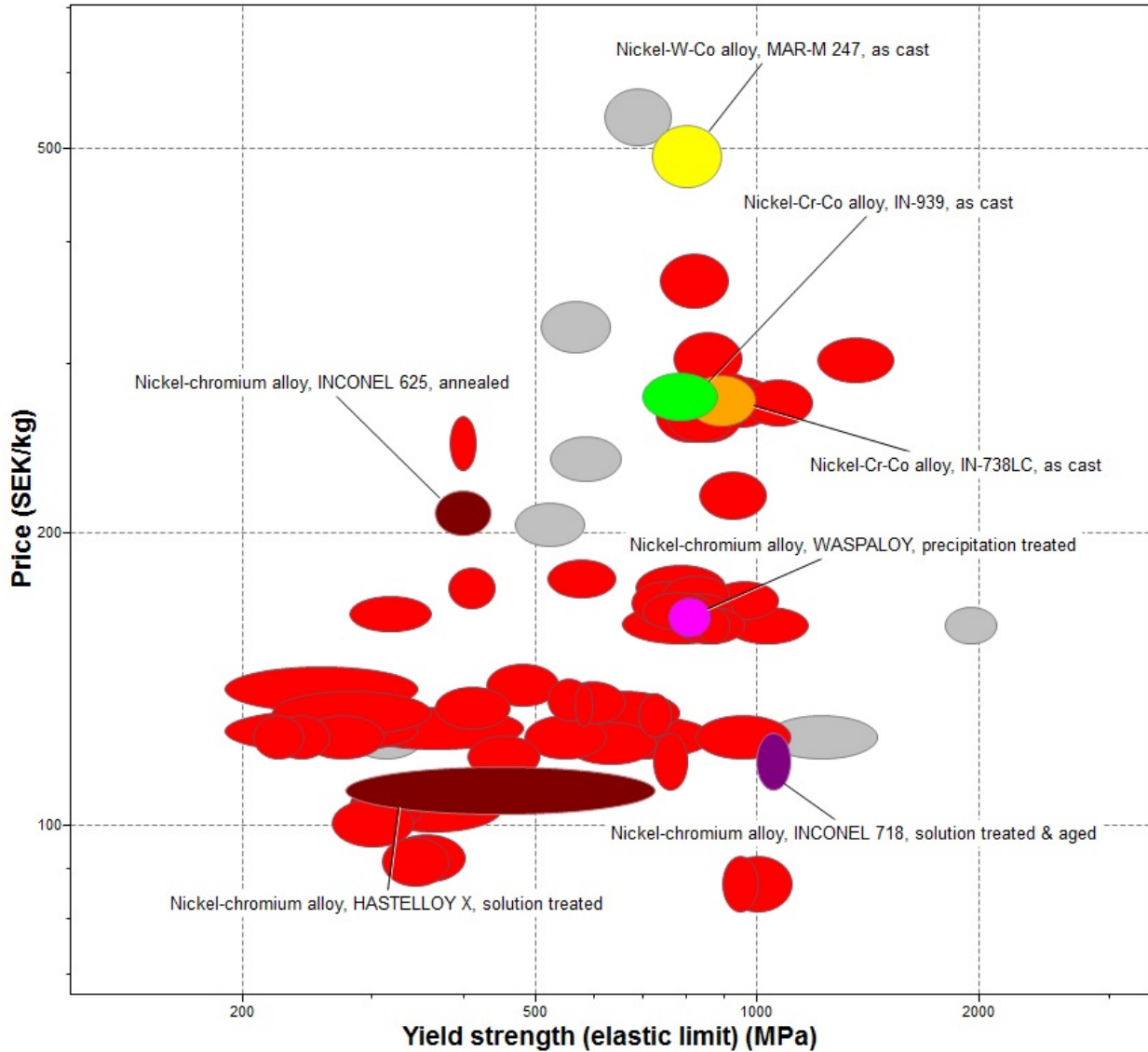


Figure 5: Ashby diagram - Cost vs Yield Strength of Common Superalloys. Source: [6]

The chart in Figure 5 shows that IN939 is at the higher end of both yield strength and cost. It has ambient temperature yield strength comparable to IN718, but significantly higher cost per kilogram. Naturally this is due to the temperature factor – IN718 has inferior mechanical properties and corrosion resistance at temperatures above 650°C. Compared to IN738LC the cost and RT yield strength of IN939 are quite similar, but corrosion resistance of IN939 is superior, as discussed in Section 2.2. Mar-M247 commands a much higher price than IN939, but also provides superior creep and corrosion resistance at high temperatures [6][18].

2.5 Heat Treatments for Cast and Additively-Manufactured IN939

The purpose of heat treatment in any precipitation hardening alloy is to achieve size and distribution of hardening-precipitates that result in optimum mechanical properties. However, due to the complex microstructure (and ambitious range of required mechanical properties) in superalloys, it can be quite challenging to formulate a heat treatment regime that is both effective in strengthening and efficient in time and cost.

The publication by Shaw [8] presents a comprehensive history of development of heat treatment for IN939. The same treatment is also included in the review by Gibbons and Stickler [7], along with a number of shortened heat treatment regimes. A 4-stage heat treatment was initially developed for IN939 which resulted in the best compromise of tensile ductility, yield strength, and stress rupture life. However, the excessive time required for such a heat treatment was not considered economically feasible (heating and cooling time in addition to 50 hrs at temperature), and shorter processing routes were sought after.

	Temperature (°C)	Time (hrs)	Cooling	Remarks
4-Stage HT	1160	4	FAC	Produces best overall mechanical properties.
	1000	6	FAC	
	900	24	AC	
	700	16	AC	
2-Stage HT	1160	4	FAC	Suitable for less demanding applications, e.g. stationary vanes.
	1000	6	AC	
FAC = Fast Air Cooling; AC = Air Cooling				

Table 5: Heat treatment routes for IN939. Source: [7], [8], [12]

The standard heat treatment consists of one solution treatment stage followed by three ageing steps. The 1160°C stage dissolves almost all γ' and η phase, and homogenises the alloy. On cooling from solution temperature, the γ' phase already precipitates, and this grows in the 1000°C ageing step. This step also precipitates small amounts of MC carbide on the grain boundaries. The second ageing step at 900°C reportedly grows the γ' further and also strengthens grain boundaries by precipitation of discrete $M_{23}C_6$ particles. The last ageing step at 700°C precipitates fine γ' particles with a diameter of only about 10 nm, which considerably improve room temperature and intermediate temperature yield strength [8]. According to Durand-Charre, however, these finer precipitates are not desirable as they lead to ductility reduction and thermal fatigue problems [5].

Comprehensive tensile and stress-rupture testing by the alloy developers showed that omitting the two secondary ageing treatments at 900°C and 700°C produces adequate properties for less demanding applications, allowing IN939 to replace some cobalt based alloys. The 2-stage heat treatment also improved ductility and weldability, and could be used as a preparation for repair welding [8].

Sjöberg et al, when evaluating IN939 for aerospace engine applications, formulated an abbreviated 3-stage heat treatment which resulted in a microstructure with serrated grain boundaries. This has been said to reduce the tendency for “oxidation assisted intergranular high temperature creep crack growth”. A post-weld solution heat treatment was also developed, which entailed extremely fast heating (20 to 24°C per minute) through the γ' precipitation temperature range, to minimize chances of strain age cracking [10].

Heat Treatment Step	Effects
Step 1: Solution Treatment 4 hrs / 1160°C	<ul style="list-style-type: none"> ▪ homogenisation of γ matrix ▪ dissolution of γ' ▪ η rounded or dissolved ▪ primary MC unchanged, secondary MC formed on cooling ▪ fine γ' (20 nm) formed on cooling
Step 2: Ageing-1 6 hrs / 1000°C	<ul style="list-style-type: none"> ▪ precipitation of primary γ' (70 to 150 nm) ▪ precipitation of MC at grain boundaries
Step 3: Ageing-2 24 hrs / 900°C	<ul style="list-style-type: none"> ▪ growth of primary γ' (70 to 150 nm) ▪ precipitation of $M_{23}C_6$ at grain boundaries in the form of strings of discrete particles
Step 4: Ageing-3 16 hrs / 700°C	<ul style="list-style-type: none"> ▪ precipitation of fine γ' (20 nm) resulting in bi-modal distribution ▪ slight increase in amount of $M_{23}C_6$

Table 6: Effects of each step of Standard 4-Step Heat Treatment as per [7]

For critical applications such as in the aerospace industry, end users prefer to minimize risk by subjecting all components to Hot Isostatic Pressing (HIP). In HIP parts are held at high temperatures in a chamber with high pressure inert gas, which removes pores and makes the part fully dense [19]. Philpott et al evaluated the effects of HIP, standard 4-step heat treatment, and a modified 2-step heat treatment on cast and DMLS-processed IN939 [20]. They concluded that the DMLS-processed IN939 underwent recrystallization and grain growth, but still had a much smaller grain size than cast IN939. They also observed significant difference in precipitation and growth behaviour of carbides, with the DMLS-processed material having networks of much finer carbide particles in the microstructure after heat treatment. γ' precipitation was also studied, and no significant difference was observed between cast and DMLS-processed material. However, mechanical performance of the samples was not evaluated.

René-41 is a Ni-base superalloy with properties and applications similar to IN939. Investigations into the microstructure, properties, and thermal processing response of René-41 built by Laser Metal Deposition (LMD) was carried out by J. Li et al [21], [22]. Laser Metal Deposition (LMD) is another additive manufacturing process for metallic materials. Instead of a laser melting powder in a bed, the powder (or wire) is fed co-axially into the melt pool formed by the laser. The process has significantly higher build-rates than PBF, and the resulting columnar-grained microstructures are also coarser. Li et al characterized the microstructure before heat treatment, after solutionizing, and after ageing. The standard heat-treatment was applied, consisting of a solution step at 1065°C for 4 hrs followed by air quenching, and ageing at 760°C for 16 hrs with air cooling. The as-built microstructure was dendritic with MC carbides in the inter-dendritic regions. The γ' size differed between dendrite cores and inter-dendritic regions, with the former hosting larger precipitates. The microstructure after solution treatment still contained γ' precipitates, indicating that the 4 hrs at 1065°C was not adequate for complete solution. The columnar grain structure was not affected by solution treatment, but dissolution of the MC carbides was noted. After ageing, these carbides transformed to $M_{23}C_6$ and M_6C carbides, while γ' precipitates coarsened and coalesced into chains. Testing showed that the mechanical properties overall (except hardness) were below the required aerospace specification for René-41, even after ageing, and the as-built material actually had a higher yield strength and ultimate tensile strength than aged. This shows that heat treatments for cast or wrought material may not be suitable for additive manufactured parts, and treatments must be designed based on the starting microstructure [21], [22].

The characteristic columnar grain structure of PBF builds imparts strong anisotropy to the material. This heavily textured grain structure is not easy to anneal-out. Popovic et al produced fine and coarse-grained microstructures within individual IN718 samples by varying parameters in the L-PBF process. They subjected the samples to combinations of annealing, solution, ageing, and HIP heat treatments, to study how post-processing affects the microstructure and properties. They found that none of the heat-treatment regimes, including annealing at 850°C for 2 hours, or HIPing at 1180°C for 2 hours at 150 MPa, could homogenize the grain size [23]. Muñoz-Moreno et al studied the effect of different solution treatment temperatures on L-PBF built CM247LC. The tested solution-temperatures ranged from 1150 to 1260°C. They observed that recrystallisation only occurred for solution treatment above 1240°C, and that some anisotropy in elastic properties was retained even after recrystallization. Samples solutionised below 1240°C only experienced recovery. An important feature of recrystallized samples was their finer and more uniform γ' precipitates, while non-recrystallized samples had coarser γ' precipitates. Carbide morphology and distribution was similar for the recrystallized and recovered samples. These findings further emphasize that post processing and heat treatment can affect not only grain structure, but also morphology, distribution, and size of strengthening precipitates [24].

The stability ranges of various phases, as well as the solidus temperature of the alloy, are of prime importance when designing the solution and precipitation ageing heat treatments. A summary of the most important reaction temperatures for IN939 from various sources is given in Table 7.

Phase reaction	Temperature (°C) <i>Gibbons et al</i>	Temperature (°C) <i>Formentti et al – from DTA</i>	
		Heating	Cooling
Liquidus temperature	1340	1339	1325
Formation of primary MC	~1300	1276-1313	1250-1290
Solidus temperature	1235	1235	-
η solvus temperature	1145		~1209
γ' solvus temperature	1080-1100	-	-
$M_{23}C_6$ solvus temperature	~1000	-	-
σ solvus temperature	~950	-	-
Max rate of σ formation	~850	-	-

Table 7: Summary of reaction temperatures for IN939, as given by [7] and [25]

An important factor to consider when formulating heat treatment is the intended service temperature of the part. If the component is intended to be used at temperatures above 600°C for extended durations, then secondary ageing will continue to occur during service. In such a situation consideration may be given to installing the alloy in an under-aged condition, and allowing it to reach peak strength during service.

The geometry of the component also affects the heat treatment result, as it directly affects the cooling rate experienced by the material. A thin section will experience a faster cooling rate, and here precipitates may be fine, while the interior of a thick section will grow coarse precipitates due to a much slower cooling rate. Thin sections will also have finer grain sizes from casting, smaller carbide particles, and less elemental segregation [7]. Practical considerations, such a heating equipment, atmosphere, and cooling practise also play a role. Industrially, vacuum induction furnaces are used for heating, with forced gas flow for quenching the charge.

2.6 Additive Manufacturing and the DMLS process

Additive Manufacturing (AM) is an increasingly important approach to manufacturing components with complex geometries, with unique properties, and in lesser time to market. The basic idea is to “add” material in layers to build-up a part, as opposed to removal of material from a larger blank, as would be the case for conventional “subtractive” manufacturing processes. The addition of material is controlled by an automated process for which the primary input is a 3D CAD model of the desired part. This is where the main attraction lies – the ability to go from CAD model to solid part with minimal time or preparation in between, and no requirement for expensive moulds and tooling, or complex tool-path programming [19].

Many of the technologies now part of the super-set of additive manufacturing technologies were first developed in the 80s and 90s as methods of producing prototypes of products under development. The technologies were then known as “Rapid Prototyping”. Today a common synonym is “3D-printing”, which has come about after many of the simpler technologies for polymer additive-manufacturing have seen adoption by workshops, hobbyists, and home-users. However, AM technologies are of growing importance as they now have the capacity to produce industrial-strength parts in series-production and in a variety of materials [19].

The Direct Metal Laser Sintering process developed by EOS GmbH is categorized as a “Powder Bed Fusion” additive manufacturing technology. Figure 6, sourced from EOS GmbH’s website, describes the main sequence of steps in the DMLS process [26].

The DMLS process involves some more practical aspects than shown in the figure, such as requirements for support structures for overhanging components, and stress-relief and machining for part removal. The powder properties are, however, most important for the process. Fine powder with particle size between 10 to 60 μm is used, and layer thicknesses are also within the range of tens of microns. The powder must have a combination of controlled chemical composition, spherical shape for good flowability, and consistent particle size distribution. Most powders are produced by the Gas Atomization process. But when higher purity is required, more advanced techniques such as Vacuum Inert Gas Atomization (VIGA) or Electrode Induction Gas Atomization (EIGA) must be used.

Although the DMLS process is named as “sintering” it does not actually sinter the powder but melts it completely. In fact, the material in each layer is melted multiple times, and the whole part usually goes through multiple heating and cooling cycles as the laser repeatedly scans over it. This has a huge bearing on the microstructure of the built part. The laser power P , scan speed v , powder layer thickness d , and hatch spacing (distance between adjacent scan lines) h determine the heat input H of the process.

$$H = \frac{P}{v \times h \times d} \quad (J \text{ mm}^{-3}) \quad (1)$$

H is also known as the energy density and must be carefully selected for a given material and process. Too low a heat input will incompletely melt the material and layers will not be continuously fused together i.e. lack of fusion defects will be formed. Excessive heat input may evaporate elements in the material, or coarsen the solidification structure, causing excessive segregation and triggering various cracking mechanisms. Other important parameters include the laser spot size, shielding gas, and shielding gas flow rate, but these are not as frequently varied during process design [18], [19].

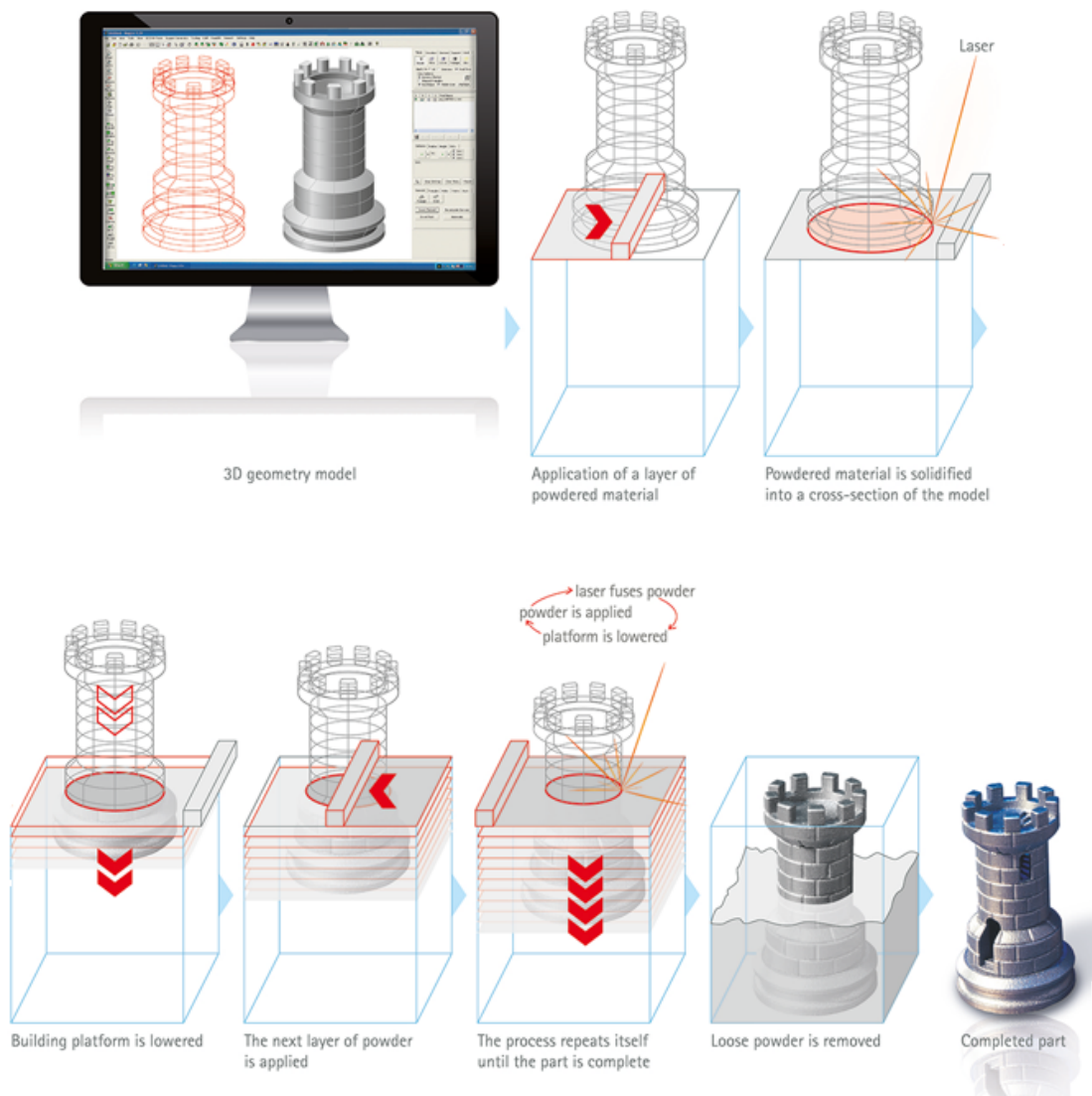


Figure 6: A graphical description of the Direct Metal Laser Sintering process. Source: [26] Pictures © EOS GmbH

The microstructure produced by the DMLS process is naturally very different from conventionally cast or wrought microstructures, due to the melting, remelting, and thermal cycling of small volumes of material. The grain structure is usually fine and columnar, with high aspect ratio grains oriented in the building direction (i.e. perpendicular to the plane of the build platform). These grains span across multiple layers due to epitaxial growth. Since the volume of material being melted in each scan line is very small compared to the volume of the build platform and build, the cooling rate is extremely fast (10^3 to 10^5 °C/s [19]) and segregation is limited. A comparison found in literature [20] between conventionally cast and DMLS-processed IN939 microstructures is shown in Figure 7. Difference in grain size, orientation, and carbide size (bright precipitates) is clearly visible. In many cases this microstructure leads to considerably higher strength in the DMLS-processed material, due to the Hall-Petch effect [19].

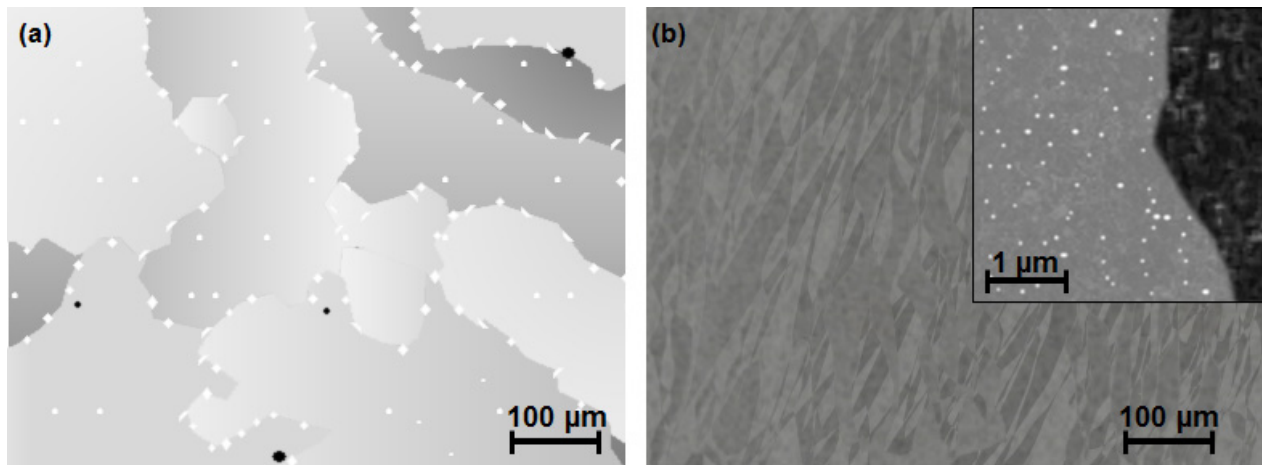


Figure 7: BSE images showing (a) cast, and (b) DMLS-processed IN939. Re-drawn based on: [19]

Table 5 shows specifications of the three main DMLS machines offered by EOS. The major differences in machines are their build-volumes and lasers. The smaller M100 machine has a less powerful laser with a smaller focus diameter, allowing finer features to be built. The M400 machine has the largest build envelope and the most powerful laser, to enable high productivity in large builds. EOS also offers the M400 Quattro, which has 4 lasers for increased throughput. A variant of the M100 is the M080 which is specialised for precious metals.

The capabilities of the machines are distinct enough that processes for different materials need to be designed differently on each machine. The EOS M290 and M400 are able to process a wide variety of materials, including aluminium alloys, steels and stainless steels, cobalt-chrome, and titanium alloys. Currently Ni-base superalloys that are commercially available for additive manufacturing using the DMLS process are IN625, IN718, and Hastelloy-X. Other suppliers of laser-based powder bed fusion technology include Concept Laser GmbH, Renishaw plc, and SLM Solutions Group AG. The only supplier currently marketing powder for IN939 is SLM Solutions.

2.7 Weldability Issues and Cracking Phenomena

Direct Metal Laser Sintering builds up material in layers by selectively melting powder, and so the process can be compared to repeated bead-on-plate welding, where the plate is a bed of powder and the melt pool dimensions are in tens of microns. Therefore, existing know-how from welding and fabrication experience can be used to design processes and understand DMLS processing problems in the various alloys. However, the weldability and cracking susceptibility of Ni-base superalloys is still a vast and complex subject. As is the case with other aspects of their metallurgy, the factors contributing to cracking and evolution of microstructure are not yet completely understood. There are three main cracking phenomena that are deemed relevant: solidification cracking, liquation cracking, and strain-age cracking. Ductility-dip cracking has not been commonly encountered in Ni-base alloys, but in view of the nature and novelty of AM processes, cannot be ignored. Many sources in literature examine mechanisms for each phenomenon in detail for various alloys. This section will attempt to summarize the major factors leading to each of these four cracking mechanisms.


	EOS M 100	EOS M 290	EOS M 400
Build Volume	Ø100 x 95 mm	250 x 250 x 325 mm	400 x 400 x 400 mm
Laser Specs	200 W Yb-fiber laser	400 W Yb-fiber laser	1 kW Yb-fiber laser
Focus Diameter	40 µm	100 µm	~90 µm
Precision Optics	F-theta lens, high speed scanner	F-theta lens, high speed scanner	F-theta lens
Scanning Speed	Up to 7 m/s	Up to 7 m/s	Up to 7 m/s
			

Table 8: DMLS machine offerings from EOS. Source: [27]–[29] Pictures © EOS GmbH

The weldability of a Ni-base alloy varies greatly depending on the alloying content of the specific alloy. Dilute, solid-solution strengthened alloys such as Hastelloy-X and IN625 are considered weldable and can be joined with conventional Tungsten Inert Gas (TIG) or laser welding processes without problems, if the

appropriate welding procedures and pre- and post-treatments are utilized. Low-volume fraction precipitation-hardened alloys such as IN718 and Waspaloy are more prone to cracking, and usually have to be welded in the solution-annealed state. However, these are still considered weldable alloys. The alloys considered “non-weldable” or “difficult-to-weld” are highly alloyed ones with high γ' volume fractions, such as IN939, IN738, and Mar-M247. These are higher performance alloys and are used in critical hot-gas path components, so flexibility in their manufacture or repair by welding or additive manufacturing would be highly valuable [30].

2.7.1 Solidification Cracking

Solidification cracking is also known as weld-centreline cracking and falls within the super-set of “hot cracking” as it occurs immediately upon welding. A classical representation of solidification cracking is reproduced in Figure 8. The newly deposited weld metal is solidifying inwards from the edges of the weld pool, and the last part to freeze is the centreline. The liquid film present here is pulled apart by the tensile stresses generated due to solidification shrinkage, forming a crack in the middle of the weld fusion zone [30]–[32].

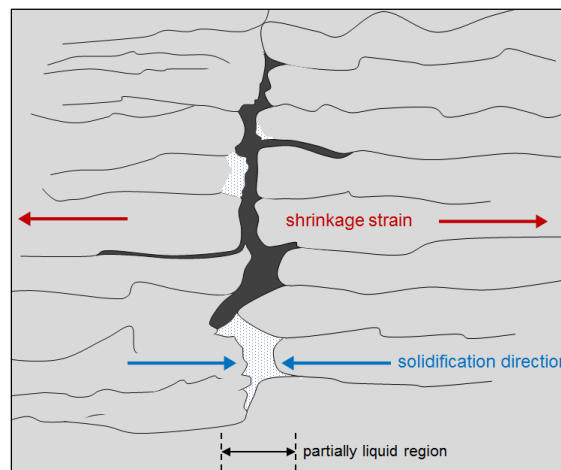


Figure 8: Illustration of Solidification Cracking mechanism in welds. Re-drawn from [32]

Grain boundary strengthening elements such as C, B, and Zr increase susceptibility to solidification cracking since these elements segregate to the inter-dendritic regions upon melting, and form the low-melting-point liquid film. P and S have the same effect and must be kept to lowest-possible levels since they provide no benefit to the alloy. As a general rule, alloying additions that widen the solidification range will promote solidification cracking.

According to DuPont et al, B lowers the solid/liquid surface energy, promoting extensive wetting of the newly-solidified grains with the inter-dendritic liquid, which favours cracking. They also provide examples of low-temperature phases that form between 1100 °C and 1200°C, such as M_3B_2 type phases,

ZrS, and TiS. A study specific to IN939 shows that cracking susceptibility is dependent on cumulative levels of Zr, B, and S. When B is held at 0.001 to 0.005 wt.%, Zr can be added up to 0.04 wt.% without increasing cracking susceptibility, while at 0.01 wt.% B, any Zr increase worsens cracking behaviour. The same study showed that reducing S concentration meant that tolerance for both B and Zr could be increased [31]. Such data provides further evidence of the complex interactions between trace quantities of alloying elements and the need to keep a stringent control on alloy impurities.

Alloys containing significant amounts of Nb are susceptible to formation of γ /Laves and γ /NbC eutectic phases, due to segregation of Nb. These phases can cause solidification cracking. At 1 wt.% Nb and 0.15 wt.% C, this is unlikely to be a problem for IN939 [31].

2.7.2 Liquation Cracking

Another type of hot cracking is Liquation Cracking, which occurs in grain boundaries in the Heat Affected Zone of welds. Also known as HAZ-fissuring, liquation cracking occurs when low-melting-point phases formed on grain boundaries in the heat affected zone are melted by the heat from a weld run. A film of liquid is formed on these grain boundaries, which is then pulled apart by the tensile thermal stresses on solidification of the weld. Phases that are likely to be “liquated” in Ni-base superalloys include MC carbide, M_6C carbides, Laves phase, and σ -phase [30].

A lower heat input can reduce the width of the HAZ, and thus subjects less material to the temperature and stress conditions potentially causing liquation cracking [31]. This is one factor that can be utilized to mitigate this cracking phenomenon. The grain structure of the material being welded is another factor in a material’s susceptibility to liquation cracking. A coarse grain structure in the HAZ increases chances of liquation cracking since grain-boundaries are expected to have more content of segregated elements, and are thus more likely to form low-melting-temperature phases. Fine grained microstructures (such as those found in wrought, or additively manufactured components) are less vulnerable to liquation cracking. Annealed or solution treated material is also expected to be less susceptible to liquation cracking. Addition of Mg and Mn is thought to reduce liquation cracking. The elements in IN939 most likely to form low-melting-point phases are C, B, Zr, P, and S [30]–[32].

2.7.3 Strain-Age Cracking

Strain-Age Cracking (SAC) is a phenomenon unique to precipitation-hardening Ni-base alloys. It is a type of “cold-cracking” or “solid-state cracking” and occurs not during welding but when the material is re-heated for post-weld heat treatment, and thus it is often termed “re-heat cracking”. SAC is most often seen in the HAZ, and the cracks are always inter-granular. The mechanism behind SAC has been widely

theorized but no consensus yet exists. However, scholars generally agree that the cracks form due to excessive stress from precipitation of γ' which cannot be accommodated by the grain boundaries. When γ' precipitates out from the γ matrix there is a stress generated due to the mismatch between respective lattice parameters. The stress may be exacerbated by residual stresses from the weld process, and the microstructure may have a reduced ductility due to precipitation of carbides at grain boundaries [30], [31].

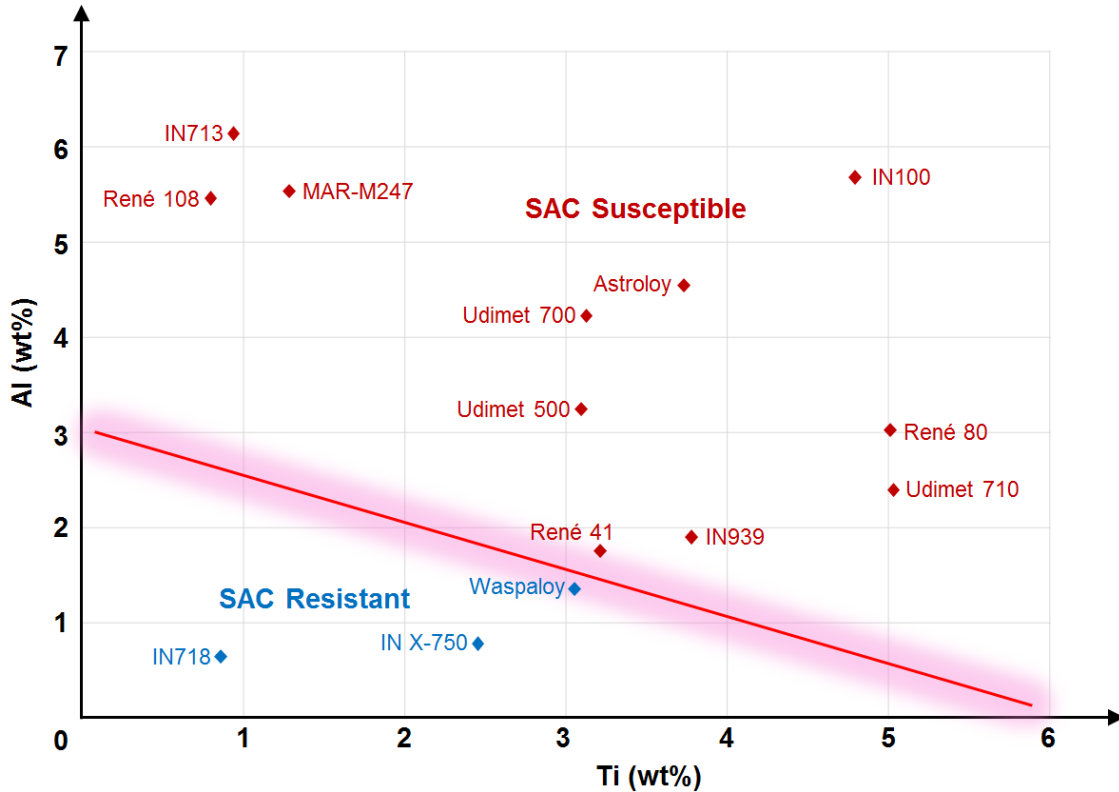


Figure 9: Effect of Ti and Al content on SAC susceptibility. Re-drawn from [31]

According to DuPont et al, high SAC susceptibility is the reason that large γ' volume fraction alloys are considered unweldable. Alloys with Al + Ti content in excess of 6 wt. % are particularly vulnerable. The Al plus Ti content has been used as a qualitative measure of SAC susceptibility, and Figure 9 shows one such diagram. The rate of precipitation is also an important factor, and alloys that precipitate γ' at a faster rate are more susceptible to cracking [30], [31]. The phase γ'' that strengthens alloys such as IN718 precipitates out from the matrix at a much slower rate, and so makes SAC much less likely during welding of IN718 and other γ'' -strengthened alloys. IN718 was, in fact, developed to overcome just this problem.

2.7.4 Ductility Dip Cracking

Ductility Dip Cracking (DDC) is a solid-state cracking phenomenon that often occurs in austenitic alloys. Although it has not been widely reported for Ni-base superalloys [31], the conditions under which it is active may well be encountered during L-PBF processing, and thus it cannot be ignored as a possible

defect-formation mechanism. It can take place even in materials which have S, P, and B impurity levels low enough to avoid solidification and liquation cracking [33]. DDC produces intergranular cracking in the weld metal or HAZ, and usually occurs when material is reheated, such as in multi-pass welding.

Most materials have high ductility at temperatures close to their melting point, which drops gradually with decreasing temperature. However, some materials exhibit a “ductility-dip” i.e. a range of temperature between around $0.6T_m$ and $0.9T_m$ where their ductility is uncharacteristically low. DDC cracking occurs when the material temperature is passing through this low-ductility region. For Ni-base alloys, this temperature range is between 800°C and 1150°C . Since DDC occurs by sliding of grain-boundaries, a zip-zag or serrated grain boundary morphology, or precipitate-pinned grain boundary microstructure promotes resistance to DDC.

2.8 Studies on AM of difficult-to-weld Nickel-base superalloys

Ni-base alloys such as IN625, Hastelloy-X, and IN718 have been the main focus of industrial and academic researchers engaged in AM-material development, undoubtedly due to their amenability to melt-processing. However, several studies have been performed on higher γ' volume fraction alloys, mostly focused on IN738LC and Mar-M247. IN939 has also been studied by multiple groups.

Attallah et al [34] published a review on the outstanding problems to be solved for successful adoption of Ni-base superalloys in AM. The review cites DDC as an issue at $0.4T_m$ to $0.7T_m$ for Ni-base superalloys that form grain boundary carbides, and a weldability assessment diagram is included, as shown in Figure 10. However, the mechanism does not appear to be a problem for IN939, which appears within the “readily weldable” section of the diagram.

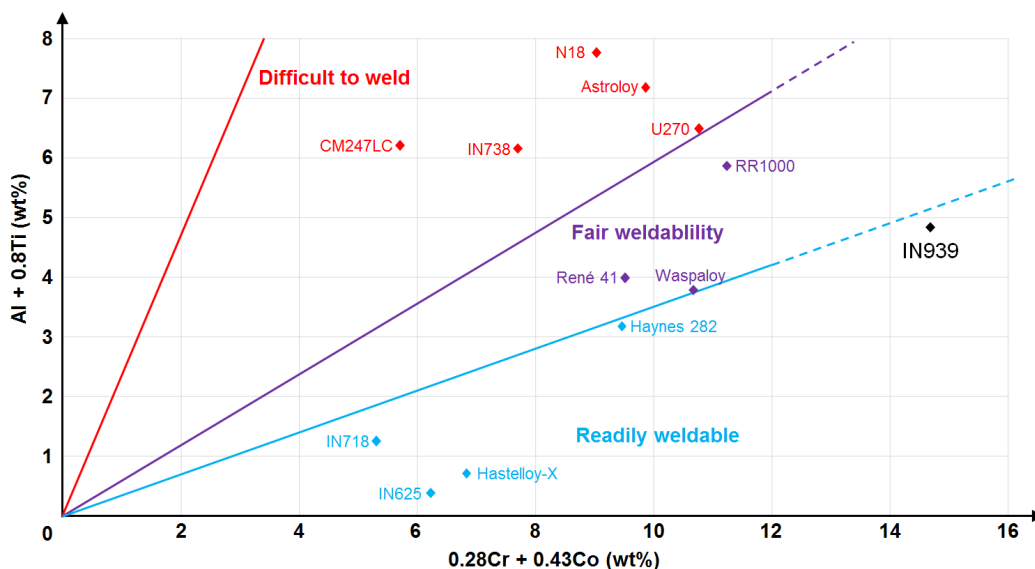


Figure 10: Weldability assessment diagram for DDC of Ni-base superalloys. Re-drawn to include IN939. Source:[34]

Attallah et al stressed the importance of component geometry as a factor in propensity for solidification cracking, emphasizing that larger components produce greater thermal gradients which increase solidification cracking. Differences in opinion among scholars on the deleterious or beneficial effect of high energy density on solidification cracking were also identified. Effect of Zr segregation on cracking was reiterated [34].

Carter et al attempted to examine the influence of various parameters on the laser powder bed fusion process for CM247LC alloy, which is a lower carbon version of Mar-M247. They employed the popular practise of building simple cubes and sectioning them parallel to the build direction to examine the microstructure. Extensive cracking was observed in the builds, with jagged cracks extending in many directions parallel and oblique to the build direction. The researchers used image analysis to quantify the cracking. They concluded from crack appearance that cracks at high heat input conditions were solidification cracks, while another unidentified solid solid-state cracking mechanism was claimed to be active for lower energy density conditions. A comparison of the crack details is shown in Figure 11. A HIP treatment was performed and demonstrated that cracks could be closed, but the mechanical performance of HIPed material was not evaluated [35].

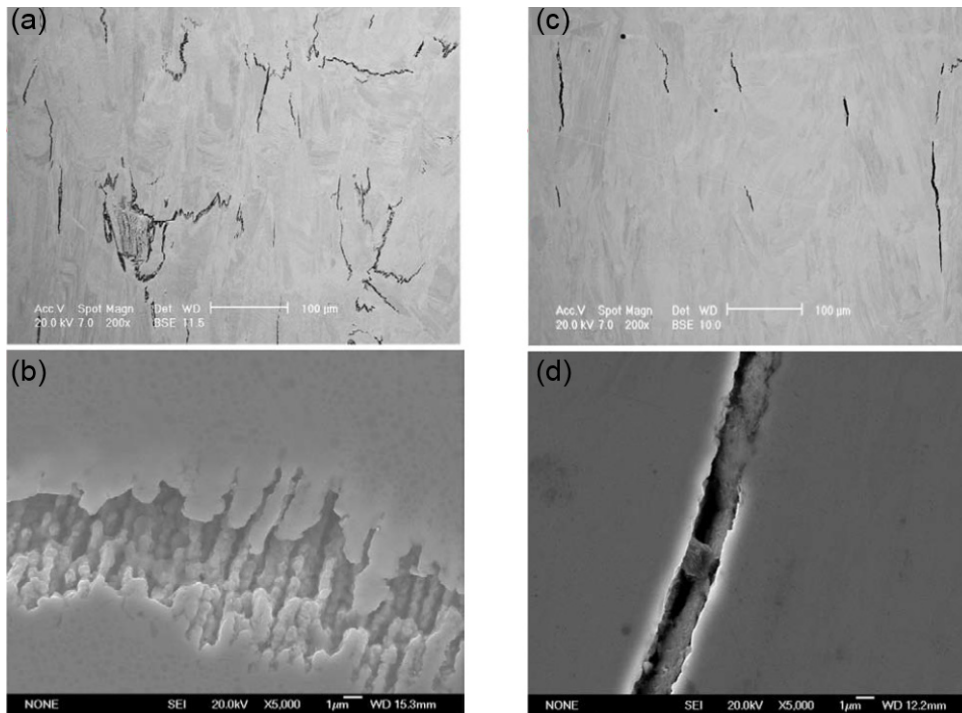


Figure 11: (a)(b) showing cracks from high heat input process suspected to be solidification cracking, and (c)(d) showing cracks from low heat input process suspected to be caused by solid-state cracking.
Source: [35]. Reprinted with permission from John Wiley and Sons

Kanagarajah et al produced IN939 samples in an SLM Solutions machine with the intention of comparing static and cyclic mechanical properties to conventionally cast material. No cracking was reported in the

article. Processing parameters were not disclosed. Transmission Electron Microscopy (TEM) and Scanning Electron Microscopy (SEM) were used to study the as-built microstructure, which was observed to be cellular. In the aged condition the same material was shown to have γ' precipitates of around 100 nm, similar to cast material. TCP phases were also observed in the microstructure with needle-like morphology. The results from static testing by Kanagarajah et al are reproduced in Figure 12. They clearly show that L-PBF produced IN939 shows higher yield strength in both as-built and aged conditions, at ambient and high temperature. The trade-off is that ductility is significantly reduced when the material is aged. In cyclic loading the as-built L-PBF IN939 performed better than as-cast at ambient temperature. At 750°C the cast material showed more cycles to failure in both as-cast and aged conditions [36].

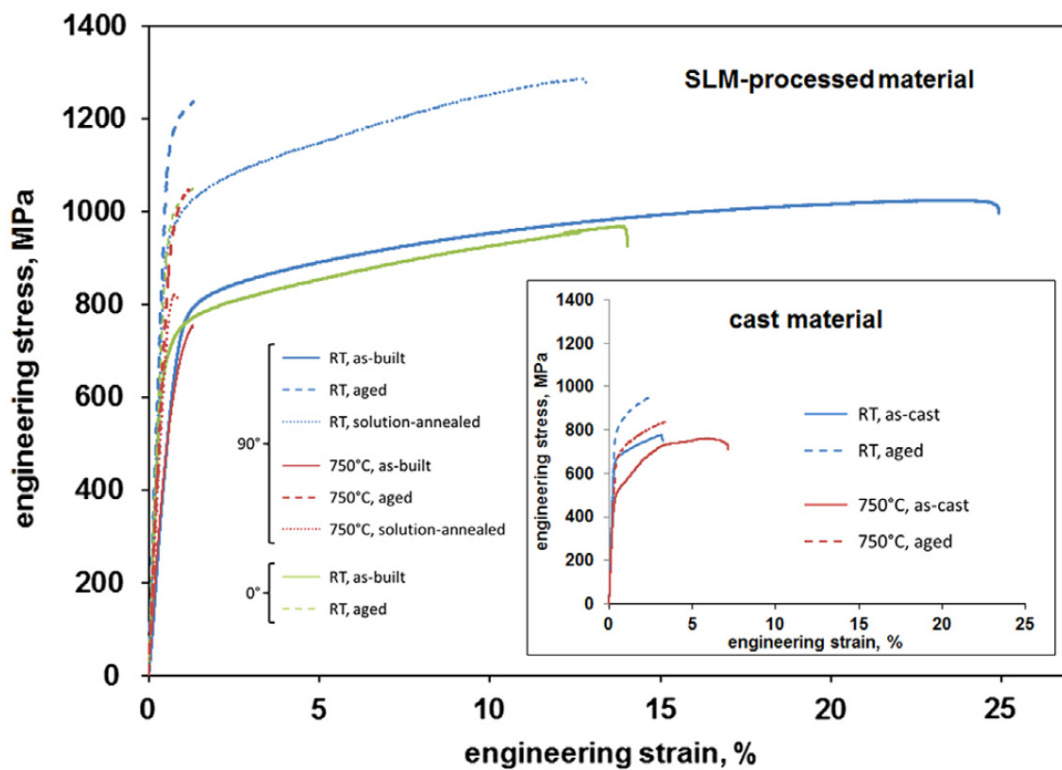


Figure 12: Tensile testing results for L-PBF built and 2-step heat treated IN939. Source: [36]. Reprinted with permission from Elsevier B V

The microstructure of L-PBF-built IN738LC was studied by Cloots et al using (among other techniques) Electron Backscattered Diffraction (EBSD) and Atom Probe Tomography (APT), in an attempt to understand the buildability of IN738LC using L-PBF. Several process parameters were varied, including hatch distance, scan speed, and laser beam intensity profile at the focal plane. The results of parameter variation showed that low scan speed (i.e. high energy density) resulted in high crack density but raising scan speed increased the frequency of lack of fusion defects and porosity. APT results showed significant Zr and B presence at the grain boundaries. This was correlated to a Scheil-solidification simulation of the alloy, which showed not only Zr in liquid phase at low temperatures, but also a very low solidus

temperature of 682°C. Based on this and microscopy results the authors proposed solidification cracking caused by low-melting Zr-containing phase as the mechanism for cracking in L-PBF IN738LC. The authors also propose the complete removal of Zr and claim that it plays no positive role in the alloy, which contradicts conventional understanding. It is also worth noting that the alloy studied contained only 0.03 wt% of Zr, while IN939 has a nominal 0.1 wt% [37].

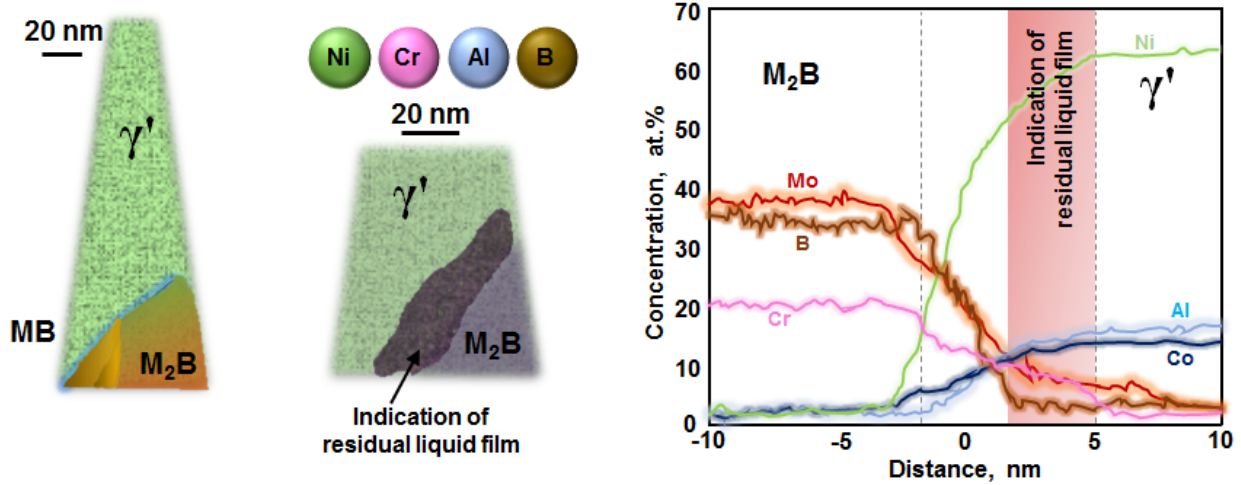


Figure 13: APT results showing Boron enrichment at grain boundaries. Redrawn based on [38]

Hot cracking in an unspecified “Ni-Co-Cr-Mo-Al-Ti-B” non-weldable Ni-based superalloy built by Electron Beam PBF was investigated by Chauvet et al. The high temperature maintained in the EB-PBF process resulted in a build having a coarse grain-structure, with extensive γ' precipitation occurring even in the as-built condition. EBSD analysis of the EB-PBF-built specimens showed high incidence of cracking at high-angle grain boundaries. Fracture studies were also performed and fractographs revealed a dendritic cracking morphology. This led the authors to exclude the possibility of solid-state cracking (i.e. SAC or DDC). Segregation of B was observed at grain boundaries, forming micron-sized precipitates of the MB, M_2B , and M_5B_3 types. The APT results have been redrawn and shown in Figure 13. The presence of B was again highlighted as playing a critical role in maintaining a low-melting-point liquid film. The build showed no cracks in the bottom, and the authors link this to higher grain boundary area in the bottom leading to elements with high segregation tendency to spread out over larger areas, as well as accommodation of stress by grain boundaries. Low incidence of cracking at the bottom of the build was also related to less restraint due to there being less built-up material under the melt pool [38].

3. Experimental Methods

3.1 Scheme of Experiments

The cracking behaviour of DMLS-processed IN939 was investigated by metallography and fractography. Builds showing cracks were examined in ZY-cross-section after metallographic preparation in the plain polished and etched conditions. In addition, tensile testing was performed to fracture the material. It was anticipated that the material may fracture along the cracks, and their appearance was studied by fractography.

Segregation of solute elements it well known to play a key role in cracking mechanisms. Thus it was attempted to study segregation by simulation using the Scheil Solidification Simulation module of the ThermoCalc software. The equilibrium composition of phases in the alloy was also attempted to be simulated using JMatPro version 9.1.2.

The material was also studied using thermal analysis techniques, namely Differential Scanning Calorimetry (DSC) and Dilatometry (DIL), in order to observe phase transformation behaviour during controlled heating and cooling conditions.

To investigate the effect of different heat treatment steps on the microstructure and mechanical properties of DMLS-processed material, the series of heat treatments designated A to P in Table 9 was performed.

HT	Heat Treatments			
A	-	-	-	-
B	1160°C / 4 hrs FAC	-	-	-
C	1160°C / 4 hrs FAC	1000°C / 6 hrs AC	-	-
D	1160°C / 4 hrs FAC	1000°C / 6 hrs AC	900°C / 24 hrs AC	-
E	1160°C / 4 hrs FAC	1000°C / 6 hrs AC	900°C / 24 hrs AC	700°C / 16 hrs AC
F	1160°C / 4 hrs FAC	845°C / 16 hrs AC	-	-
G	1100°C / 4 hrs FAC	-	-	-
H	1100°C / 4 hrs FAC	1000°C / 6 hrs AC	-	-
J	1160°C / 4 hrs FAC	1000°C / 6 hrs AC	700°C / 16 hrs AC	-
M	1160°C / 40 hrs FAC	-	-	-
N	1100°C / 4 hrs FAC	1000°C / 6 hrs FAC	700°C / 16 hrs AC	-
P	-	1000°C / 6 hrs FAC	700°C / 16 hrs AC	-

FAC = Fast Air Cooling, AC = Air Cooling

Table 9: List of Heat Treatments performed for evaluation of microstructure and mechanical properties

The As-Built condition of the material is represented by HT-A. The standard 4-step heat treatment for cast IN939, as mentioned in Section 2.5, is represented by HT-F. The 2-step heat treatment for IN939 is represented by HT-C, and another heat treatment with a single step ageing is represented by HT-F. HT-G is a low temperature solution treatment also found in literature. Several other heat treatment combinations were also formulated and evaluated, including changing cooling rates between Air Cooling and Fast Air Cooling. A discussion of the rationale behind the various trials is presented in Section 5.2.

For every heat treatment (with the exception of HT-L and HT-M) two metallographic samples, three horizontal tensile samples, and three vertical tensile samples were subjected to the respective heat treatment. The experimental methods used for production, treatment, and characterization of these samples are described in detail in the following sections.

3.2 DMLS builds

Samples for various analyses were produced in an EOS M290-400 DMLS machine, using a fixed set of parameters. The DMLS machine was operated using a platform temperature of 80°C, Argon gas atmosphere, and an energy density of 75 J.mm⁻³. The layer thickness of the building process was 40 µm. As the bulk properties of the DMLS-processed material are of prime importance to this investigation, additional parameters affecting the surface properties were omitted from the process. Standard EOS exposure patterns were utilized for the builds, whereby the direction of laser scanning vectors was rotated 67° between layers. The Flow Optimised exposure strategy was also consistently employed. This ensured that the laser was always travelling opposite to the direction of shielding gas flow, to avoid de-focusing of the laser beam by the smoke and spatter generated on melting. The build platforms used for the development builds were made of DIN 1.1730 grade “tool” steel.

Geometries built for various analyses are as follows:

- Samples for metallographic analysis were built as cuboids of 15 mm width x 15 mm depth x 18 mm height. Solid support structures were used.
- Horizontal tensile samples were built as cylinders of 80 mm length and 11 mm diameter. A combination of solid and “block” supports were used.
- Vertical tensile samples were built as cylinders of 45 mm length and 6 mm diameter. Solid support structures were used.
- Dilatometry samples were built as cuboids having length of 52 mm x 3 mm width x 6.50 mm height. Solid support structures were used here as well.

Figure 14 shows various parts as they appear after removal from the M290 machine.

At the time of initiation of this work, process development at EOS Finland Oy had already advanced to such an extent that building of a virtually crack-free IN939 was possible. However, in order to study the

cracking phenomenon, builds were performed with higher energy density. This was readily achieved by reducing the layer thickness to 20 μm . One further process having 20 μm layer thickness was used for building crack-free material in order to compare fracture behaviour. All tensile samples built for the purpose of fractography were oriented horizontally on the build platform.

The following table provides a summary of the process parameters sets that were used during this work, and their intended purposes:

Process Parameter Set	Energy Density ($\text{J}\cdot\text{mm}^3$)	Layer Thickness (μm)	Purpose
P1	100	20	Building of samples with high crack density for metallographic and fractographic study of cracks.
P2	105	20	Building of crack-free samples with similar layer thickness as P1, for comparison in fractography.
P3	75	40	Building of samples for heat-treatment study.

Table 10: Summary of process parameter sets and the samples built with each.

3.3 Powder

The powder used for DMLS builds was Gas Atomized powder having nominal composition as specified in Table 1, spherical morphology, and average particle size of 45 μm . Further details on the powder can be found in Section 4.6.

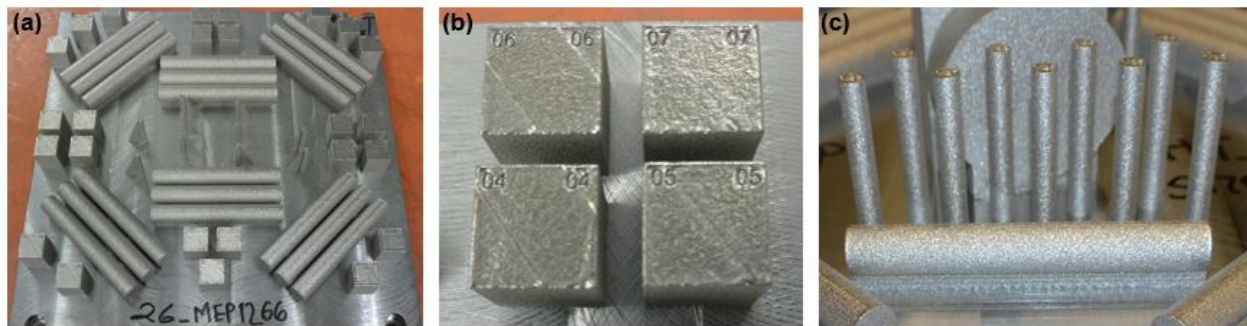


Figure 14: As-built DMLS parts still attached to the build platform after removal from the machine (a) complete platform, (b) cubes for metallographic examination, and (c) horizontal and vertical tensile bar blanks

3.4 Heat Treatment

Built parts were cut off from the building platform using a bandsaw, which had a kerf width of $\sim 2\text{mm}$. This ensured that no material affected by diffusion from the carbon steel building platform remained in the samples. No evidence of any elements from the build platform diffusing into the samples was found at any point in the experiments.

All heat treatments were performed in Nabertherm box furnaces with Argon gas atmosphere. Heating rates of $\sim 400^{\circ}\text{C/hr}$ were used. Where Forced Air Cooling (FAC) was required, samples were removed from the furnace and placed directly in front of air blowers. When Air Cooling (AC) was designated, the samples were placed in still air and allowed to cool naturally to room temperature. Temperatures during heat treatment were monitored using K-type thermocouples, and the industrial guideline of $\pm 15^{\circ}\text{C}$ was used when ensuring target temperatures.

3.5 Metallographic preparation

Metallographic samples were sectioned along two planes using an alumina cut-off wheel. Slow feed speeds and cooling fluid were utilised to minimize any effect of cutting on the microstructure. Cutting planes are illustrated schematically in Figure 15. Samples were mounted in Struers PolyFast (conductive resin) using a hot-mounting process. Grinding and polishing was performed with the following process: SiC paper FEPA# 320 \rightarrow SiC paper FEPA# 500 \rightarrow SiC paper FEPA# 1000 \rightarrow Struers MD-Mol cloth + DiaPro Mol $3\ \mu\text{m}$ \rightarrow Struers MD-Nap cloth + DiaPro Nap R $1\ \mu\text{m}$.

Etching of solid samples was performed by immersion in Kalling's 2 reagent, which consists of $5\ \text{g CuCl}_2 + 100\ \text{ml } 37\% \text{ HCl} + 150\ \text{ml Ethanol}$. Etching of powder samples was performed electrolytically using a solution of Perchloric Acid + 2-Butoxyethanol + ethanol + water.

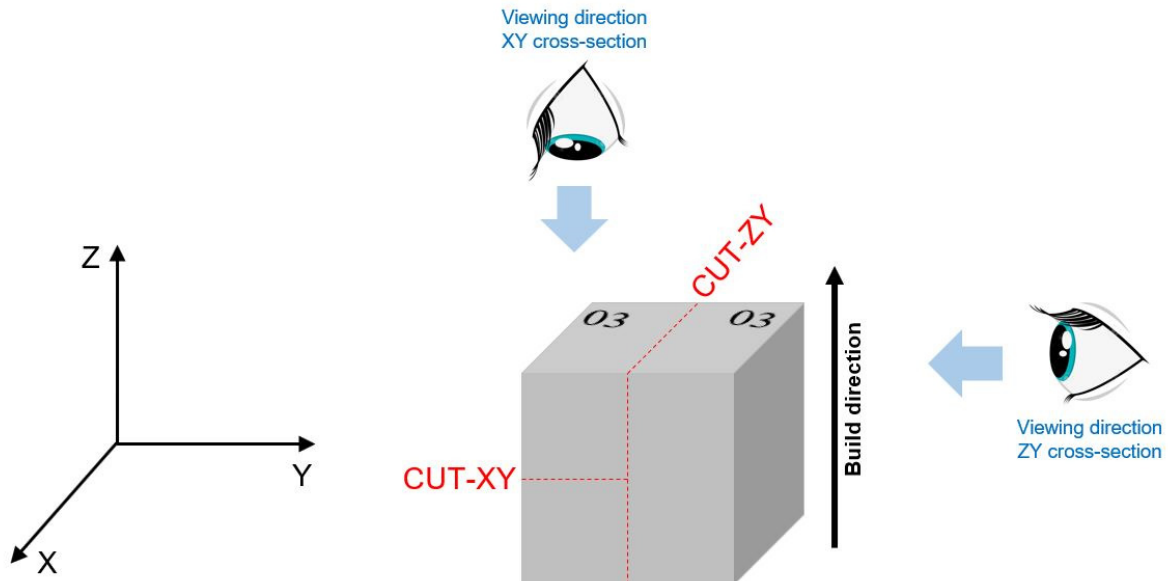


Figure 15: Planes and viewing angles of metallographic sections

3.6 Microscopy

Light optical microscopy was performed using an Olympus GX-51 inverted microscope with Stream Motion software for capturing and processing images. The microscope was equipped with a motorized stage which enabled capturing and stitching together images to make overviews of large areas.

Electron microscopy was performed using a LEO 1550 Gemini FEG-SEM, which is equipped with a detector for Energy Dispersive X-ray Spectroscopy (EDX). An “InLens” secondary electron detector was used for topographic imaging, while a “Centaurus” Back-Scattered Electron (BSE) detector was used for imaging with compositional contrast.

3.7 Mechanical Testing

To accommodate for the anisotropy of materials built using the DMLS process, tensile testing was performed of two kinds of samples:

- 1) Samples built to be tested with the axis of applied tensile stress perpendicular to the building direction – henceforth known as “Horizontal tensile” samples.
- 2) Samples built to be tested with the axis of applied tensile stress parallel to the building direction – henceforth known as “Vertical tensile” samples.

Horizontal tensile samples were machined into test specimens according to the ASTM E8M Fig 20 “Standard Round Machined Tension Test Specimen for P/M Products”. The original gauge length of these specimens was 25.4 mm and diameter was 4.75 mm. For practical reasons some heat treated specimens had to be machined according to ISO 6892 Annex D, having original gauge length 27 mm and diameter of 5 mm. The co-efficient of proportionality for both test geometries is the same, and the change in dimensions is minor; hence it is considered that results across specimens are comparable.

Vertical tensile samples were machined according to ISO 6892 Annex D with diameter of 4 mm and original gauge length of 16 mm.

All tensile testing (except fractographic samples) was performed on a Zwick/Roell BTC-EXMACRO.012 machine according to ISO 6892-1:2016(E) Method A (crosshead controlled) with a constant strain rate of 0.00025 s^{-1} throughout the test. All tensile testing was performed at room temperature.

Samples for fractography were tested using the same procedure but at a strain rate of 0.0001 s^{-1} .

Vickers Hardness testing was performed on a Struers Duravision 20 hardness tester using a load of 10 kgf on plain polished or etched metallographic samples.

3.8 Thermal Analysis

Samples for Differential Scanning Calorimetry (DSC) were extracted from metallographic sample cubes using the same cutting procedure detailed in Section 3.4. A Netzsch STA 449F1 Jupiter Simultaneous Thermal Analyzer was used for DSC. Samples were heated from room temperature to 1400°C at 10°C/min, and cooling was also performed using the same rate. An alumina crucible was used for containing the sample and an argon flow of 50 ml/min was used to keep the sample in an inert atmosphere.

Dilatometry was performed in a TA Instruments DIL802 dilatometer, with heating and cooling rates of 5°C/min in an argon atmosphere.

3.9 Simulations

All solidification simulations were performed using ThermoCalc 2018 with the TCNi8 database using the Scheil Solidification Simulation module. Following are the phases which were included in the simulation: FCC_A1, FCC_L12, FCC_L12#2, FCC_L12#3, FCC_L12#4, LIQUID, M3B2, M2B_TETR, and NI3TI_D024. Start temperature was 1400°C and a temperature step of 1°C was used.

For prediction of phase fractions and phase changes under equilibrium condition a step-temperature simulation in the JMatPro version 9.1.2 software was used. The phases included in the simulation were liquid, γ , γ' , MC, and η phases. A 1 degree step was used from 25°C to 1400°C.

3.10 Sources of Error and Uncertainty in Results

Interpretation of the results included in this thesis must be done while bearing in mind that experimental data are susceptible to various sources error and uncertainty. While every effort has been made to use best laboratory practices, standardise testing methods, and discard obviously misleading results, there is still a likelihood that measurements include some error or micrographs are misrepresentative.

When building samples in DMLS machines, the quality of parts is generally considered to be constant for a particular set of process parameters. However, some hardware systems have been known to produce marginally fewer defects in the middle of the build platform compared to the edges. The proximity of parts to each other may also affect the defect count. For these reasons care was taken to build parts for any particular heat treatment at various regions of the platform. The DMLS process has also been known to vaporise material and result in minor changes in the composition. While heat treatments were performed

in argon gas atmosphere, this was not enough to prevent oxidation, and minor change in composition as a result of oxidation or decarburization is not impossible. These factors must be considered when interpreting results in light of the nominal IN939 composition.

As discussed earlier, heat treatments were performed in box-type furnaces, and temperatures were monitored using K-type thermocouples. The temperature in such furnaces may vary by as much as ten or fifteen degrees from region to region within the furnace, and K-type thermocouples have the same margin of error.

All results that depend on metallographic techniques are susceptible to inconsistencies in sample preparation. For Ni-base superalloys the etching step is known to be challenging, due to the alloys' passivating nature and high corrosion resistance properties. Small changes in etchant strength or etching time can result in differences in the revealed microstructure. It is also important to note that phases in the microstructure have generally been identified based on EDX analysis, along with matching their appearance and morphology to literature. Identification of crystal structures would have been a more certain method of phase identification; however this was not possible within the scope of the experimental work. The spatial resolution of EDX analysis is also highly dependent on the interaction volume of the electron beam, but is seldom less than 1 μm , and this must be considered when interpreting EDX analysis data. In the case where microstructures are complex and contain many phases in fine morphologies, it is possible that there are phases or structures that are simply too small to be seen even with high resolution SEM. The morphology, size and, quantity of the γ' phase are important topics of discussion in superalloy metallurgy, and here it must be considered that γ' is coherent with the matrix, and its appearance may change with the relative angle of the plane of cross-section to the crystallographic orientation of growth. Quantitative analysis of γ' volume fraction has not been performed in this study, therefore all statements discussing volume fraction are based solely on qualitative analysis of micrographs.

Tensile testing was performed at a certified facility, however the values of elongation and reduction in area are dependent on manual measurement of the fractured tensile samples, and thus may be susceptible to error.

4. Results

4.1 Metallography and fractography of cracking

Plain polished specimens in the light optical microscope showed defects in clear contrast. Figure 16 (a) and (b) show that specimens produced with process parameter set P1 contained a high density of cracks. Cracks were consistently oriented in the build direction, i.e. the Z-axis. Etching showed that cracks were intergranular – see Figure 16 (c). Crack dimensions were on the order of tens of microns, with the largest cracks showing dimensions close to 100 μm .

The electron micrograph in Figure 16 (d) show the appearance of one such large crack after etching. The crack is oriented roughly parallel to the build direction with a jagged appearance that follows a grain boundary. Individual dendrites can be distinguished on either side of the crack, and their varying orientation show that separation has taken place between two grains. Figure 16 (e) and (f) show the appearance of the interior faces of the crack: a clear dendritic morphology can be distinguished.

Figure 17 shows the results of fractography of the as-built high-crack density specimens. Observation of the fracture surface at low magnification - see Figure 17 (a) - shows the general appearance of the fracture surface. It is apparent that a mixed fracture took place. A number of “steps” seen on the fracture surface suggest that fracture propagated along certain crystallographic orientations [39]. Decohesion facets are plainly visible and a difference in height between different areas of the fracture surface shows that several initiation and propagation points were involved.

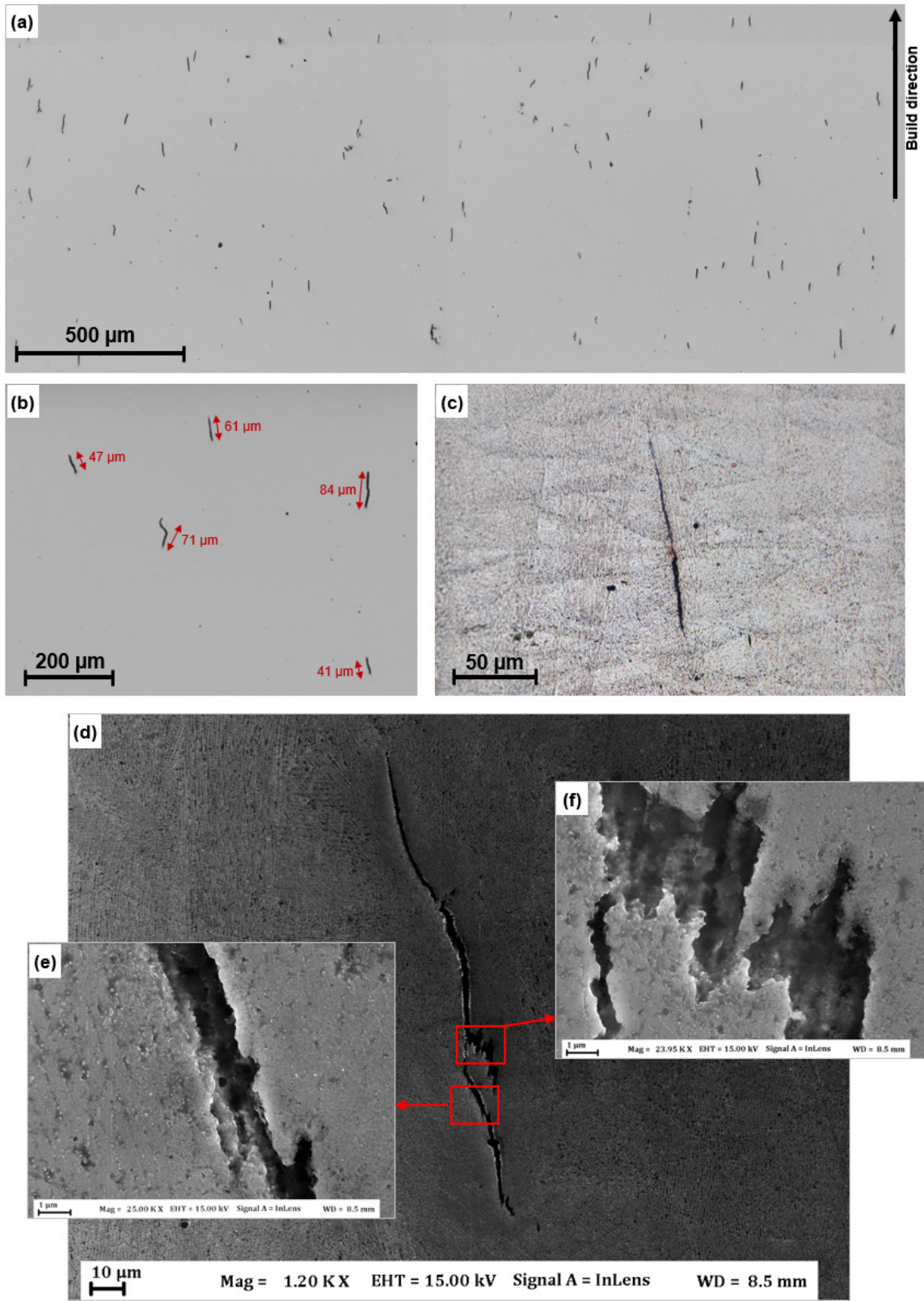


Figure 16: As-built high-crack density samples: (a) and (b) Optical micrographs of plain polished specimens; (c) Optical micrograph of typical intergranular crack, Kallings 2 etch; (d), (e), and (f) Electron micrographs showing dendritic appearance of cracks.

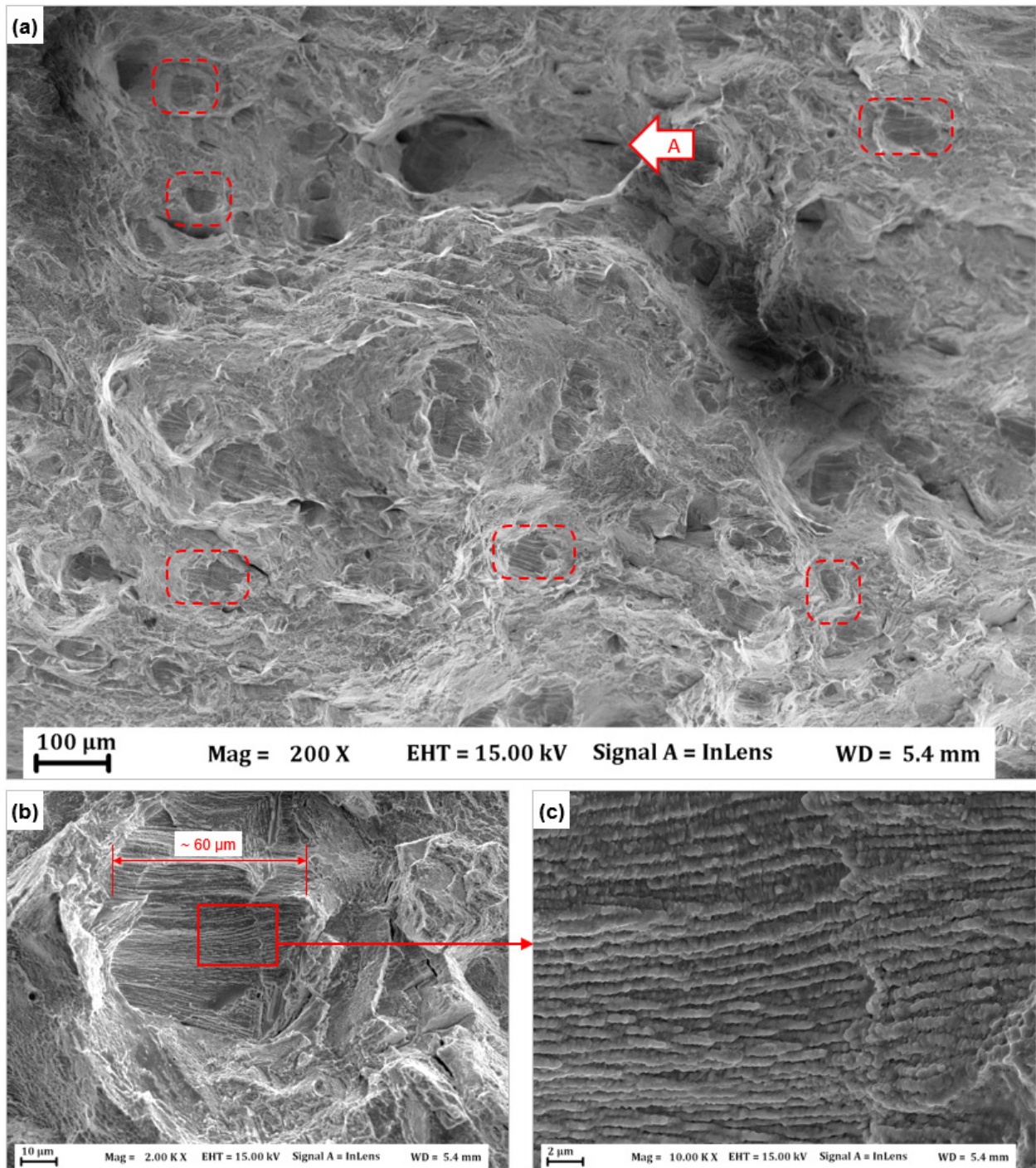


Figure 17: As-built high crack-density sample: (a) Fractograph with selected cracks in dotted outline; (b) dimensions of a selected decohesion facets; (c) high magnification micrograph showing dendritic appearance on a decohesion facet.

The most notable features of the fracture surface are highlighted with several dotted red outlines. One of these areas is shown at higher magnifications in Figure 17 (b) and (c). These are areas showing a distinctly different appearance from the rest of the fracture surface. The high magnification images show these areas to have an unmistakable dendritic morphology. The scale bar in the micrograph allows the dimensions of

these regions to be estimated as tens of microns, with the largest dimensions being around 100 μm . These dimensions are consistent with the proportions of the cracks seen in Figure 16 (a) and (b). These regions are thus identified as crack propagation facets.

The specimens built using a 20 μm layer-thickness process and understood to be completely crack-free were subjected to the same examination in order to further confirm the presence of crack propagation facets in fractography. Figure 18 (a) shows an optical micrograph of a plain polished crack-free specimen. Small circular defects are observed, which have been identified as gas pores. No cracks can be seen. Figure 18 (b) to (d) present fractographs of the crack-free tensile specimen. The fracture again appears to be mixed; Figure 18 (c) shows a much smoother fracture surface, and a higher magnification view in Figure 18 (d) shows signs of ductile fracture with evident microvoid coalescence. However, no decohesion features similar to those observed in Figure 17 can be observed.

4.2 Scheil Solidification Simulation

The non-equilibrium solidification of alloys has been simulated in literature [37], [38] using the Scheil Solidification Simulation module of Thermocalc. This can provide an insight into the extent of segregation that causes stable liquid films at temperatures far below the equilibrium solidus temperature, and the elements responsible for the stabilization of such liquid films. In any result generated using the Scheil-Gulliver model, it must be stated that the model is based on the assumptions that the liquid phase is homogenous at all times, and that no diffusion occurs in solidified material.

Results of the Scheil Simulation are shown in the software-generated graphics in Figures 19 and 20. Figure 19 shows that the equilibrium solidification of IN939 starts at approximately 1350°C and the final liquid is solidified at ~1205°C. Non-equilibrium solidification lowers the solidus temperature to ~780°C, i.e. a difference of ~240°C from equilibrium. The solidification begins with γ , and at ~1315°C the MC carbides begin to form. Precipitation of the η phase occurs at ~1205°C, at which point more than 0.8 mole fraction of the material has already solidified. The final phase to solidify is the boride M_2B .

Figure 20 shows how the elements Zr, B, and C segregate with the progression of solidification. Zirconium and Boron are only present in the alloy in concentrations of hundreds of ppm, and the simulation shows that these have a particularly strong tendency for partitioning to the liquid. Figure 20 (a) shows that during the final stages of solidification, the concentration of Zr in liquid shoots up drastically. The same is true for B, which also partitions heavily to the last liquid until it is consumed during precipitation of borides. Carbon is also pushed into the liquid during the initial stages of solidification, but is consumed in formation of carbides, and the simulation predicts that the last liquid has very minor C content compared to B and Zr.

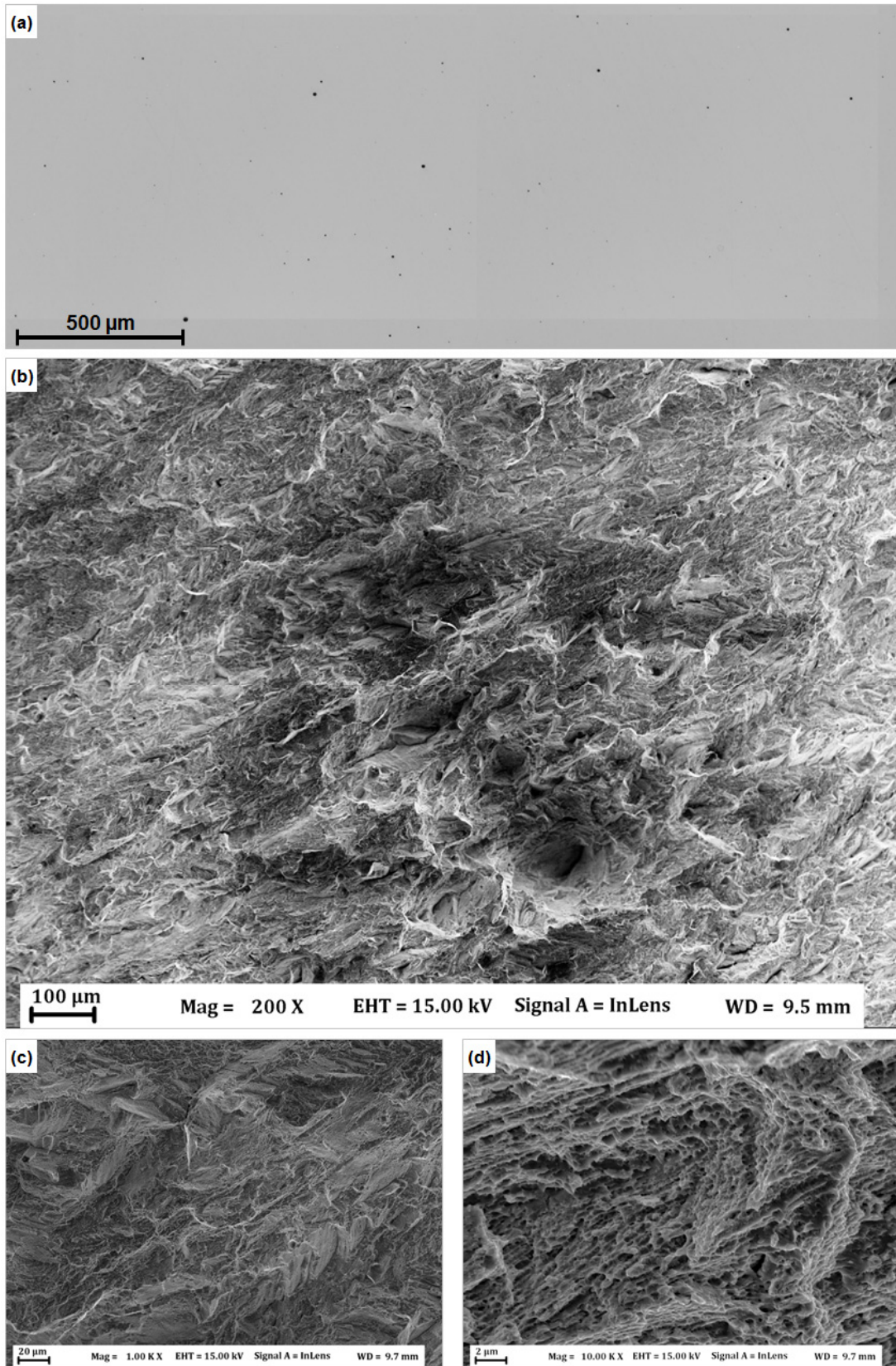


Figure 18: As built crack-free specimen from process parameter P2: (a) Optical micrograph of plain polished specimen; (b) - (d) SEM fractographs.

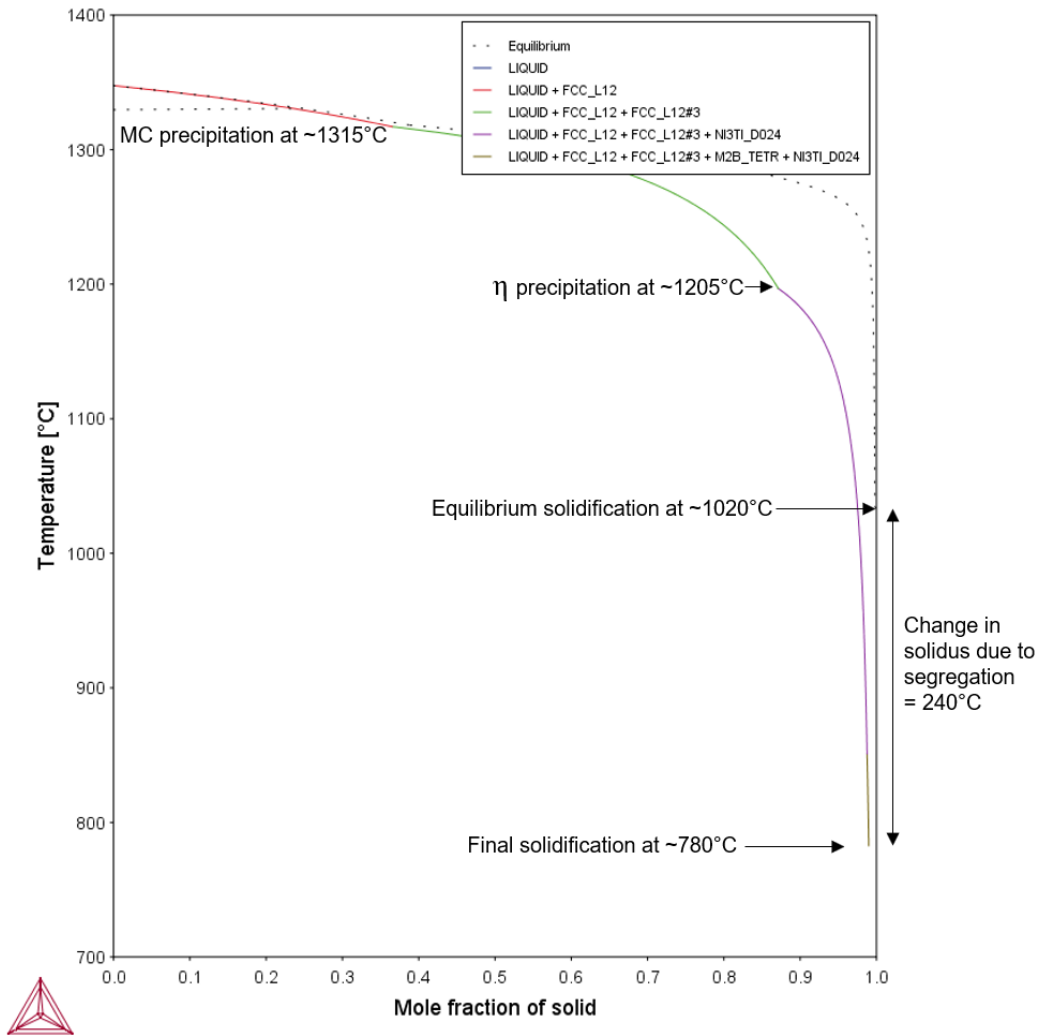


Figure 19: Scheil Solidification Simulation of IN939

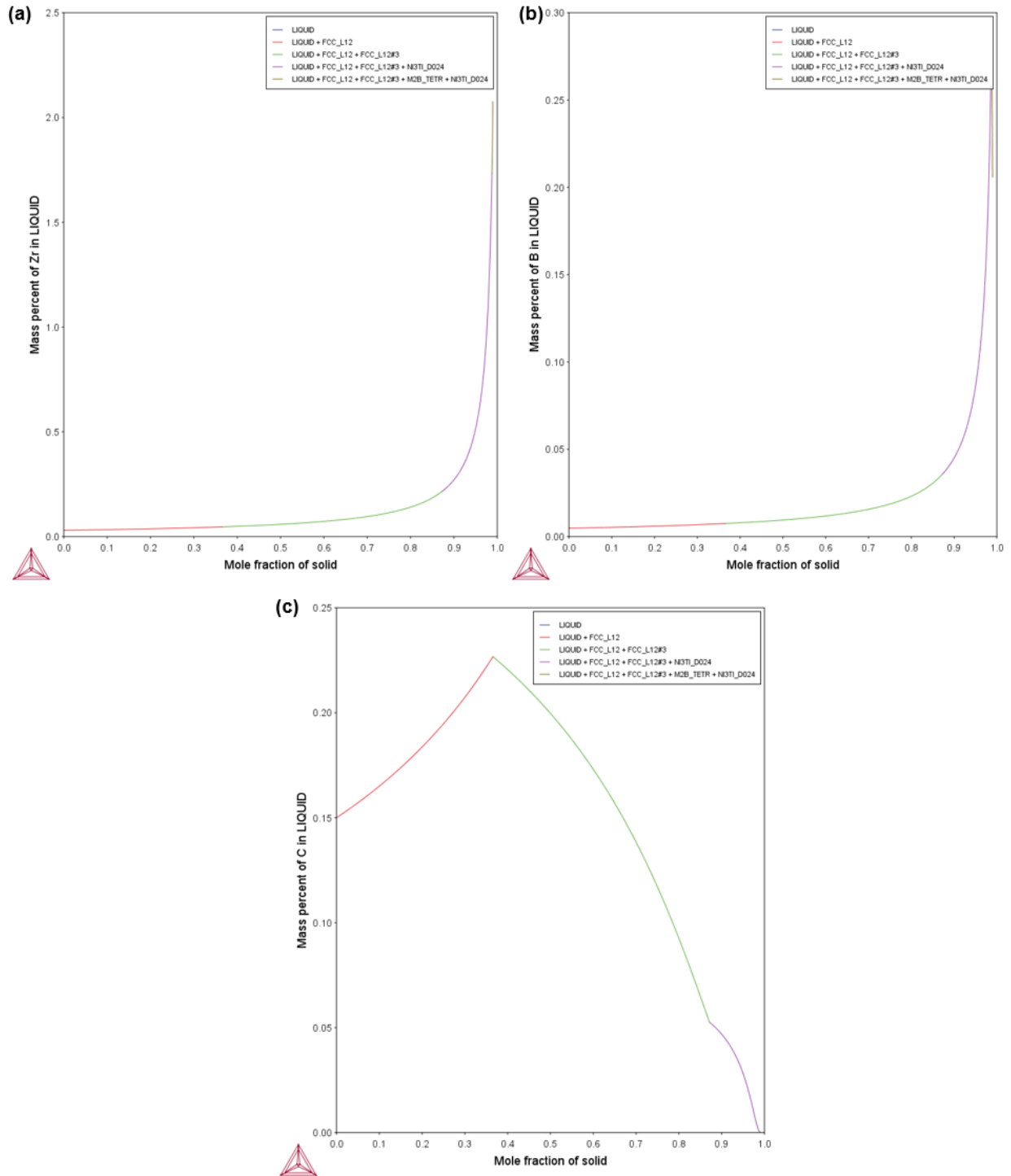


Figure 20: Segregation of selected elements to liquid phase during non-equilibrium solidification, as predicted by Scheil Solidification Simulation: (a) Zirconium; (b) Boron; (c) Carbon.

4.3 Thermal Analysis of As-Built and Standard Heat-Treated Microstructure

The DSC graphs showing heating runs for As-Built and Standard 4-Step Heat-Treated IN939 can be found in Figure 21. The DSC graphs for cooling runs are shown together in Figure 22. Complete results for thermal analysis can be found in Appendix 1.

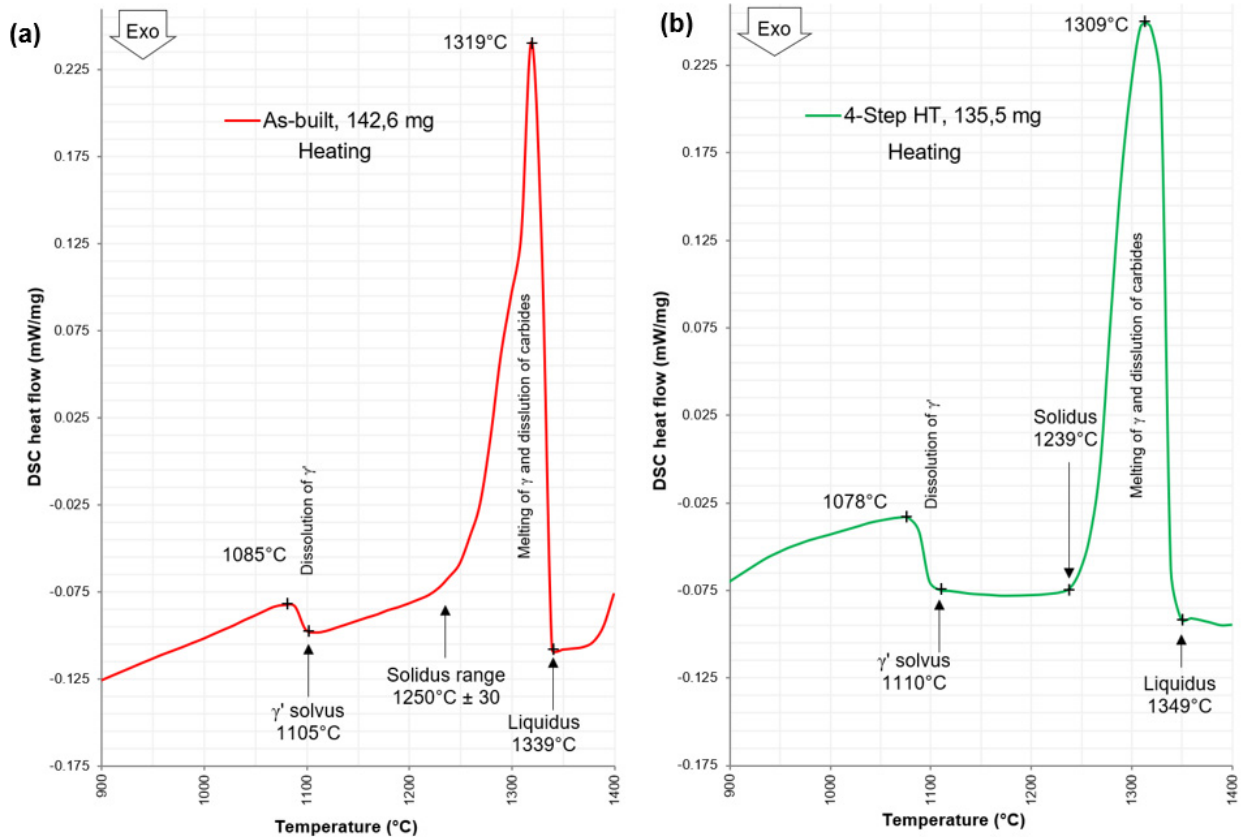


Figure 21: DSC graphs for heating runs of (a) As-Built (HT-A); (b) Standard 4-Step Heat Treated IN939 (HT-E)

The As-Built (HT-A) material exhibits a notable change in heat flow between 1085°C and 1105°C which is explained by dissolution of γ' into the γ matrix. A similar range for this transformation has been reported by Gibbons and Stickler [7], and by Formenti et al [25]. The same drastic change in heat flow is observed in the HT-E sample over a slightly wider temperature range (1078°C to 1110°C). However the magnitude of the change is greater. This may be explained by the greater volume fraction of γ' precipitates that would be expected in the aged material.

Following the dissolution of γ' there is a gradual change in heat flow observed in the As-Built sample in the 1220°C to 1280°C range. This appears to be related to the beginning of melting of the γ matrix. The shape of the peak indicates complex shape and hence overlapping of two peaks, connected to melting of two phases. A steeper gradient in the same temperature range for the 4-Step Heat Treated sample enables

the melting temperature to be ascertained as 1239°C. Both Formenti et al and Gibbons et al have quoted the solidus temperature as 1235°C [7], [25] which is largely consistent with Figure 21.

The peak labelled as “melting and dissolution of carbides” can clearly be seen to be composed of two separate peaks in the DSC graph for As-Built material. It appears to indicate that dissolution of carbides occurs close to ~1300°C, whereas melting of the matrix continues up until 1339°C. The corresponding peak in the 4-Step Heat-Treated DSC graph, though better defined, cannot be deconvoluted into separate peaks for matrix melting and carbide dissolution. This may suggest that the carbides melt over a larger temperature range than in the As-built material. This is consistent with the understanding that as-built (or as-cast) material contains only MC-type carbides, while aged material contains more complex $M_{23}C_6$ type carbides as well. The liquidus temperatures have been determined as 1339°C and 1349°C for As-Built and 4-Step Heat-Treated IN939 respectively, and are very close to the value of ~1340°C reported in literature [7], [25], [40].

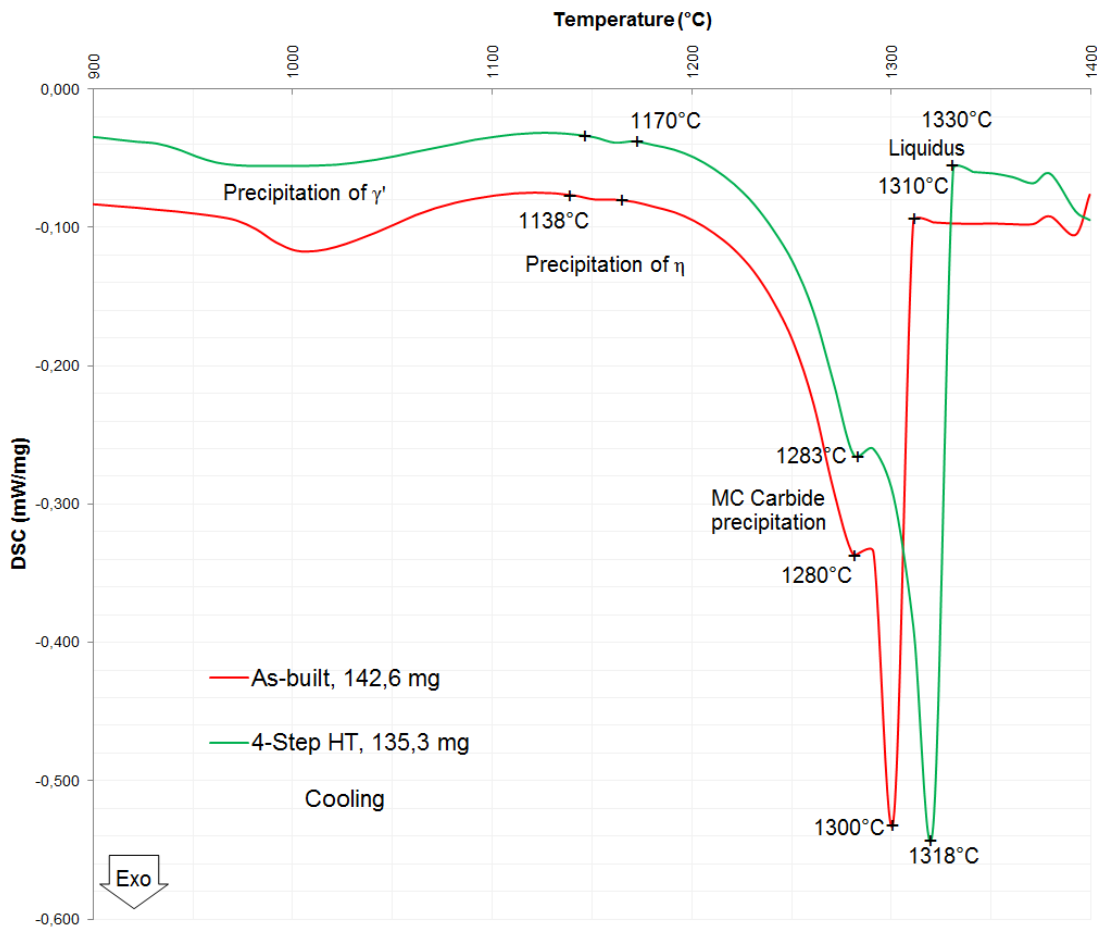


Figure 22: DSC graph for cooling run of As-Built (HT-A) and 4-Step Heat Treated (HT-E) IN939

The cooling DSC graphs represented in Figure 22 provide a clearer temperature range for precipitation of the MC type carbides. A very small exothermic peak is also noticeable in Figure 22, which is found between 1138°C and 1170° for both samples. This can only be attributed to the formation of the η -phase. Gibbons et al have quoted the η phase solvus temperature to be 1145°C [7].

4.4 Phase Transformations in IN939 – JMatPro Simulation

The phase transformation temperatures and phase composition as a function of temperature for IN939, as predicted by the JMatPro 9.1.2 step temperature programme, are presented in Figure 23.

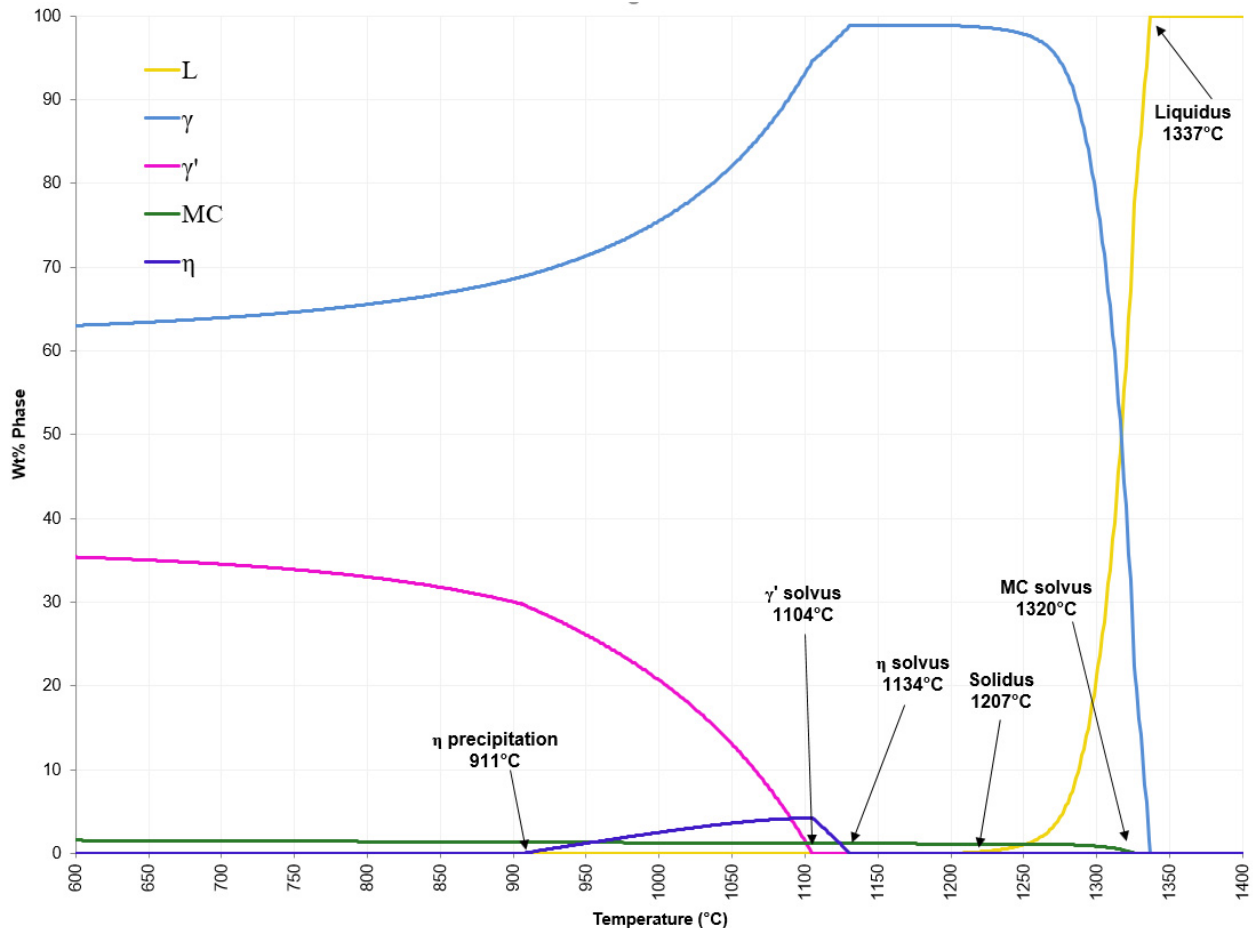


Figure 23: JMatPro Step-Temperature programme prediction of equilibrium phases in IN939

The simulation shows a fraction of 35 wt% of γ' phase, which is stable up until 1104°C, when it is completely dissolved. The fraction of γ' in the alloy is relatively stable above 30% until 911°C, when η phase is precipitated. The solvus temperature for η is predicted to be 1134°C – within the range suggested by DSC results and literature. Solvus for MC carbides is predicted as 1320°C. The matrix solidus and liquidus temperatures are predicted to be 1207°C and 1337°C respectively.

4.5 Microstructures of As-Built and Heat Treated IN939 in Metallography

4.5.1 HT-A: As-Built

The optical micrographs of plain polished ZY and XY cross sections shown in Figure 24 illustrate that the DMLS-processed IN939 is virtually defect free. Defect percentages in all samples were consistently in the range of 0.01 to 0.03%. Lack-of-fusion defects, where encountered were examined in microscopy, and examples are shown in Figure 24 (c) and (d). The lack of fusion defect shown in Figure 24 (c) can be seen as incomplete penetration of a powder particle in a particular layer of the build. Likely reasons for incomplete penetration are defocusing of the laser beam caused by interaction with smoke or spatter, oxidation of the powder particle, or oxidation of the underlying layer. An example of oxide causing poor bonding between layers is shown in Figure 24 (d). The oxide was investigated by EDX point analysis and proved to be aluminium oxide, as shown by Spectrum 9. The result of point analysis at the matrix is shown in Spectrum 10 for comparison purposes.

Figure 24 (e) shows a second phase particle observed in the as built structure, and subsequently throughout all heat treatment stages. In optical microscopy the particle has a golden-orange appearance. EDX analysis as displayed in the spectrum next to the electron micrograph shows that this inclusion is composed of Ti and N and is thus identified as a titanium-nitride TiN. Such inclusions have been reported by Lund and Wagner in their excellent monograph on the identification of microconstituents in superalloys [41]. This inclusion is formed during melt processing of the powder feedstock and apparently does not melt during DMLS processing due to its extremely high melting point of $\sim 2930^{\circ}\text{C}$.

The microstructure of As-Built samples is shown in the optical and electron micrographs in Figure 25. The light optical micrograph in Figure 25 (a) shows a cross section parallel to the build direction, in which elongated columnar grains can clearly be seen extending from top to bottom. The width of a single grain can be estimated to be in the range of 50 to 150 μm , while the height may be as long as several millimetres. The etch also reveals the characteristic pattern of closely spaced and overlapping melt pools that is familiar in as-built PBF microstructures [36], [37].

Figure 25 (b) shows the XY cross section – perpendicular to the building direction – where the cross hatches in a single layer of the build can be discerned as a pattern of impressions diagonally across the micrograph. The grains appear to be more equiaxed, with grain sizes around 50 μm . However, some grains that are much smaller can also be seen, and these are found where a columnar grain initiates or terminates.

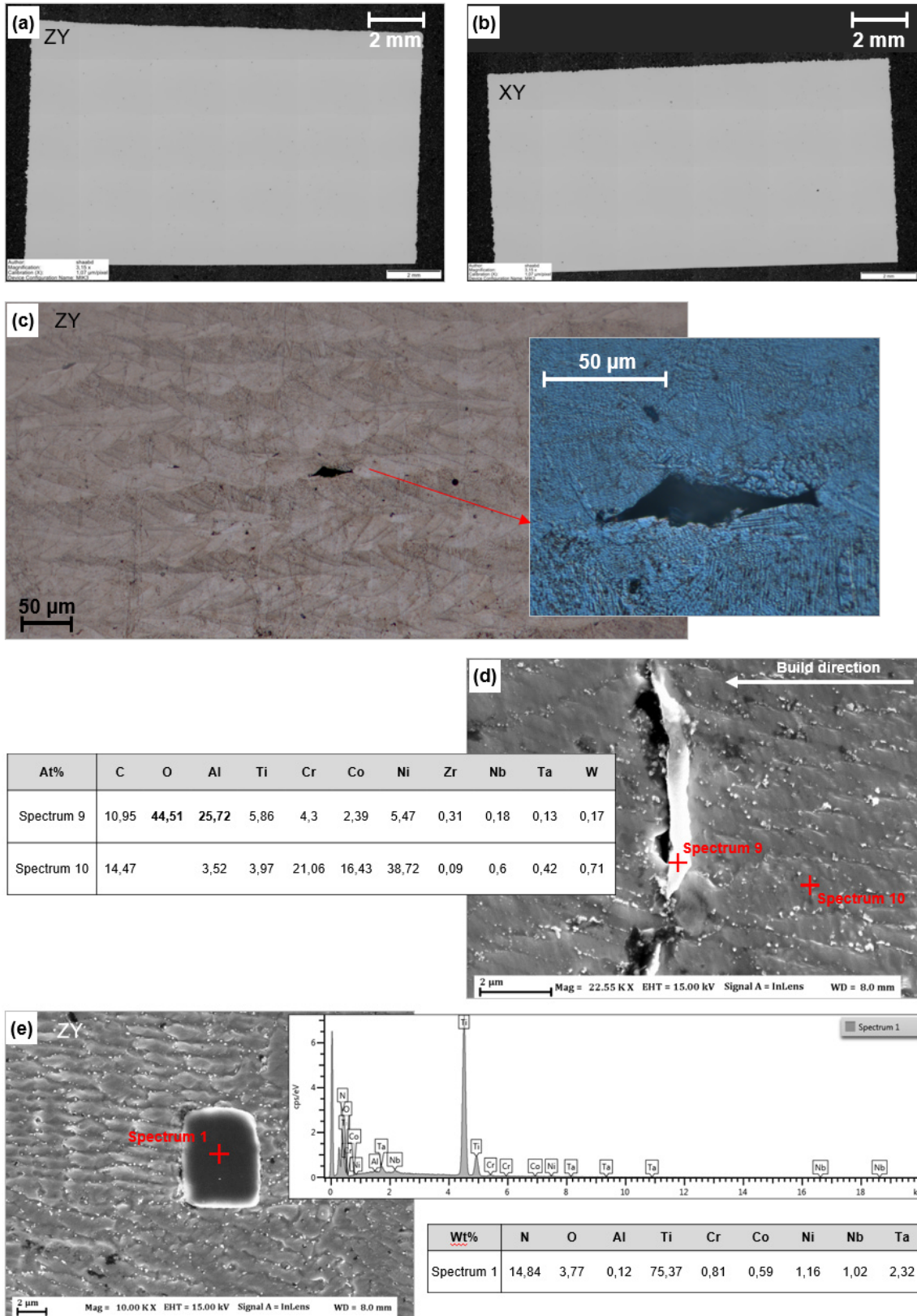


Figure 24: (a) and (b) Optical micrographs showing largely defect-free DMLS-processed IN939; (c) and (d) Lack of Fusion defects; (e) a second phase particle identified as a Titanium Nitride

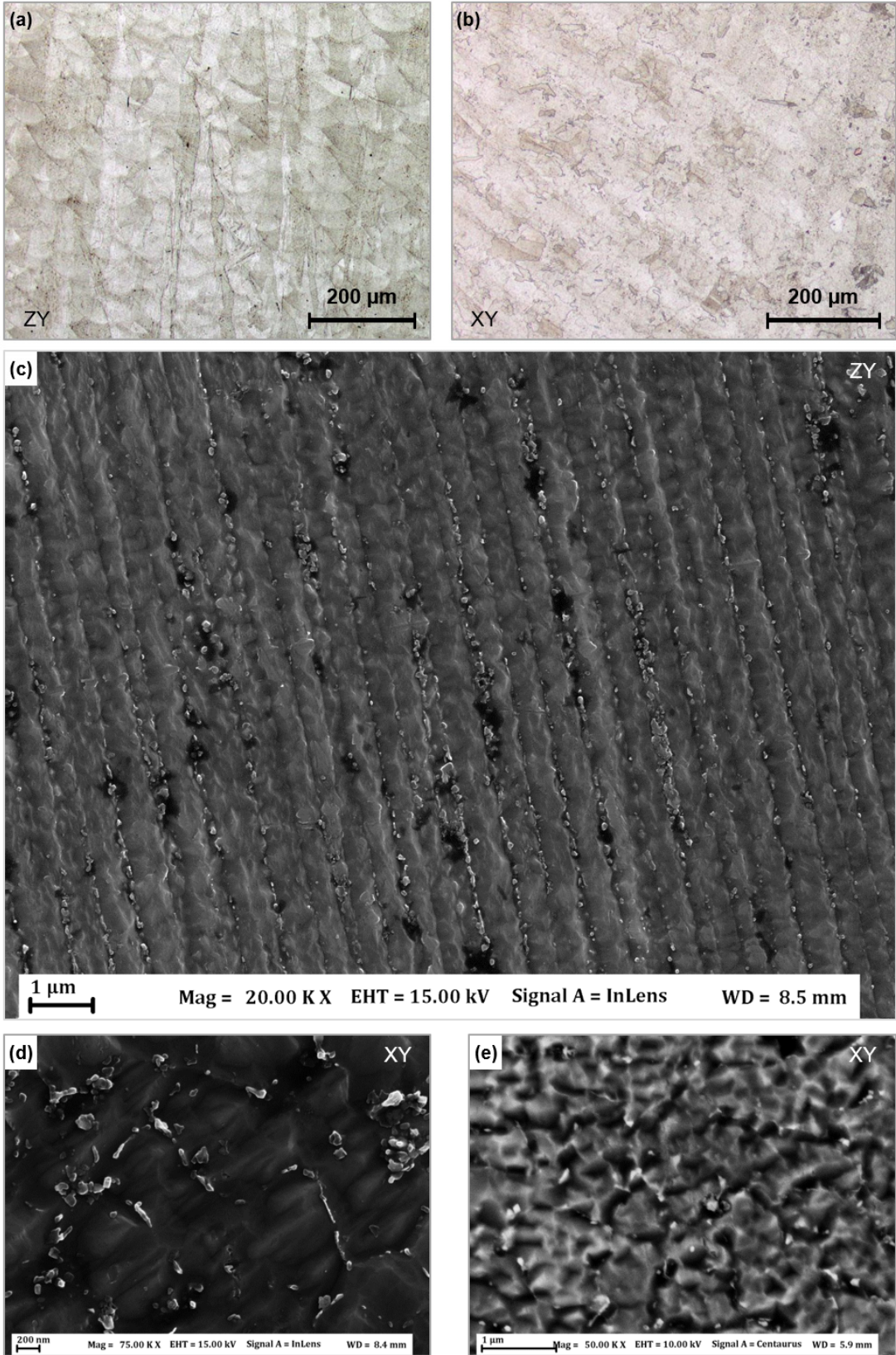


Figure 25: Microstructure of As-Built IN939, HT-A: (a) and (b) Optical Micrographs showing ZY and XY orientations respectively, Kallings 2 etch; (c) to (e) Electron Micrographs, orientation of cross section inlaid.

Figure 25 (c) shows the fine dendritic solidification structure observed in electron microscopy. The individual dendrite arms can be seen stretching vertically across the image. Dendrite arm spacing is smaller than 1 μm . The dendrite cores (γ phase) are seen to be free from any precipitates, whereas the inter-dendritic regions have a regular distribution of particles. Based on the known solidification sequence [25] and DSC analysis, these particles are understood to be MC-type carbides. Figure 25 (d) shows a higher magnification view of these particles: two morphologies can be seen: a rounded “globular” morphology [41] with sides of around 100 nm or less; and an elongated shape, with major length around 200 to 300 nm. As described by Formenti et al, the morphology is dependant on local solidification conditions [25], and may also vary depending on the composition (different M-elements) in the carbide phase. The BSE image in Figure 25 (e) shows brighter contrast in these inter-dendritic regions, which corresponds to the heavier elements of which MC carbides are typically composed.

Due to their fine size, verification of the composition of any individual particle was not possible using EDX analysis as the interaction volume of the electron beam far exceeded the size of the particle. However, regions of samples which were not re-melted (top layers) could be found where denser precipitation was observed, and here the larger volume of particles clumped together allowed detection by EDX. Figure 26 (a) shows one such example. Spectrum 1 in the figure is on an accumulation of particles, while Spectrum 2 is on a dendrite core. In comparison to Spectrum 2, Spectrum 1 shows a higher concentration of Ti, Nb, and Ta, which are commonly reported as constituents in MC carbides [7], [25], [42]. Spectrum 1 also shows lower amounts of Ni, Co, and Cr than Spectrum 2; these elements are known to partition to the γ -phase. The same trend can be seen in Figure 26 (b), where Spectrum 14 and 15 are at particle clusters, and Spectrum 16 and 17 are at dendrite cores. The relative orientations of the plane of cross section and the dendrite at this location were favourable for fitting the desired area of analysis into the electron beam interaction volume. The accelerating voltage of the electron gun was also lowered to 5 kV in order to reduce the interaction volume. A more defined difference between the dendrite cores and particles can be seen here: high carbon contents of 41 and 43 at.% were detected in the particles, versus 6 at.% in the cores. Similarly, Ti contents in cores were around 2 at.% versus 8 and 12 at.% in the particles. This shows that the inter-dendritic regions consist of carbide particles which contain mainly Ti, as well and Nb and Ta, while the dendrite cores consist of mainly Ni, Co, and Cr.

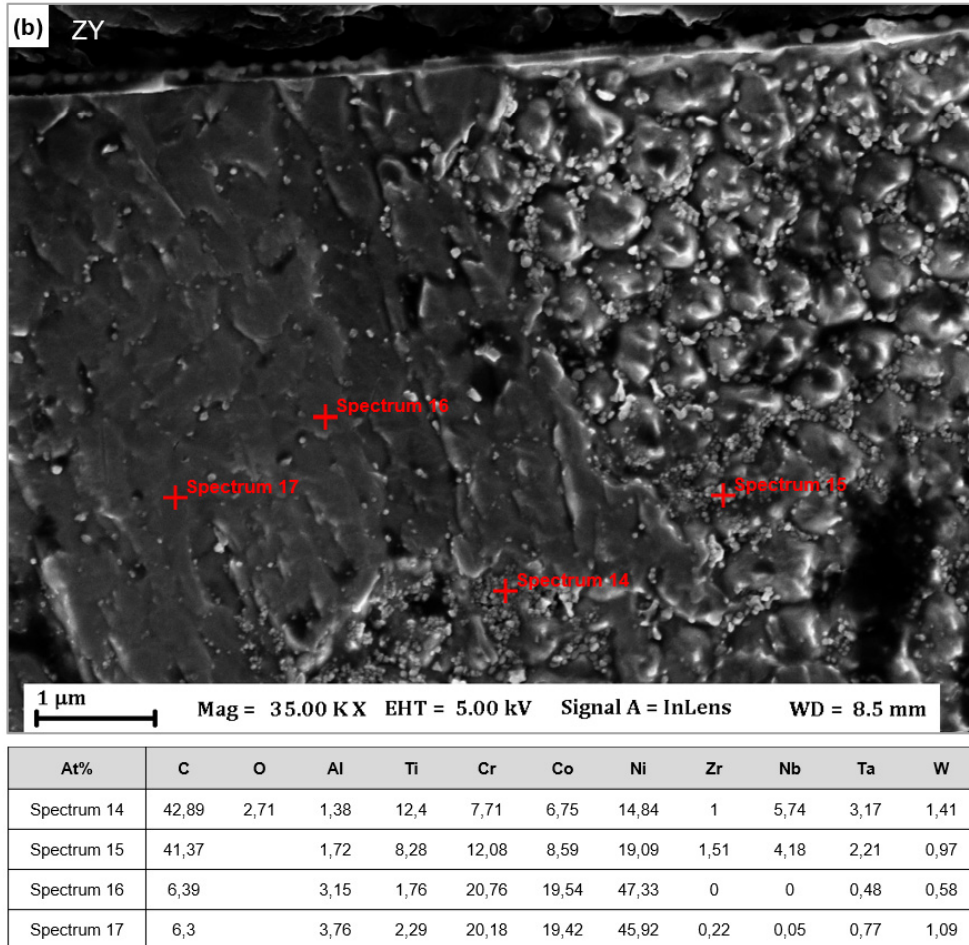
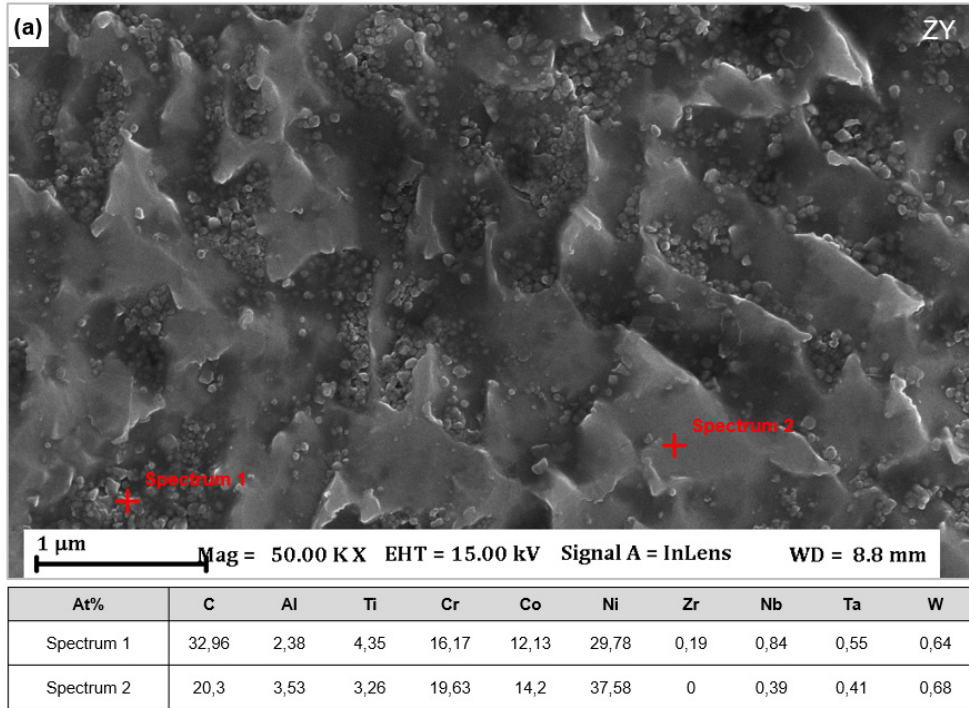


Figure 26: EDX analysis of fine particles in As-Built microstructure

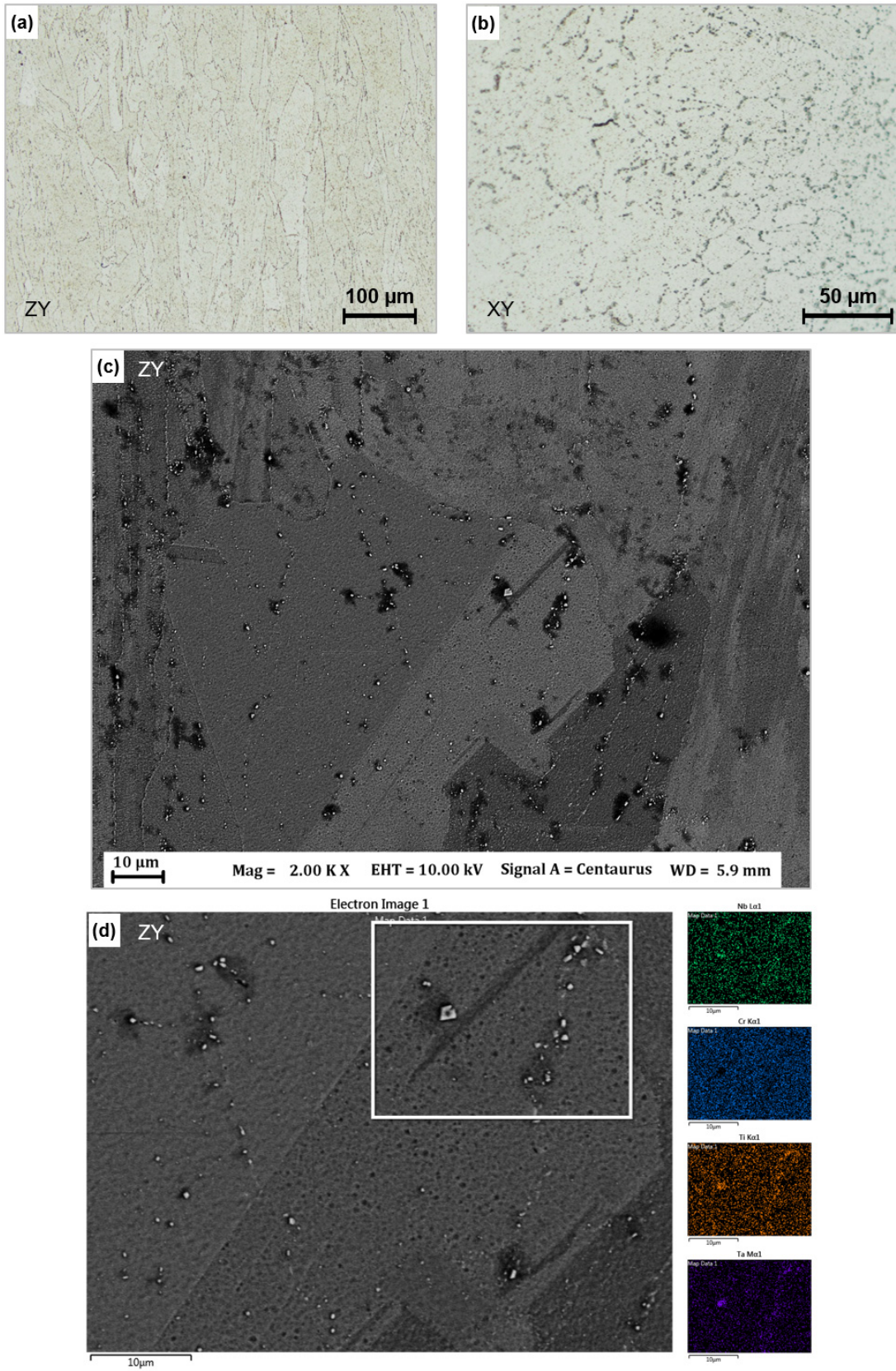


Figure 27: Microstructure of IN939 Solution Treated, 4/1160, HT-B: (a) and (b) Optical Micrographs showing ZY and XY orientations respectively, Kallings 2 etch; (c) grain structure in BSE image (d) EDX mapping of carbide particles.

4.5.2 HT-B: Solution Treated 4 hrs / 1160°C

The microstructure after standard solution heat treatment, i.e. 4 hours at 1160°C followed by forced air cooling, is shown in Figure 27. The light optical micrographs in Figure 27 (a) and (b) show that the melt pool and hatch patterns observed in the as-built specimens are no longer found. The grain structure is now more apparent, and this consists of columnar grains with carbide particles at grain boundaries. The BSE micrograph in Figure 27 (c) shows that carbide particles are not only present at the grain boundaries, but also within grains. The differing orientation of the grains in the micrograph can be seen as different shades of grayscale due to the BSE channelling contrast. The extreme left side of this micrograph shows a columnar grain where some remnants of the dendritic solidification structure can still be seen. In the centre of the micrograph, a recrystallized region of the grain structure can be seen. This shows that even after only 4 hours at elevated temperature, the fine solidification structure has partially recrystallized into equiaxed grains. It must be noted, however, that recrystallized grains were not a common observation within the microstructure. The carbides within the individual recrystallized grains mark the prior grain boundaries. Also notable is the absence of any incipient melted regions as predicted by Jahangiri et al [40].

A region within the recrystallized grain from Figure 27 (c) is shown at higher magnification in Figure 27 (d). The carbides at prior grain boundaries were examined by EDX mapping. Despite their small size, some compositional information can be obtained. Similar to the as-built microstructure, these carbides are rich in Ti, Ta, and Nb. Cr was observed in the matrix, but none was detected at the location of the carbide particles.

Imaging at high magnification revealed a bi-modal distribution of γ' precipitates. Figure 28 (a) shows the particles as irregular shaped ~ 100 nm size precipitates distributed in the matrix. Figure 28 (b) shows precipitates of < 20 nm size between the larger precipitates. The difference between γ' precipitates and MC particles is not immediately apparent in SE imaging, as both particles have similar size. The BSE image in Figure 28 (c) shows the γ' phase in bright contrast against a darker matrix, and carbide particles appear even brighter. As shown by the inlaid red arrow, MC particles also appear to have clearly defined facets along crystallographic planes. The brighter contrast of γ' precipitates compared to the matrix may be caused by the concentration of heavy elements such as Ta and Nb in γ' .

Fine ~ 20 nm sized γ' after solution treated has been described by Gibbons et al [7]. However, such a bimodal structure with larger precipitates has not been reported at this stage of heat treatment.

As no plate-like phase was observed, it is understood that no significant η -phase is present in the microstructure at this stage of the heat treatment.

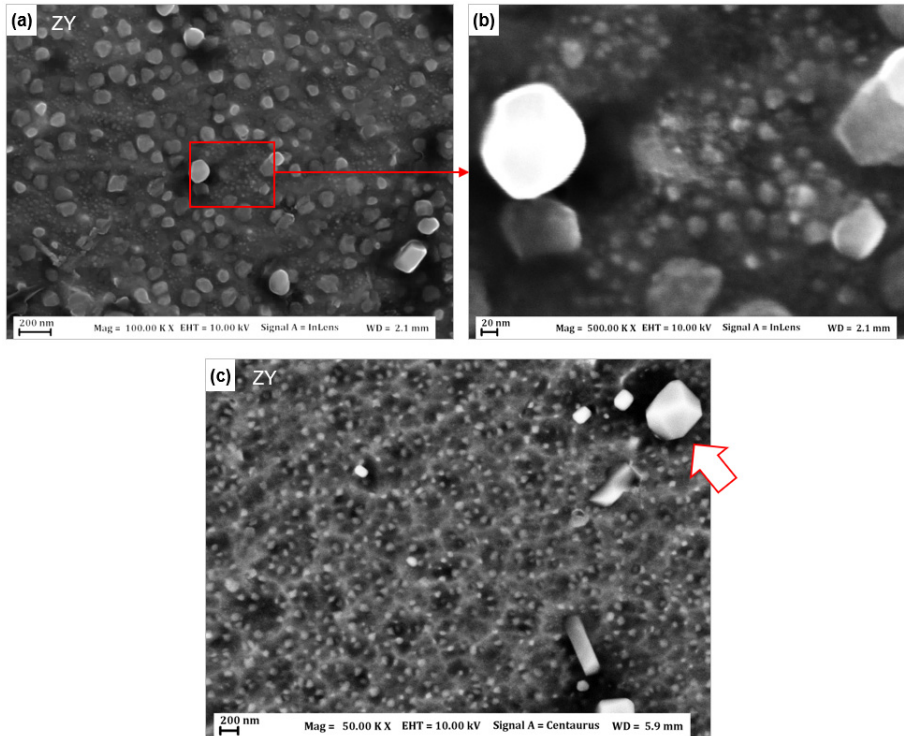


Figure 28: Precipitates in IN939 Solution Treated, 4/1160, HT-B: (a) and (b) γ' precipitates imaged with SE detector; (c) carbides and γ' imaged with BSE detector

4.5.3 HT-C: 4 hrs / 1160°C + 6 hrs / 1000°C

The effect of the first ageing step on the solutionized microstructure is presented in Figure 29. The figure shows carbide particles along grain boundaries and γ / γ' visible inside the grains. Carbide particles with sizes larger than 1 μm can commonly be seen here, which was not the case in microstructures from HT-B. Increased diffusivity at the ageing temperature can be expected to cause growth of carbide phases. Chemistry of these carbides was examined by EDX point analysis. Spectrum 5 and Spectrum 7 shown in Figure 29 are at larger sized carbide particles, and Spectrum 10 is at the matrix. Spectrum 10 shows prominent peaks of Ni, Co, and Cr – the primary components in the alloy. Spectrum 7 shows much smaller peaks of these three elements, and relatively high counts of Ta, Ti and Nb. Based on composition, this particle can still be expected to be an MC-type carbide. Spectrum 5 also shows high counts of Ti, Ta, and Nb, but these are lower compared to the particle analyzed in Spectrum 7. The relatively higher Cr peak suggests that this carbide may be undergoing transition to the M_{23}C_6 type carbide. Alternatively, MC type carbides have also been reported to contain small amounts of Cr, as described by Delargy et al [43].

The distribution and sizes of γ' precipitates after the first ageing step in the standard 4 step heat treatment are shown in Figure 30. The largest fraction of precipitates is of those of sizes between 150 and 200 nm. An example is shown by the arrow B in Figure 30. A smaller size of precipitates is also seen. These have

diameters in the range of 50 to 100 nm – see arrow A in Figure 30. The morphology of precipitates is closer to spherical than cubical.

Note that the W peaks that are auto-identified by the EDX software have been ignored, since these overlap the Ta peaks in the energy axis. Furthermore, W has not been shown to partition strongly to either dendritic or inter-dendritic region during solidification, nor play a major role in precipitation of carbides or γ' [7], [25], [43].

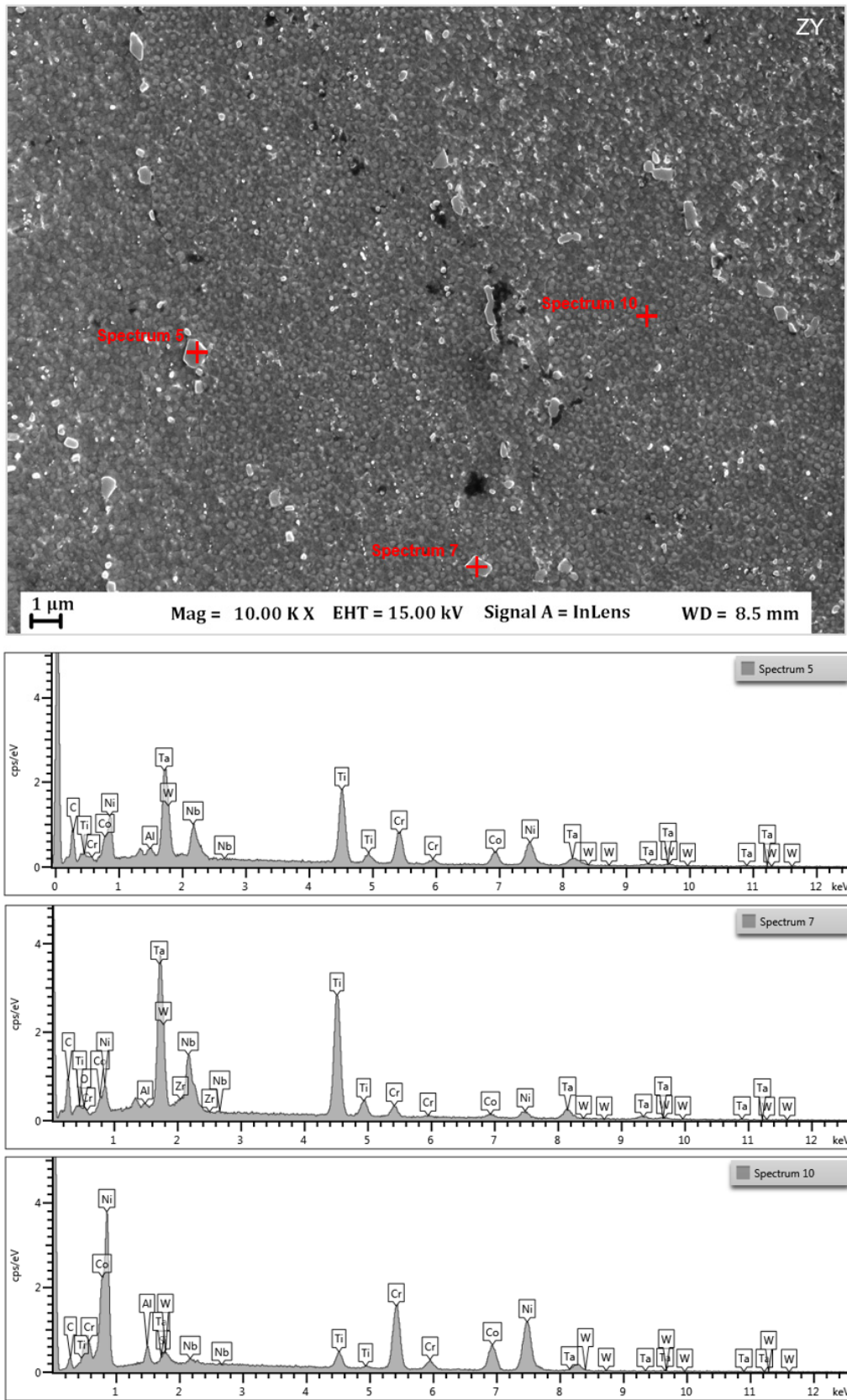


Figure 29: Microstructure and EDX analysis spectra of IN939 after solutionizing and one step ageing HT-C

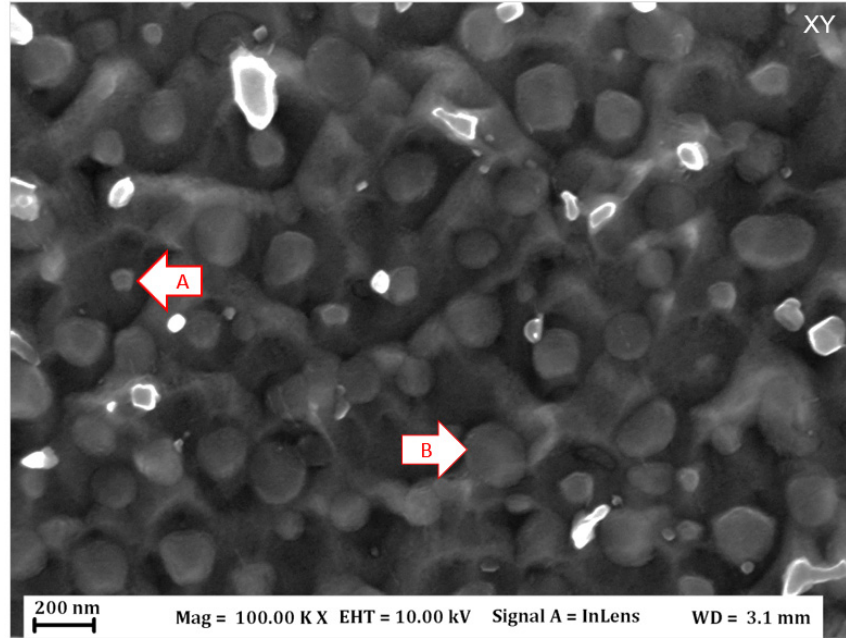


Figure 30: Appearance of γ' precipitates after 6 hrs / 1000°C step of the 4-Step Heat Treatment

4.5.4 HT-D: 4 hrs / 1160°C + 6 hrs / 1000°C + 24 hrs / 900°C

The microstructure of DMLS-manufactured IN939 after the third step of the standard 4-step heat treatment is shown in Figure 31. The BSE image in Figure 31 (a) shows that there is a difference in contrast between the larger and smaller grain boundary particles. These particles, which have in previous results been shown to be Ta, Ti, and Nb-rich MC-type carbides, were analyzed by EDX analysis and the resulting spectra are shown in the figure. Spectrum 21 and Spectrum 23 are at particles with larger size and darker contrast, and Spectrum 24 is at a smaller carbide particle.

Spectrum 21 and Spectrum 23 show very similar results: high peaks of Cr are seen, suggesting that these particles have been transformed to $M_{23}C_6$ type carbides. This carbide is known to be rich in chromium [7], [25], [43]. Spectrum 23 shows peaks of Ni and Co as well, and this is most likely due to the electron beam interaction volume extending into the matrix. The reaction of MC type carbides with the γ matrix to form $M_{23}C_6$ type carbides has been described by several authors [16] as follows:



A difference in contrast can also be noted between the outside edges and the interior of these $M_{23}C_6$ type carbides; the exterior has a lighter contrast – and these may be areas where the heavier elements found in MC type carbides have not completely been replaced by chromium.

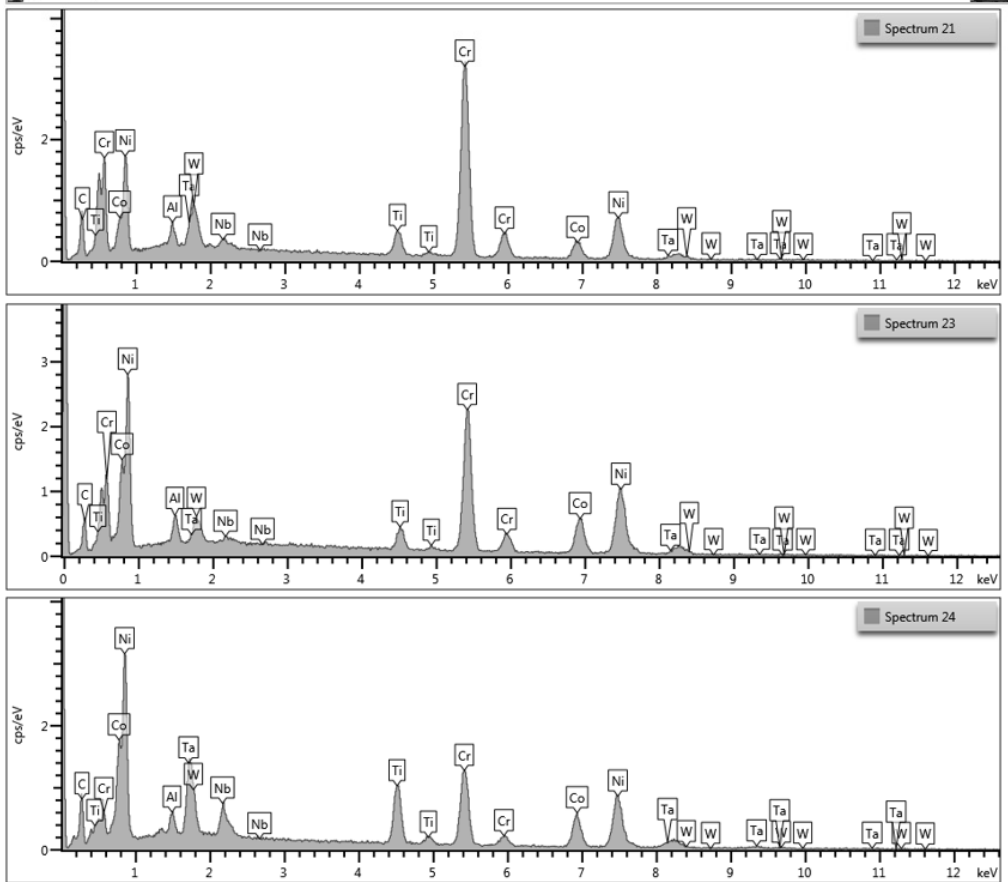
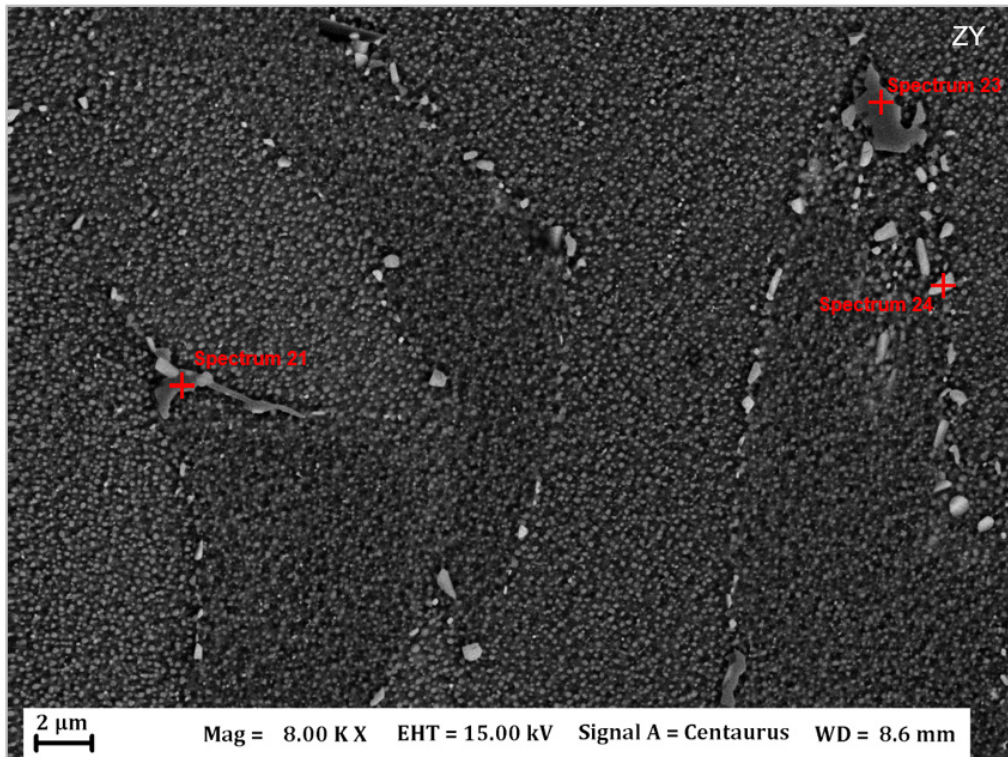


Figure 31: Microstructure after HT-D: 4/1160 + 6/1000 + 24/900, showing EDX spectra

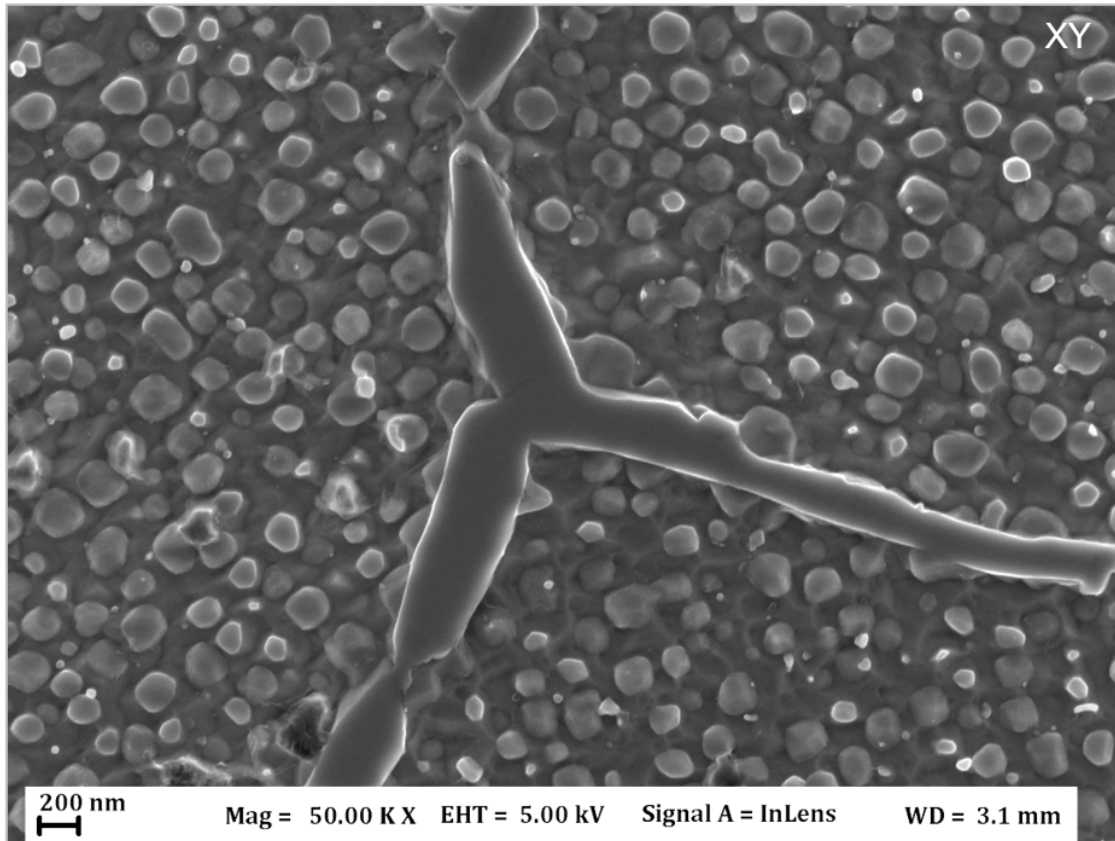


Figure 32: Morphology and distribution of γ' precipitates in microstructure after HT-D : 4/1160 + 6/1000 + 24/900

Spectrum 24 in Figure 31 represents EDX point analysis at an MC-carbide particle, and shows prominent peaks of Ni, Co, and Cr. However, when compared to the Spectrum obtained from the matrix (see Spectrum 10 in Figure 29) the peaks of Ti, Ta, and Nb counts appear to be relatively high, suggesting that the particle is an MC-type carbide. The Ni, Co, and Cr peaks are probably due to large interaction volume relative to the size of the particle.

The $M_{23}C_6$ -type carbides have more varied morphology than the MC-type, and are mostly observed at grain boundary triple points. As grain boundary triple points are high diffusivity paths, MC-type carbides at grain boundary triple points would be more likely to complete the transformation to $M_{23}C_6$ types. The observation by Gibbons et al of precipitation of $M_{23}C_6$ carbides at grain boundaries in “strings of discrete particles” [7] was not strictly seen.

Figure 32 shows the γ' morphology and distribution around an $M_{23}C_6$ carbide at a grain boundary triple point. Individual γ' particles can be observed at very close proximity to the $M_{23}C_6$ carbide, which should be expected if the transformation occurs according to the reaction described by Equation 2.

Since γ' is a coherent precipitate and thus is oriented along crystallographic planes of the γ matrix, its appearance during microscopy observation will vary depending on the intersection of the plane of cross

section with different grains. This effect can be observed in the different grains seen at the left, top-right, and bottom-right of Figure 32. Precipitation appears to be more dense in the grains on the left of the micrograph, and the morphology appears more cuboidal. The grain at the bottom-right shows sparser precipitation. It can therefore be difficult to make confident observations about volume fraction (and to a lesser extent morphology) of γ' based solely on qualitative micrographs in polycrystalline specimens. However, when compared to the micrographs showing prior heat treatment conditions, the size of γ' precipitates is clearly larger (~200 nm) with a reduced volume fraction of precipitates under 100 nm. The more cubic morphology is also plainly evident.

4.5.5 HT-E: 4 hrs / 1160°C + 6 hrs / 1000°C + 24 hrs / 900°C + 16 hrs / 700°C

The microstructure of DMLS IN939 after the final stage of the 4-step heat treatment is shown in Figure 33. The grain boundaries are consistently decorated by MC carbides (arrow A), and the $M_{23}C_6$ carbides (arrow B), which can be recognized by darker contrast, are mostly observed at grain boundary triple points. A notable difference from the solutionized microstructure is that large carbides within the grains are no longer seen. The absence of any continuous intergranular carbides with a film morphology is also notable. The channeling contrast obtained in BSE imaging shows that within the larger grains defined by carbides, there are subgrains which follow the dendritic orientations of the original solidification structure.

The size and morphology of γ' precipitates is shown in Figure 33 (b) and (c). A dense precipitation and sizes around 100 to 200 nm are observed. This agrees with the 150 ± 20 nm size reported by Gibbons et al [7]. However, as shown by Figure 33 (c), the bimodal distribution reported in the same publication is not observed. This may be simply due to imaging limitations, however there is a greater likelihood that these smaller ~20 nm sized particles are not precipitated in the microstructure. Note also the absence of any plate-like phase, suggesting that the η -phase does not exist in this microstructure.

4.5.6 HT-F: 4 hrs / 1160°C + 16 hrs / 845°C

The microstructure resulting from the simple two stage heat treatment HT-F is shown in Figure 34. Since this treatment involved only 20 hours at temperature compared to 50 hours for the standard 4-step heat treatment, a markedly less-homogenized microstructure is developed. MC-type carbides – as shown by the EDX mapping results in Figure 34 (a)– are found both at grain boundaries and within grains. The faint Zr indication observed in the mapping is not unexpected, as Zr has been known to replace C in MC carbides [7] – see Table 3. A dense precipitation of ~100 nm sized γ' particles can be seen in Figure 34 (b). As anticipated, finer ~20 nm precipitates are not observed as they are expected to dissolve above 820°C [7].

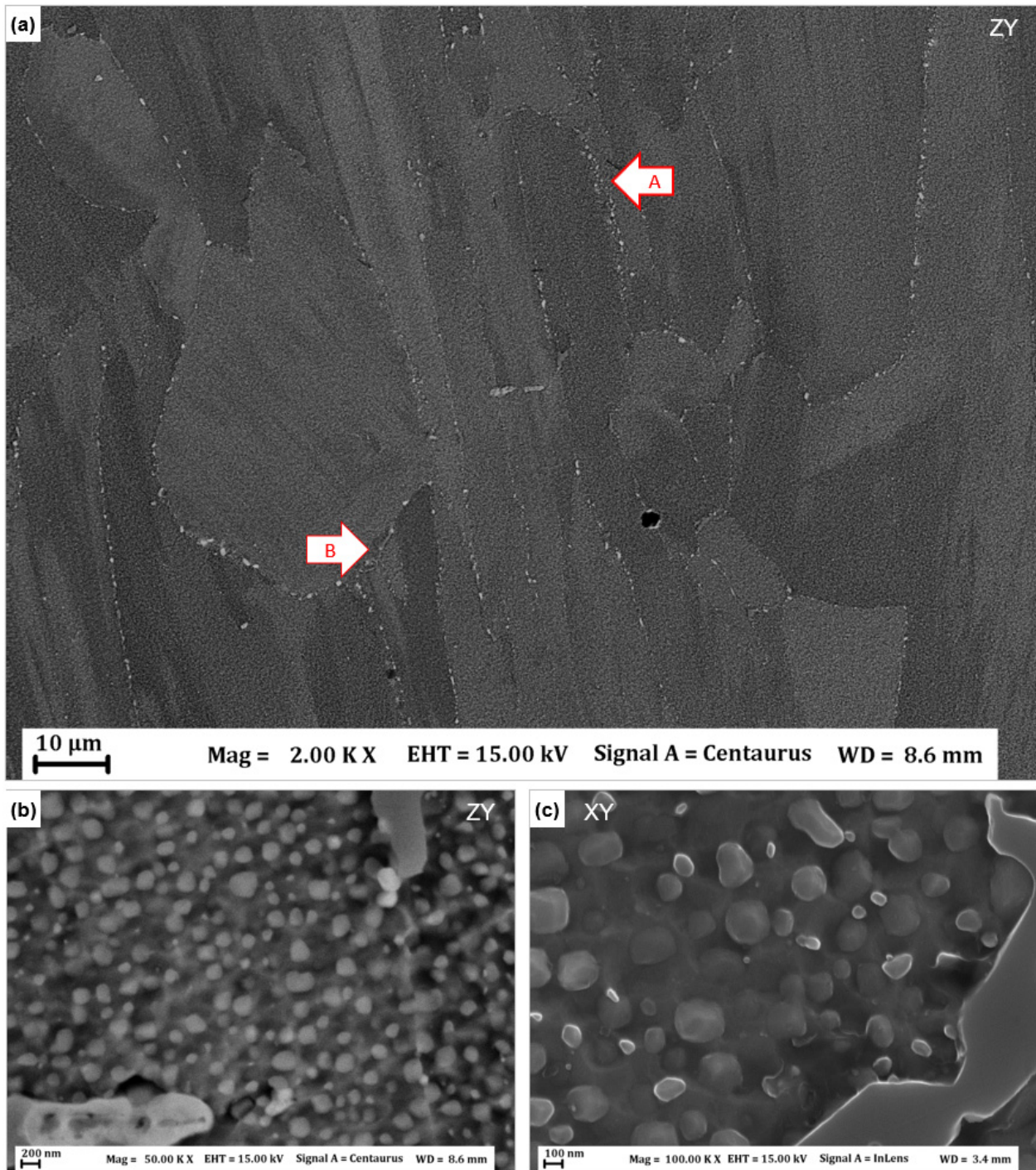


Figure 33: HT-E: Microstructure after complete 4-step heat treatment: 4 / 1160 + 6 / 1000 + 24 / 900 + 16 / 700

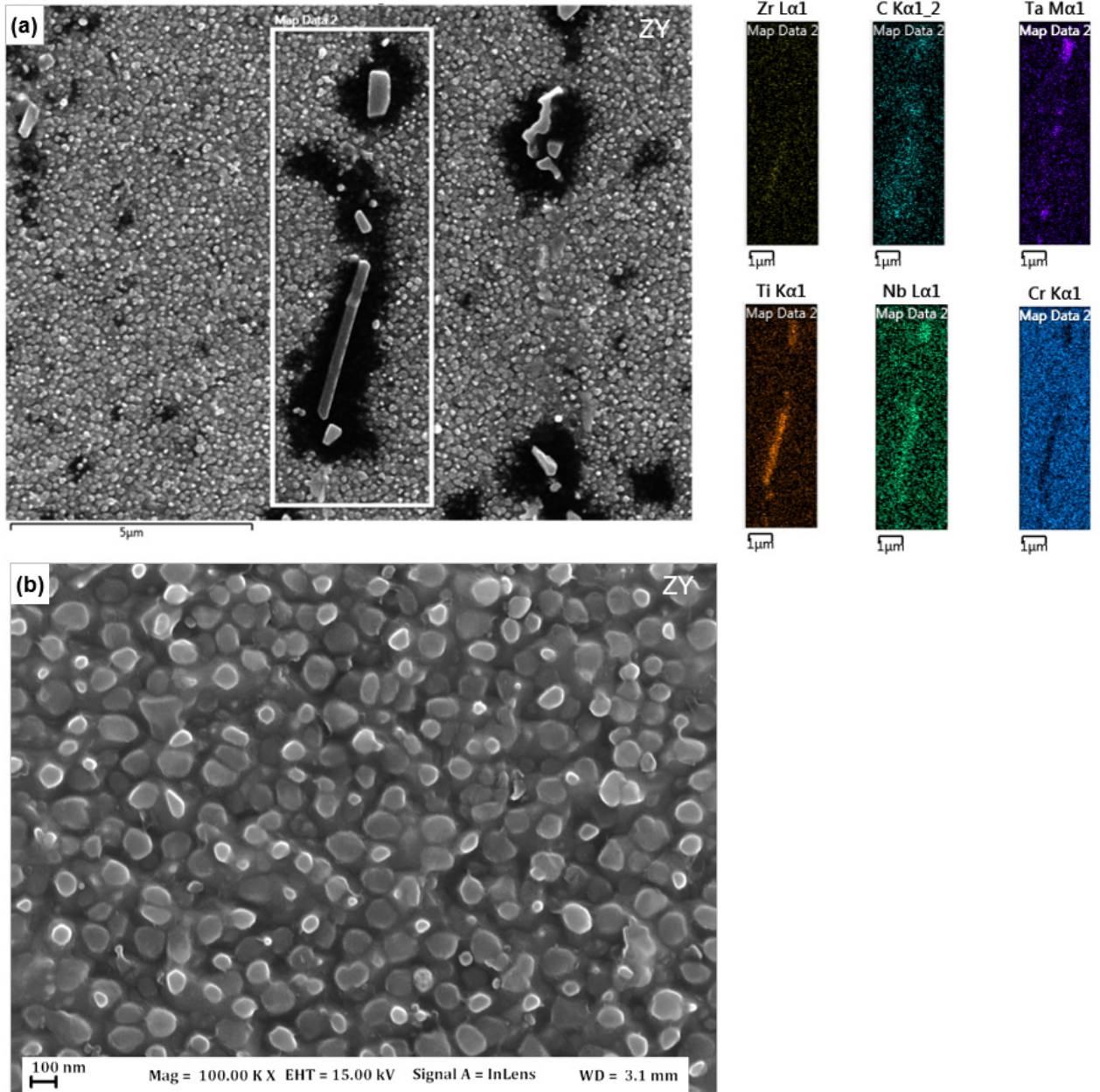


Figure 34: Microstructure of HT-F: 4/1160 + 16/845

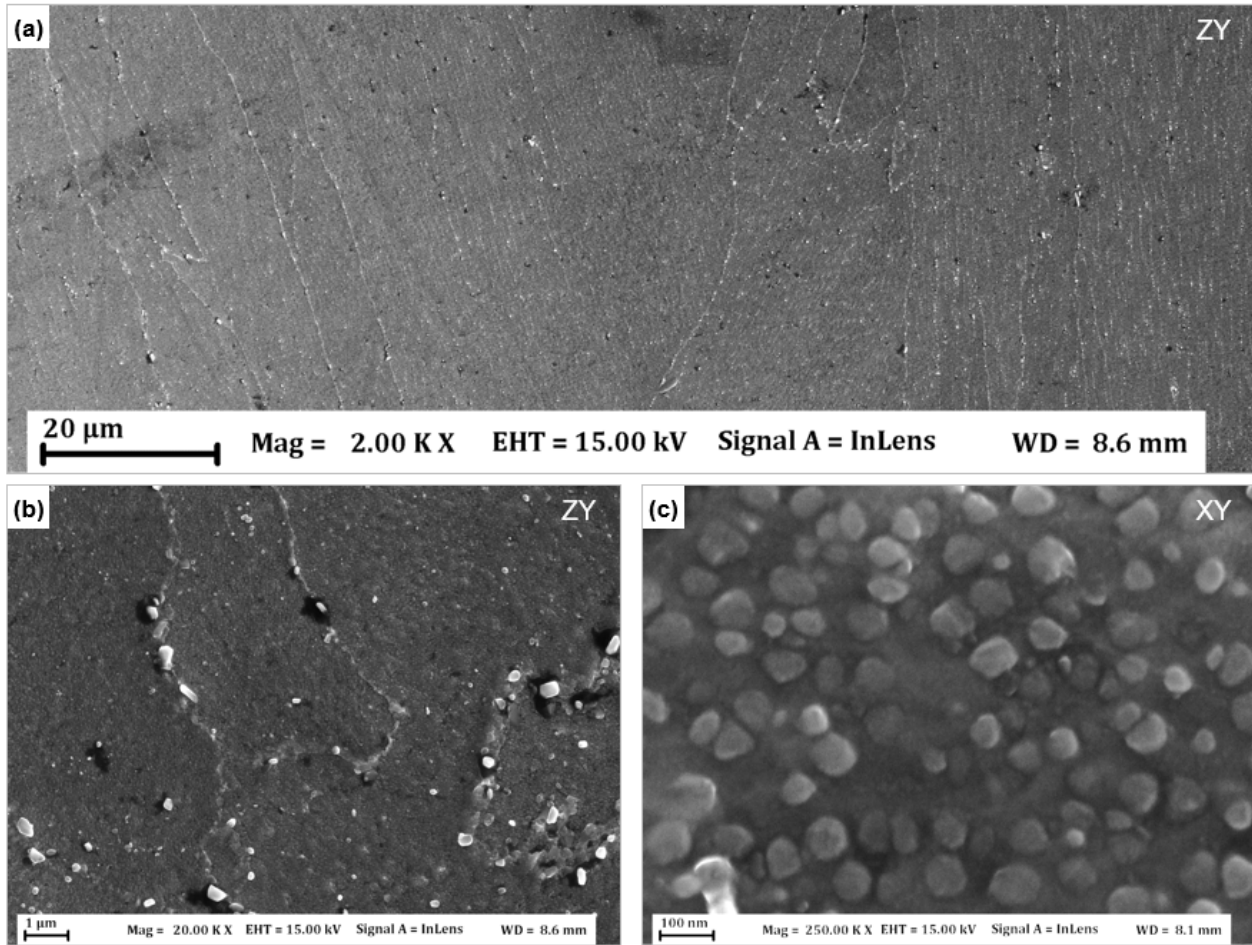


Figure 35: Microstructure after low-temperature solution treatment HT-G: 4/1100

4.5.7 HT-G: 4 hrs / 1100°C

The low-temperature solution treatment at 1100°C resulted in the microstructure shown in Figure 35. The structure appears to be less homogenized than the microstructure after standard solution treatment at 1160°C, which is described in Section 4.5.2: more evidence of the dendritic solidification structure and inter-dendritic segregation and carbide precipitation can be seen. The fine ~20 nm γ' particles seen in the standard solution treatment were not observed, and γ' size was generally limited to less than 100 nm – see Figure 35 (c).

No indications of presence of η phase were observed in the microstructure, despite the solution treatment temperature being below the η solvus temperature as found in literature and determined by DSC. If present, η would generally be observed as clusters of plate-like phase at the inter-dendritic regions. However, the presence of η cannot be ruled out. It is possible that η phase plates are at this stage simply too small to be imaged, or are not revealed (or consumed) by the Kalling's 2 etchant. Analysis at higher resolution would be required to prove that η is absent from the microstructure.

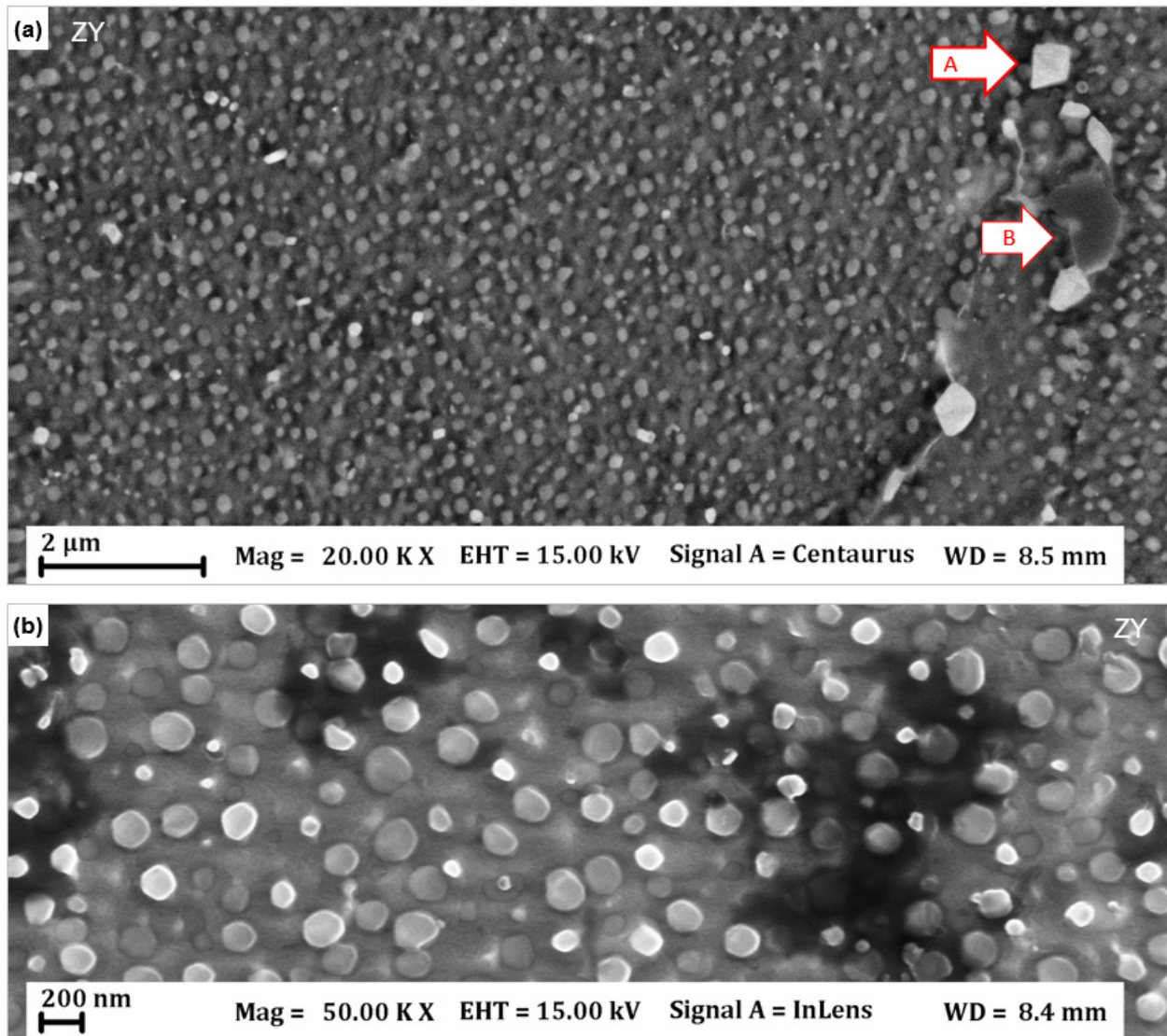


Figure 36: Microstructure of IN939 subjected to HT-J: 4/1160 + 6/1000 + 16/700

4.5.8 HT-J: 4 hrs / 1160°C + 6 hrs / 1000°C + 16 hrs / 700°C

The omission of the 24 hour ageing step from the standard 4-step heat treatment did not produce any obvious changes in the microstructure of the material. Figure 36 shows that the microstructure is well homogenized with MC type and $M_{23}C_6$ type carbides at grain boundaries. An example of an MC type carbide is shown by the arrow A in Figure 36 (a), while an $M_{23}C_6$ type carbide is shown by the arrow B. The γ' sizes and distribution as seen in BSE and SE imaging are also very similar to the observations for the standard 4- step heat treatment in Section 4.5.5.

4.5.9 HT-P: 6 hrs / 1000°C + 16 hrs / 700°C

Alloy IN738, which is a predecessor alloy to IN939, is heat treated using a sub- γ' -solvus solution treatment. A similar approach was applied with HT-P to evaluate the effect of omitting the 1160°C

solution treatment and jumping straight to the first ageing step. The resulting microstructure is exhibited in Figure 37.

Compared to the microstructures seen after 1160°C (HT-B) and 1100°C (HT-G), the microstructure after omission of solution treatment is considerably less homogenized. Grain boundaries are not as clearly defined and MC type carbides appear to be distributed randomly. The prior dendrite cores and interdendritic regions can be easily discerned because γ' particles have precipitated in straight lines along the dendrite cores. The carbides in the microstructure appear to be only MC type with sizes generally smaller than 1 μm .

A plate-like phase is easily visible in all three micrographs in Figure 37, which has not been observed in any other results so far. The phase appears to be growing only at certain crystallographic orientations. Individual plates appear to be only about 100 nm in thickness and about 2 μm in diameter. EDX analysis at one of the largest observed plates is also shown in the figure. Spectrum 12 represents an EDX point analysis at the plate-like phase, and Spectrum 13 is the corresponding analysis at the matrix.

Spectrum 13 can be compared to Spectrum 10 from Figure 29, and appears very similar since both are at the matrix. Spectrum 12 shows very strong peaks of Ni (note that the counts scale of Spectrum 12 is different from the other spectra) which are in fact stronger even than those observed for point analyses at the matrix. This suggests that the platelet phase contains high amounts of Ni, and leads to likely identification as the Ni_3Ti - η phase. According to Formenti et al, the η phase in IN939 can also contain some amount of other elements (Ti, Co, Cr, Al, and Nb in decreasing order of amounts) [25], and this may explain the identification of these elements in minor quantities in Spectrum 12.

4.5.10 HT-M: 40 hrs / 1160°C

The microstructure of DMLS-processed IN939 after an extended solution treatment of 40 hours is shown in Figure 38. The BSE image in Figure 38 (a) shows a microstructure that has undergone substantially greater recrystallization than the microstructures shown in Section 4.5.2. The size of carbides also appears larger than that observed in the 4 hour solution-treated microstructure. Moreover, no γ' precipitation was observed in the microstructure after this extended solution treatment.

4.6 Powder Microstructure

The microstructure of gas atomized IN939 powder particles is shown in Figure 39. The optical micrograph shows the spherical morphology and size of the powder. Satellites can be observed, along with minor irregularly shaped particles. The microstructure can be seen to be dendritic. Figure 39 (b) and (c) show electron micrographs of powder etched electrolytically, where the dendrite cores have been preferentially

attacked by the etchant, giving the inter-dendritic regions a raised appearance. Arrow A in Figure 39 (c) shows voids inside the powder particle, and Arrow B shows fine carbides at the inter-dendritic regions. It can be inferred that despite the high cooling rates in the atomization process, carbide precipitation still occurs.

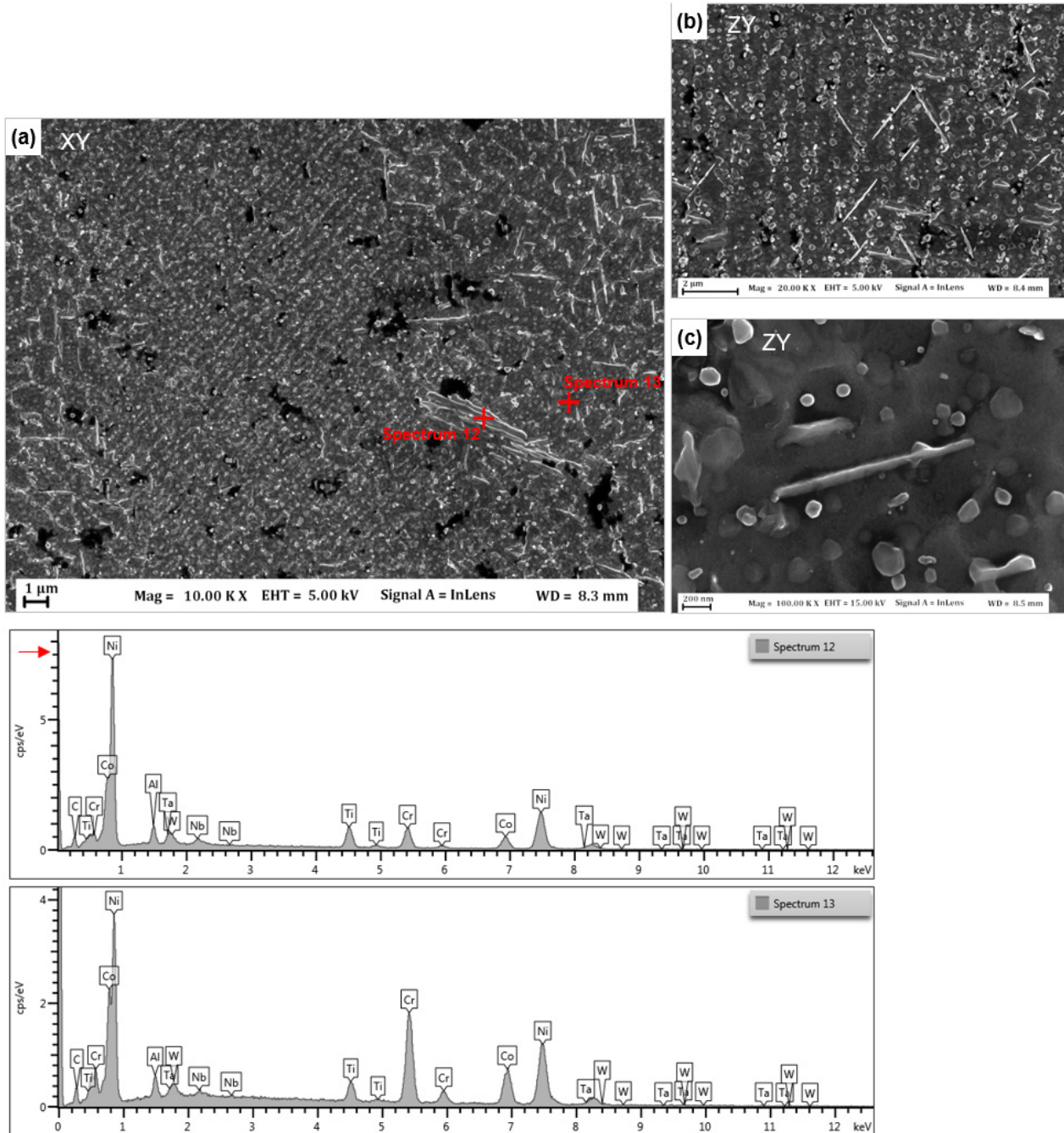


Figure 37: HT-P: Microstructure resulting from omission of solution treatment – 6/1000 + 16/700

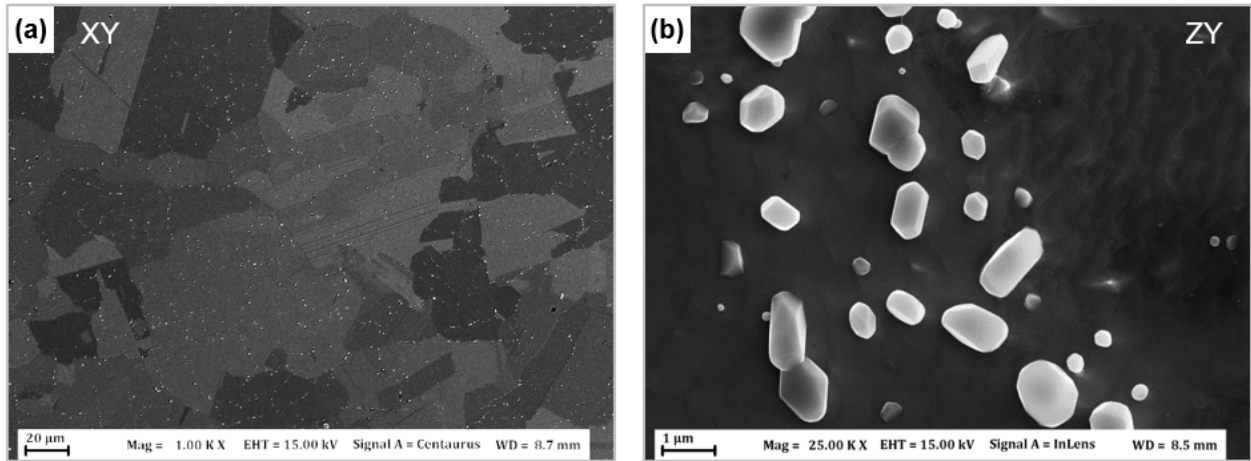


Figure 38: Microstructure of DMLS IN939 after extended Solution Treatment for 40 hours / 1160°C

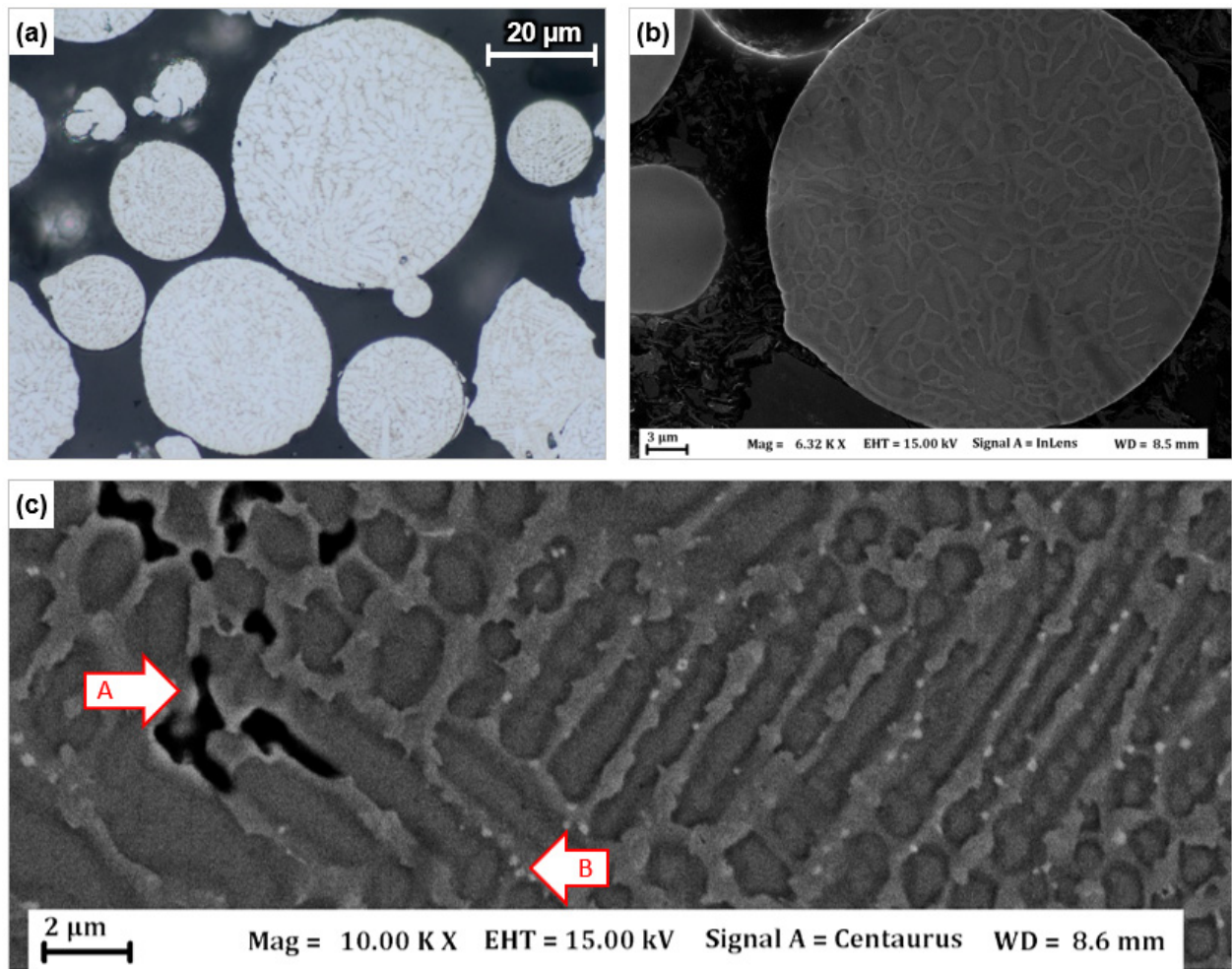


Figure 39: Microstructure of powder particles; (a) Optical Micrograph, Kallings 2 etch, (b) and (c) Scanning Electron Microscopy images, Electrolytic etch

4.7 Tensile Testing Results

A summary of the results of tensile testing is shown in Figure 40. Averages of the 0.2% offset yield strength and percentage elongation for three samples tested for each orientation for each heat treatment are shown along with their standard deviations. For the sake of meaningful interpretation of data, only values of 0.2% offset yield strength and tensile elongation are included. The complete data set of tensile testing results can be found in Appendix 2.

A clear trend across all heat treatment conditions is that vertical tensile samples show significantly higher elongation compared to horizontal tensile samples. This may be explained by the texture of the DMLS-built material, which has a higher density of grain boundaries in the horizontal direction than in the vertical direction. The same explanation can be applied to the observation that yield strength in the horizontal direction is always greater than or equal to the yield strength in the vertical direction. This is a result of the grain size hardening effect caused by higher density of grain boundaries of AM material in the “horizontal” XY plane.

The HT-A material (as-built) shows a yield strength of 802 MPa and 732 MPa in horizontal and vertical orientations respectively. This agrees very closely with the values reported by Kanagarajah et al in their paper on processing of IN939 by Selective Laser Melting [36]. However, Kanagarajah et al observed higher values of strength and elongation for samples built vertically, rather than horizontally. Elongations of 31 and 32% for horizontal and vertical as-built DMLS samples compare favourably with values of 14 and 25% reported by Kanagarajah et al for SLM samples.

Solution treating the material produces a significant increase in yield strength to the value of ~1070 MPa for both orientations. And as expected, a marked reduction in ductility. These effects are attributed to the substantial and bimodal γ' precipitation that has been observed in the microstructure [7], [8], [17]. HT-C and HT-D resulted in progressively lower strength and ductility. This is contrary to expectation, as the results quoted by Shaw [8] show an increase of yield strength with progressive ageing. The 700°C ageing performed in HT-E raises the yield strength at the expense of ductility. However, there is no notable gain over the values already observed in the solution treated HT-B condition.

HT-F produced yield stress values on average ~10% higher than the standard 4-Step HT-E, with similar or better elongation. HT-J, which skipped the 24 h / 900°C step, also showed yield stress higher than HT-E, and comparable values of elongation, which is an important result.

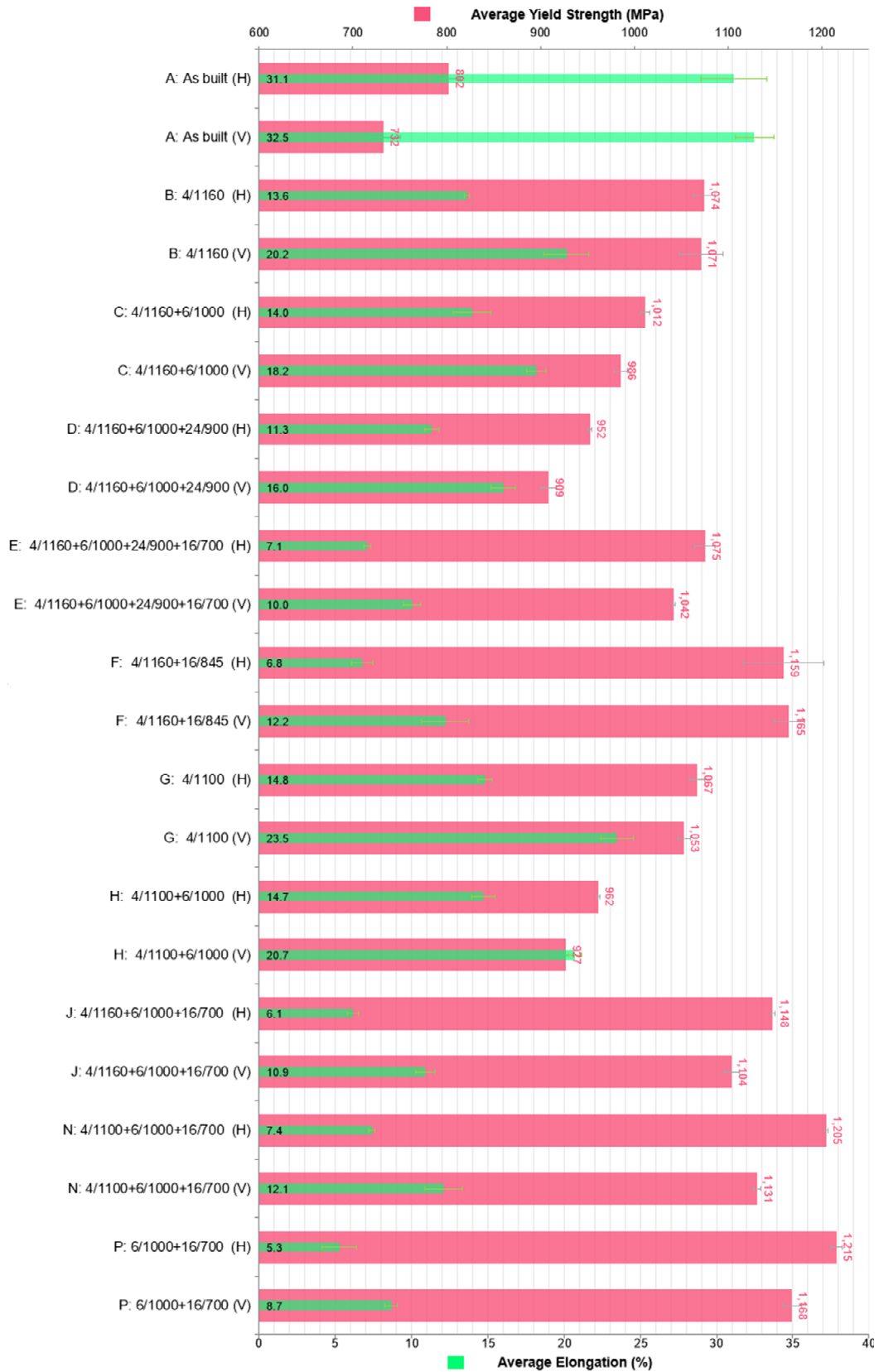


Figure 40: Comparison of yield strength and elongation from tensile testing at different heat treatment conditions

The low-temperature solution treatment also showed high values of yield strength, however these were somewhat less than the 1160°C solution treatment. Understandably the observed elongation values were very high at ~15% and ~24% for horizontal and vertical samples respectively. As with HT-B, adding an ageing step at 1000°C for 6 hours (HT-H) increased ductility and reduced yield strength. Adding a 700°C ageing step produced very high yield strengths at good ductility. When HT-N is compared to HT-J (the only difference being solution treatment at 1100°C vs 1160°C) HT-N shows higher yield strength as well as higher ductility. A significant drop in ductility is observed when the solution treatment is skipped, while the highest values of yield strength were reported for this treatment.

5. Discussion

5.1 Identification of cracking mechanism

A metallographic and fractographic examination of crack-containing and crack free IN939 specimens was presented in Section 4.1. These results show dendritic appearance at the interior of cracks seen in metallographic sections, as well as at exposed crack facets on the fracture surface. The tensile bars which were fractured and studied in fractography were built horizontally on the build platform. Due to the epitaxial growth across layers, typical of L-PBF microstructures, the resulting bar would be composed of a large number of columnar grains oriented perpendicular to the longitudinal axis of the test sample. The same would be true for cracks, which have been shown to be inter-granular. Figure 41 (a) provides a schematic representation of the orientation of cracks in the tensile bar. The appearance of the fracture surface clearly shows weak cohesion between the dendrite columns observed on the fracture surface. Absence of any dimples indicates that these facets did not bear any load during testing, and thus were already separated from their mating fracture surface at the time of application of tensile stress. The dimensions and distributions of crack faces over the fracture surface corresponds well to the metallographic observation of cracks, and along with the absence of any similar observation in crack-free material, reaffirm the understanding that these are indeed the exposed surfaces of cracks in the material.

If a crack is considered to be a planar surface, it must be recognized that cracks can have a range of orientations in 3D space while still remaining parallel to the building direction. Figure 41 (b) shows two such extremes of how cracks may be oriented. The ZX plane in the figure is the plane of the fracture surface, therefore the cracks encircled by dotted-red seen in Figure 17 (a) correspond to those which are oriented as Crack A in Figure 41 (b). When fracture occurs the mating faces of these cracks would end up on opposing fracture surfaces. This may also explain the multiple initiation points and steps observed on the fracture surface. However, any cracks oriented perpendicular to the fracture plane – see Crack B in Figure 41 (b) - would then appear as lines or slits. The arrow labelled in “A” in Figure 17 provides an example of one such crack.

The observation of dendritic morphology inside cracks is cited in welding literature as an indication of solidification cracking [31]. No other cracking mechanism is known to show dendrites at the exposed crack facets. Dendrites are linked to solidification cracking as these are a signature of the presence of a liquid film that decreases cohesion between the dendrite/cell packages and hence can result in cracking in case of presence of the stresses, as in AM or welding. The same conclusions have also been drawn by Carter et al [35] and Cloots et al [37] in studies specific to the cracking of Ni-base superalloys in L-PBF.

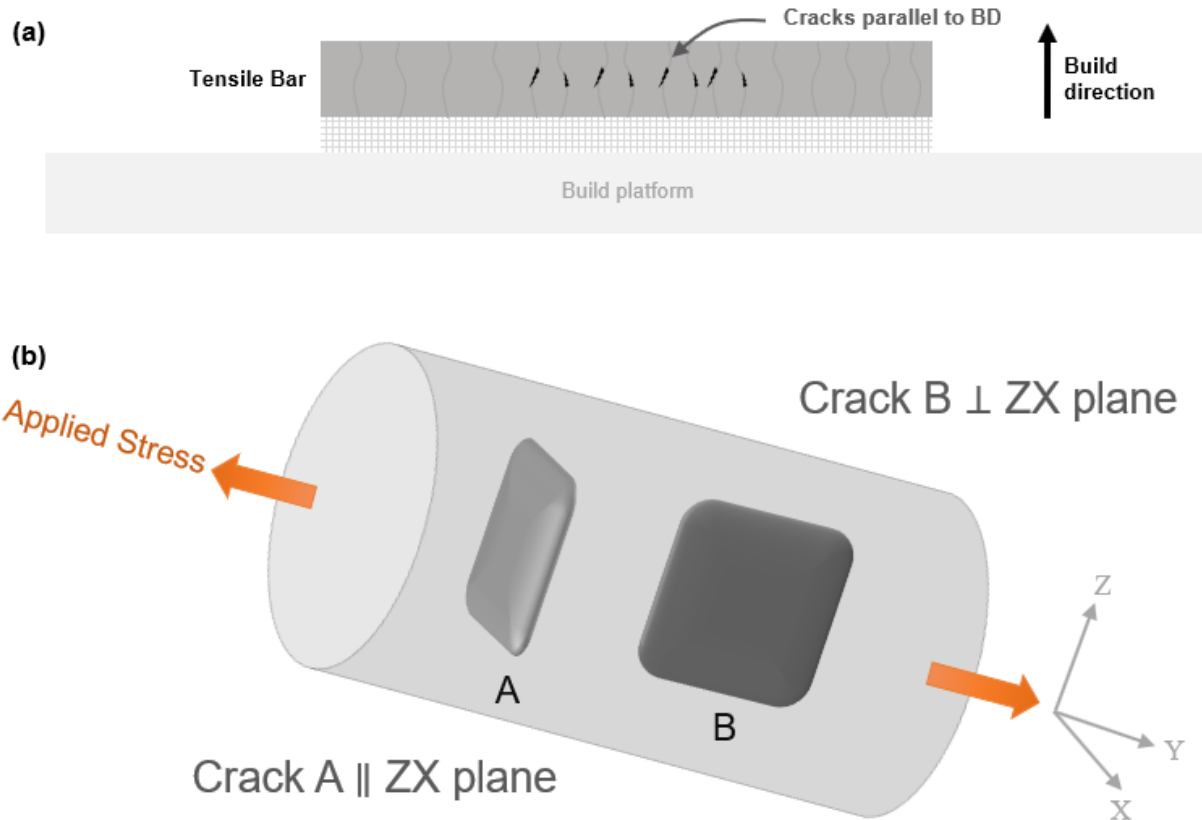


Figure 41: (a) Orientation of cracks in horizontally built tensile specimens used in fractography; (b) Range of orientations of cracks with respect to the applied stress and fracture surface.

Experimental observation of the chemical constituents of a residual liquid film could not be made, as this would require characterization methods with much higher resolution, e.g. APT, which were beyond the scope of this work. As mentioned in Section 2, several authors have used such methods to study cracking in related alloys, and their results also point towards solidification cracking as the probable mechanism [37], [38].

The hypothesis of solidification cracking as the primary cracking mechanism is well-supported by the Scheil Solidification simulation results in Figures 19 and 20, which predict the presence of liquid well below the equilibrium solidification temperature. The heavy segregation of Zr and B to the liquid at the tail end of solidification is consistent with welding literature [31] and with the results obtained by Cloots et al in their study on IN738LC [37], in which comparable Zr content is found. There is, however, cause for closer examination of the Scheil solidification simulation. The Scheil-Gulliver model is based on the assumption that there is perfect homogeneity in the liquid. Given the extremely fast cooling rates in L-PBF processes [44] this may not be the case in the IN939 DMLS melt pool, as there may be insufficient

time for diffusion of all elements in the melt. If high local concentrations of liquid stabilizing elements are produced in a melt pool - as might be the case when a grain boundary is re-melted - the solidus temperature would be lowered further than predicted by the Scheil solidification simulation. This would in turn increase the likelihood of solidification cracking. Segregation of heavily partitioning elements has also been shown to be underestimated by Thermocalc in other work [45], and Formenti et al have claimed that the Scheil model cannot accurately describe partitioning of elements in IN939 [46]. It is also worth noting that the equilibrium solidus temperature predicted by Thermocalc is far lower than that predicted by JMatPro and observed in DSC.

Results in Figure 16 show that large cracks can extend across multiple layers in the build direction. The basic theory of solidification cracking does not describe how a crack continues across several layers of material, nor why cracks are not healed by re-melting layers. This may be explained with reference to the publication of Chauvet et al on PBF of an (unspecified) Ni-base superalloy, where the authors claimed that hot cracking occurs preferentially at High Angle Grain Boundaries rather than Low Angle Grain Boundaries [38]. Once a crack has formed at such a boundary, epitaxial solidification prevents re-melted material from healing the crack by promoting dendritic growth at high misorientation angles on opposite sides of the crack. Epitaxial growth across multiple layers and melt pools can be readily observed in as-built material, and an example is presented in Figure 42. However, it is plausible that if an initiated crack is completely re-melted, the crack may not reoccur.

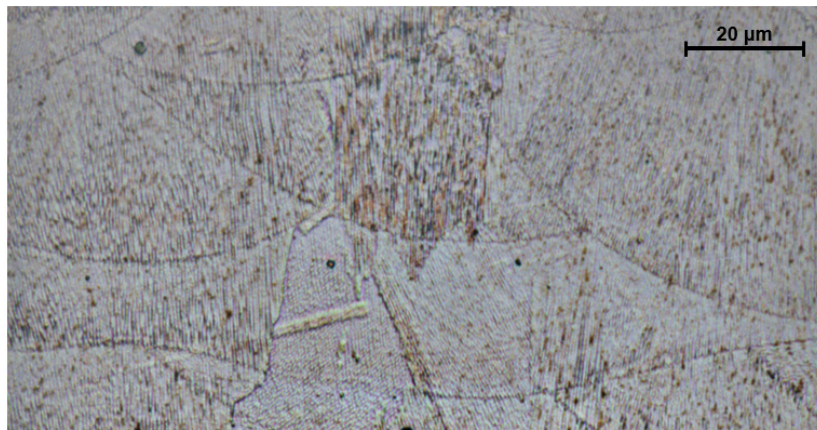


Figure 42: Epitaxial growth: dendrites continue to grow in a specific orientation across multiple melt pools.

Apart from the clear dendritic morphology and its well-known association with hot cracking, the solid-state cracking mechanisms are improbable for several reasons. No increase in frequency of cracks was seen after heat treatment, nor was any gradient in cracking observed between the top and bottom of the builds. In the case of SAC being a significant contributor to cracking, the in-situ ageing of Ni-base superalloys [44] due to thermal cycling during the building process would lead to greater cracking

frequency at the bottom of the build than at the top. Furthermore, there are currently no studies published which claim to have proven DDC or SAC as the dominant cracking mechanism in L-PBF of IN939 or similar Ni-base superalloys.

Based on the obtained results, liquation cracking does not appear to be the primary mechanism of cracking. However, the pre-requisite factors for the established mechanism of solidification cracking are also causes for HAZ liquation cracking. Since IN939 has shown to be prone to segregation of low-melting elements, and the DMLS process provides ample opportunity for re-heating and constitutional re-melting, liquation cracking cannot be eliminated as a supplementary cracking mechanism.

5.2 Rationale for selection of trial heat treatments

The standard heat treatment for IN939 requires 50 hours at temperature, in addition to heating and cooling times. The heat treatments HT-B to HT-E were performed to study the effect of each step of the standard 4-step heat treatment on the microstructure and mechanical properties. This information may be available in various literature sources, but applied to cast material. Since the starting microstructure for material built with the DMLS process is vastly different, a re-examination of these effects was considered necessary. As was noted in Section 2.5, HT-C is also considered a two-step heat treatment in itself. HT-F was a heat treatment applied during the development phase of IN939 [8] which provided extremely high tensile performance, at the cost of elongation. It was considered that better elongation may be seen due to the fine grain structure. The 1100°C solution treatment, HT-G, was tried based on the premise of an as-built structure with little segregation not requiring quite so high a solution treatment. It was considered that in case η phase was absent in the material there would be no need to solutionize above 1100°C. HT-H added a 6/1000 step, which is shown in multiple sources to be a necessity for good tensile ductility. HT-J was performed in order to evaluate the effect of skipping the 24 hour ageing step in the standard 4-step heat treatment. HT-M were intended to evaluate the effect of longer a solutionising step on microstructure and especially grain structure. HT-M was limited only to metallographic samples. HT-N was performed to understand the combined effect of a lower-temperature solution treatment and skipping of the 24 hour ageing step at 900°C. The solution treatment step was skipped altogether in HT-P to see how the material would react.

5.3 Phase Transformation Temperatures in As-Built IN939

Formulation of an efficient and effective heat treatment regime requires knowledge of the important phase transformation temperatures of the alloy. Since equilibrium phase diagrams are not available for alloys with compositions as complex as IN939, the results of simulation and thermal analysis are considered for a better understanding of reaction temperatures. In Table 11 the results from the DSC measurements on

as-built material (Section 4.3) are compared with the simulation results from JMatPro (Section 4.4) and those reported in literature.

There is generally good agreement on the liquidus temperature across results from DSC, simulation, and literature. An accurate measurement of the MC carbide solvus temperature could not be obtained because of the wide melting range of the alloy and the proximity of the MC carbide solvus temperature to the liquidus. However, it appears that MC carbides start to form at $\sim 1300^{\circ}\text{C}$ while the alloy is still partly molten. The performed DSC was not sensitive enough to determine the solidus temperature accurately, but based on the DSC graph for the heat-treated material, solidification appears to be completed at 1240°C , which agrees well with literature. The γ' solvus temperature range is also accurately measured by thermal analysis and agrees with the JMatPro simulation as well as literature.

The solvus temperature for the η -phase is of importance since the primary objective of solution treatment is to dissolve η so as to safeguard against its embrittling effects. No clear η -phase dissolution could be detected in DSC of the as-built material during the heating phase. The formation of η was noticeable on the DSC graph in cooling, which at least proves that the composition is susceptible to η formation. This peak was observed around $\sim 1160^{\circ}\text{C}$. The η -phase solvus temperature is quoted in literature [7] and predicted by JMatPro to be between 1134°C and 1145°C . It appears that both the current DSC work and even the Differential Thermal Analysis performed by Formenti et al [25] have overestimated the η solvus. Comparison to the heating DSC curve for heat-treated material showed no peaks at all between 1100°C and 1200°C . This provides further proof that no η -phase exists in the 4-step heat treated microstructure. Formation of η in as built microstructure remains inconclusive.

Phase reaction	Temperature ($^{\circ}\text{C}$)		Temperature ($^{\circ}\text{C}$)	Temperature ($^{\circ}\text{C}$)	Temperature ($^{\circ}\text{C}$)	
	<i>Current Work, DSC As Built</i>		<i>Current Work</i>	<i>Gibbons et al</i>	<i>Formenti et al – from DTA</i>	
	Heating	Cooling	<i>JMatPro</i>		Heating	Cooling
Liquidus temperature	1339	-	1337	1340	1339	1325
Formation of primary MC	~ 1310		1320	1320	1276-1313	1250-1290
Solidus temperature	1250 ± 30	-	1207	1235	1235	-
η solvus temperature	-	~ 1160	1134	1145	-	~ 1209
γ' solvus temperature	1085 - 1105		1104	1080-1100	-	-
M_{23}C_6 solvus temperature	-	-	-	~ 1000	-	-
σ solvus temperature	-	-	-	~ 950	-	-
Max rate of σ formation	-	-	-	~ 850	-	-

Table 11: Comparison of phase transformation and reaction temperatures between measurements from thermal analysis, predictions from simulation, and literature. Sources: [7], [25], [46]

5.4 Optimization of Solution Treatment Temperature

5.4.1 Precipitation of γ' after solution treatment

Two different solution treatment temperatures were studied, and an additional extra-long 40 hour solution treatment was also investigated. Different γ' precipitation was observed for each of these heat treatments. As shown in Section 4.5, the standard 4 hr / 1160°C solution treatment showed a bi-modal distribution of γ' precipitates, the 4 hr / 1100°C solution treatment showed γ' precipitates of about 50-100 nm size, and 40 hr / 1160°C extended solution treatment showed no γ' precipitation at all. Figure 43 shows a schematic diagram of the thermal cycling experienced by the alloy before and during the solution treatment. This consists of a number of very fast heating and cooling cycles during the DMLS processing. The exact temperatures, heating and cooling rates, and number of cycles is not known, however the cycling has been shown to affect the microstructure [44] and it is conceivable that the material spends some amount of time within the γ' precipitation range. The rest of the thermal history consists of the heat-up step (where the material spends many tens of minutes in the γ' growth temperature range), the holding step, and the cooling step. Figure 43 (b) shows a recorded temperature gradient of the forced air cooling step, and here also the material spends 2 to 3 minutes in the γ' growth temperature range. Precipitation during the quenching step has also been recorded in literature [7].

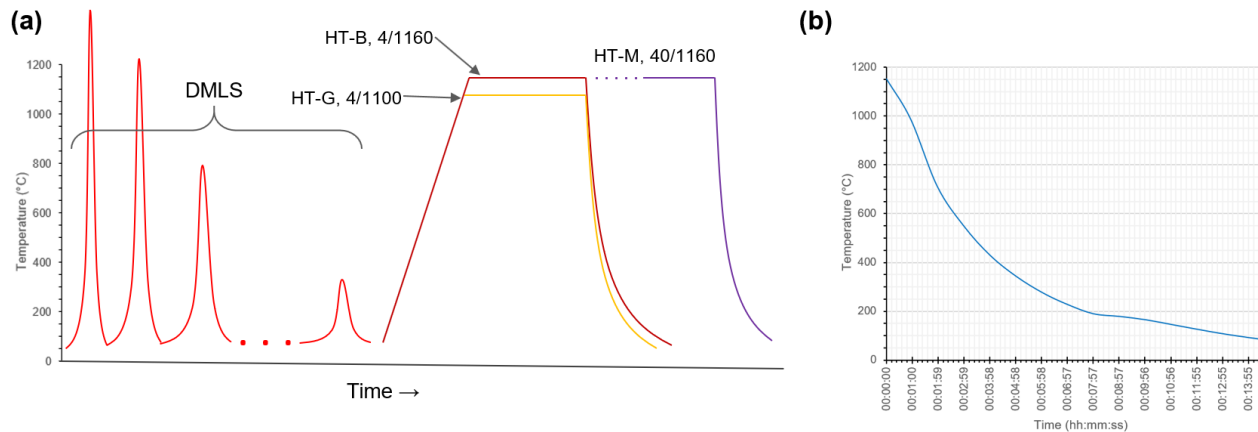


Figure 43: (a) Schematic illustration of the thermal cycling in DMLS processed IN939 during the DMLS build and during the various solution treatments; (b) measured temperature profile during Forced Air Cooling from 1160°C

A hypothesis has been formulated to explain the different γ' precipitation observed. It is proposed that the “primary” γ' is precipitated during the DMLS thermal cycling, however it is some tens of angstroms in diameter and too small to be seen in SEM. Consider that for the 4 hr / 1100°C HT-G, the primary precipitates would then grow during the heat-up step, while a secondary population would be precipitated. Since the secondary γ' would be much smaller in size, these would be dissolved during the 1100°C hold, while the primary would either be partially dissolved or unaffected. When the material is cooled, the

primary precipitates are grown and appear as the 50-100 nm population observed in Section 4.5.7. A secondary population may either not be precipitated at all due to lack of solute, or may be too fine to be observed in the SEM.

A similar evolution of γ' precipitation can be envisaged for the standard solution treatment at 1160°C i.e. HT-B. Again the primary precipitation happens during DMLS, and these precipitates grow during the heat-up for solution treatment. The secondary γ' is precipitated during the heat-up phase but completely re-dissolved during the hold, while the primary is only partially dissolved due to the high-volume fraction and insufficient time at temperature. Cooling for this heat treatment starts at 1160°C, so more time is spent in the γ' precipitation temperature range compared to HT-G. Thus during quench cooling the primary γ' is grown, and the secondary population is precipitated and has time to grow to the ~20 nm size observed in Figure 28. This also explains the larger size of γ' after HT-B compared to HT-G.

The reason for apparent absence of γ' in the 40 hr / 1160°C solution treatment HT-M could be that the precipitates are completely dissolved due to the extended time above solvus temperature. Alternatively, fine γ' may have precipitated during cooling but may simply be too small to observe. Microscopy at higher resolutions in all the relevant stages of heat treatment would be needed to show evidence of the proposed precipitation sequence.

It is also worth noting that Delargy et al have recommended a difference of 180K between successive heat treatment steps for precipitation of a bimodal γ' distribution, based on which 1160°C is a more rational temperature for solution treatment.

5.4.2 Effect of Solution Treatment on η -phase

The discussion on thermal analysis showed that samples solution treated at 1160°C do not contain η -phase, while presence of η was inconclusive in the as-built specimens. Microstructural analysis showed no η in any of the solution treated or fully aged samples. Conversely, omitting the solution treatment step resulted in widespread plates of η -phase in the microstructure, which lead to the highest observed yield strength and lowest observed ductility. The η -phase appears to have grown through the 1000°C and 700°C ageing steps when solution treatment was skipped. Based on these results it is inferred that η -phase does exist in the as-built microstructure, albeit too small to observe. This necessitates a super- η -solvus solution treatment above ~1145°C.

The microstructure and tensile test results of HT-G i.e. 4 hr / 1100°C do not show any signs of plate-like phases or embrittlement, however η would be very small in size at this stage of heat treatment, and may even have a positive effect on the mechanical properties through precipitation strengthening. In fact, Lund

and Wagner have claimed that η phase is coherent with the matrix when it is first formed [41]. The samples that were further aged after 1100°C solution treatment could not be studied in SEM, and this would need to be done to establish whether η is present or not. Higher resolution microscopy or atom probe analysis is also recommended to look for η in the as-built and sub- η -solvus solution treated samples.

The long term effects of η -phase on high temperature endurance are reported as overwhelmingly negative [7], [17]. Despite the exceptional mechanical properties exhibited by the samples heat treated with 1100°C sub- η -solvus solution treatment, the conventional 1160°C solution treatment must be preferred.

5.5 Development of Microstructure and Mechanical Properties through HT Steps

The evolution of microstructure from fine dendritic as-built through the various stages of heat treatment was presented in Section 4.5. A description of the cast microstructure as it should appear after the standard 4-step heat treatment was provided in Section 2.3. Apart from the grain size and texture which are typical of PBF processes, several other differences between the DMLS processed and the cast microstructures are also notable.

The difference in γ' precipitation was discussed in depth in Section 5.4. It is worth reiterating that a bimodal γ' distribution was observed even after just the solution treatment, which for cast material is described only after the final step of the 4-step heat treatment. Interestingly this was not seen after HT-E, but the excellent mechanical properties observed after HT-B correlate well with the γ' distribution.

An argument for lowering of the solution treatment temperature was made by Jahangiri et al [40] based on incipient melting observed at inter-dendritic regions. No evidence of incipient melting was found in the microstructure after solution treatment, which can be attributed to the high cooling rates in DMLS producing a microstructure with less segregation compared to cast.

The effect of the 1000°C ageing step on microstructure is not described fully in literature. Shaw submits that during development of heat treatment for IN939 the reduction of ageing temperature from 1080°C to 1000°C prevented the formation of η phase [8], however there is no evidence of this effect. Since mechanical properties of DMLS-processed material deteriorate upon this step, and ductility seems not be a concern due to the fine-grained structure, it is recommended to re-examine the necessity of this step in future work. The high elongation exhibited by HT-F, which includes no 1000°C age, also suggests that this step is unnecessary.

The evolution of carbide morphology was another point of difference between what is reported for cast and what has been observed for DMLS-processed IN939. Cast alloy is supposed to contain strings of fine $M_{23}C_6$ carbides, which were not present, or otherwise not observed. Larger $M_{23}C_6$ carbide particles, as

shown in Figures 31 and 32, were found at grain boundary triple points. The effect of such carbides on creep strength is not certain, and must be tested. The absence of any film-like grain boundary carbides is, however, a positive observation.

The 900°C ageing step has been cited as having the effect of precipitating $M_{23}C_6$ carbides. This was indeed observed as shown in Section 4.5.4. Omitting this step and jumping straight to ageing at 700°C did not prevent formation of $M_{23}C_6$ carbides. On the whole it appears that of all steps in the 4-step heat treatment, the 900°C ageing step has the least influence on the final microstructure.

The high strength and dense γ' precipitation observed in HT-F show that even a single ageing at the 845°C temperature is sufficient to produce good room temperature tensile properties. Shaw has shown that the highest yield strengths are achieved in cast IN939 with final ageing done at ~820°C [8], which suggests that additional experimental heat treatments with such an ageing step should be considered. The ageing time has also been optimized by Delargy et al [17], and this may also be an area where further improvement is possible.

5.6 Mechanical Performance and Creep Considerations

For applications such as turbine blades and guide vanes, components are likely to be built in the vertical orientation in DMLS machines to optimize productivity through nesting. Based on this consideration, more emphasis is placed on tensile properties in the vertical orientation. For the most demanding application, i.e. turbine blades, the conditions experienced by the material at the blade tip and blade root are significantly different. At the blade tip the highest temperatures and loads are applied, and these may be similar to the temperatures in the final ageing steps. The alloy is then aged while it is in service, and tests [17] show that stress rupture properties are largely independent of the low-temperature ageing steps. At the blade root temperatures are much lower, and the mechanical performance is closer to the room temperature properties.

Based on the discussion in Section 5.4.2, the only complete heat treatments that can be considered are HT-C, HT-E, HT-F, and HT-J. Table 12 presents a comparison between the tensile properties of vertical heat-treated samples and mechanical properties presented in literature for cast and additively manufactured IN939. For all four heat treatments, the obtained yield strengths and elongation values were higher than those observed in cast IN939. However, the trend among the heat treatments is the same as for cast. HT-C produces the highest strength, followed by HT-E and HT-J, which are roughly similar, and HT-F produced the highest yield strength. However, for DMLS processed material HT-F also produced the highest elongation, which is 6 times that of cast material. The higher strength and elongation values can be explained by the smaller grain size and finer precipitates in the microstructure. The strain rates during

testing can also greatly affect the values of elongation and yield strength; decreasing strain rate results in higher elongations, at the expense of yield strength. Note that testing strain rate for the cast material were not given, and this must be considered when comparing values.

Heat Treatment	Current Work, DMLS		Delargy et al, cast		Kangarajah et al, SLM	
	0.2% YS (MPa)	Elongation (%)	0.2% YS (MPa)	Elongation (%)	0.2% YS (MPa)	Elongation (%)
HT-C 4h / 1160°C + 6h / 1000°C	986	18.2	651	9.2	-	-
HT-E 4h / 1160°C + 6h / 1000°C + 24h / 900°C + 16h / 700°C	1041	10.0	786	3.4	-	-
HT-F 4h / 1160°C + 16h / 845°C	1164	12.2	823	2.0	~1170	~1.5%
HT-J 4h / 1160°C + 6h / 1000°C + 16h / 700°C	1103	10.9	785	3.6	-	-

Table 12: Comparison of measured average room temperature tensile properties in vertically orientated DMLS samples with those reported in literature for cast [17] and IN939 produced by Selective Laser Melting [36].

The only published mechanical testing results for additively manufactured IN939 are from the 2013 paper by Kanagarajah et al, who have used HT-F and obtained very similar values of yield strength. However the elongation values published are far inferior to the results obtained in this study. Again, the strain rates used for testing are not known.

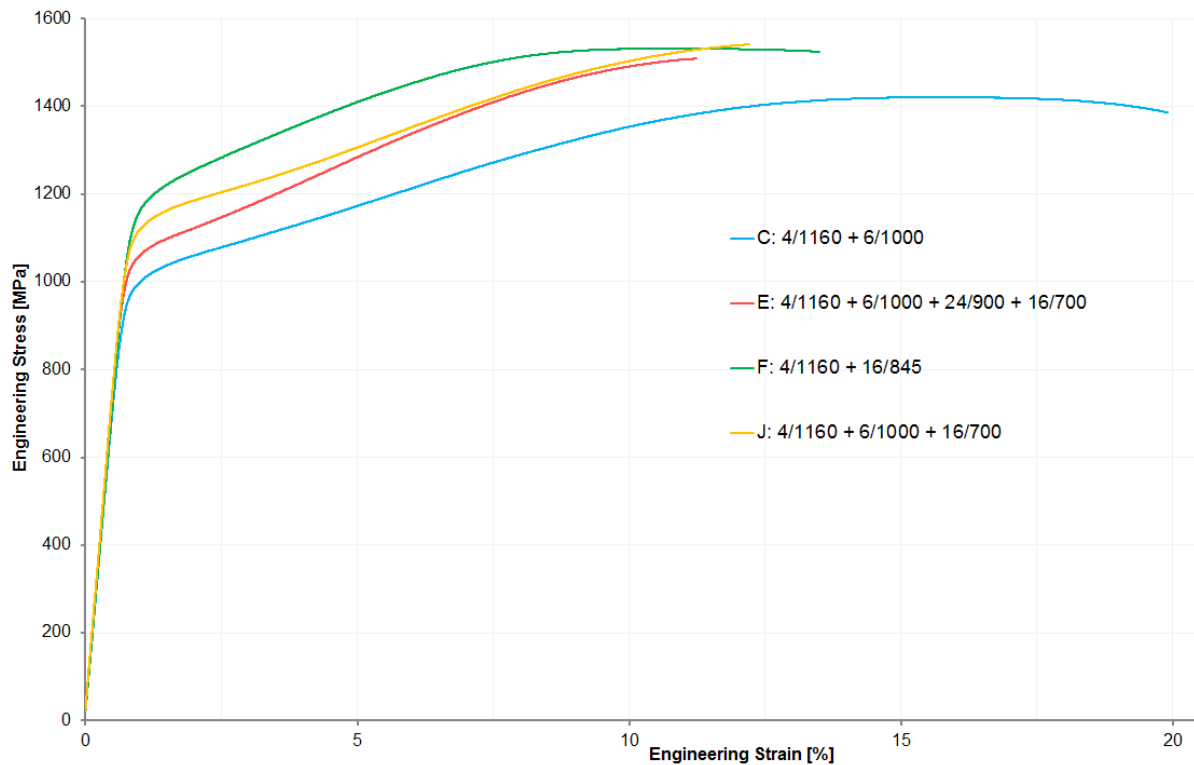


Figure 44: Tensile curves for representative vertical samples of the four best complete heat treatments

The tensile curves for representative (closest to average) vertical specimens of the four selected heat-treatments are shown in Figure 44. The best combination of yield strength and ductility was shown by HT-F. However, HT-F involves only a single ageing step, and the microstructure is considerably less homogenized than HT-E. Moreover, precipitation of the $M_{23}C_6$ type carbides was not seen in the microstructure of HT-F, and therefore its performance in creep may be inferior to HT-E or HT-J.

HT-J shows better yield strength and similar ductility to HT-E but has the significant advantage of being 24-hours shorter. No major differences in microstructure were observed. HT-J appears to be a promising candidate for evaluation of mechanical performance at high temperatures and in creep. However, the last ageing step is 700°C in HT-J which is lower than the maximum service temperature. A further iteration of HT-J with final ageing close to 820°C should be performed and evaluated.

HT-C shows the highest ductility, and may be of use as a treatment for parts that are not subject to high loads, or components that are required to be underaged for further processing.

5.7 Future Work

The drive to utilize sub- η -solvus heat treatments HT-G, HT-H, and HT-N and their evidently improved mechanical properties is considerable. It is suggested to investigate η -phase presence in the microstructures resulting from these heat treatments using high resolution microscopy, and more sensitive thermal analysis. Confirmation of the observed phases is also recommended by X-ray or electron diffraction techniques. High resolution analysis to investigate the presence of fine γ' precipitation in as-built and solution treated samples would also be instructive.

Experimental heat treatments which omit the 1000°C ageing step are also recommended in order to investigate the effects of this ageing step.

Stress rupture testing at a range of temperatures is bound to be the final step in ultimately selecting a heat treatment and proving the viability of DMLS-processed IN939.

6. Conclusions

The microstructures and mechanical properties evaluated in this thesis show that IN939 manufactured by the Direct Metal Laser Sintering process can be produced free from defects, and forms a microstructure significantly different from conventionally cast material. The mechanism causing cracking was identified and the underlying compositional segregation has been hypothesised based on literature and simulation results. The as-built microstructure was characterised in detail, and its evolution through several heat treatment stages was studied. Experimental heat treatments showed properties and mechanical performance similar to or better than conventional heat treatments, and room for further improvement has been identified. The research questions identified at the initiation of the thesis work are answered below:

- 1. Solidification cracking is suspected to be the primary cracking mechanism. Reducing concentrations of liquid-stabilizing elements such as Zr and B should effectively mitigate cracking.**
- 2. The standard 4-step heat treatment produces excellent room temperature tensile properties in additively manufactured IN939. However, the γ' and carbide sizes and morphologies are significantly different from cast material and high temperature tensile and creep performance must be evaluated.**
- 3. The 50 hour heat treatment can be reduced to 26 hours without any deterioration in room temperature mechanical properties, and ageing times and temperatures may still be further optimized. Solution treatment has proven to be the most important step in the heat treatment process and must be performed at 1160°C.**

7. References

- [1] M. Yuri, K. Tsukagoshi, S. Hada, J. Masada, and E. Ito, “Development of 1600 °C-Class High-efficiency Gas Turbine for Power Generation Applying J-Type Technology,” *Mitsubishi Heavy Ind. Tech. Rev.*, vol. 50, no. 3, pp. 1–10, 2013.
- [2] Rolls-Royce plc, *The Jet Engine*, 5th ed. Derby, England: The Technical Publications Department, Rolls-Royce plc, 1996.
- [3] N. Glover, “Materials Developments For Energy Generating Gas Turbines,” 2008, no. October.
- [4] C. Soares, *Gas Turbines: A Handbook of Air, Land and Sea Applications.*, 2nd ed. Elsevier Inc., 2015.
- [5] M. Durand-Charre, *The Microstructure of Superalloys*. Amsterdam: Gordon and Breach Science Publishers, 1998.
- [6] “CES Edupack.” Granta Design, Cambridge, 2017.
- [7] T. B. Gibbons and R. Stickler, “IN939: Metallurgy, Properties, and Performance,” in *High Temperature Alloys for Gas Turbines*, 1982.
- [8] S. W. K. Shaw, “Response of IN-939 to process variations,” *TMS Superalloys*, pp. 275–284, 1980.
- [9] J. B. Wahl and K. Harris, “Advanced Ni-base superalloys for small gas turbines,” *Can. J. Metall. Mater. Sci.*, vol. 50, no. 3, pp. 207–214, 2011.
- [10] G. Sjöberg *et al.*, “Evaluation of the IN 939 Alloy for Large Aircraft Engine Structures,” *Technology*, pp. 441–450, 2004.
- [11] C. T. Sims, N. S. Stoloff, and W. C. Hagel, *Superalloys II*. New York, NY: Wiley-Interscience, 1987.
- [12] M. J. Donachie Jr, “Understanding Superalloy Metallurgy,” *Superalloys A Tech. Guid.*, pp. 25–39, 2002.
- [13] J. K. Tien and R. N. Jarett, “Effects of Cobalt in Nickel-Base Superalloy - NASA Contractor Report,” New York, NY, 1983.
- [14] B. Wang *et al.*, “Effect of Co on microstructural stability of the third generation Ni-based single crystal superalloys,” *J. Mater. Res.*, vol. 31, no. 09, pp. 1328–1337, 2016.
- [15] P. Kontis *et al.*, “On the effect of boron on grain boundary character in a new polycrystalline

- superalloy,” *Acta Mater.*, vol. 103, pp. 688–699, 2016.
- [16] M. R. Jahangiri, H. Arabi, and S. M. A. Boutorabi, “Comparison of microstructural stability of IN939 superalloy with two different manufacturing routes during long-time aging,” *Trans. Nonferrous Met. Soc. China (English Ed.)*, vol. 24, no. 6, pp. 1717–1729, 2014.
- [17] K. M. Delargy, S. W. K. Shaw, and G. D. W. Smith, “Effect of Heat Treatment on Mechanical Properties of IN939,” *Mater. Sci. Technol.*, vol. Vol 2, pp. 1031–1037, 1986.
- [18] K. Kupi, “Material and Process Characterization of Non- Weldable Nickel Superalloys in Additive Manufacturing,” 2016.
- [19] I. Gibson, D. Rosen, and B. Stucker, *Additive Manufacturing Technologies*, 2nd ed. New York, NY: Springer-Verlag, 2015.
- [20] W. Philpott, M. A. E. Jepson, and R. C. Thomson, “Comparison of the effects of a conventional heat treatment between cast and selective laser melted IN939 alloy,” in *Advances in Materials Technology for Fossil Power Plants - Proceedings from the 8th International Conference*, 2016.
- [21] J. Li and H. M. Wang, “Microstructure and mechanical properties of rapid directionally solidified Ni-base superalloy Rene’41 by laser melting deposition manufacturing,” *Mater. Sci. Eng. A*, vol. 527, no. 18–19, pp. 4823–4829, 2010.
- [22] J. Li, H. M. Wang, and H. B. Tang, “Effect of heat treatment on microstructure and mechanical properties of laser melting deposited Ni-base superalloy Rene’41,” *Mater. Sci. Eng. A*, vol. 550, pp. 97–102, 2012.
- [23] V. A. Popovich, E. V. Borisov, A. A. Popovich, V. S. Sufiiarov, D. V. Masaylo, and L. Alzina, “Impact of heat treatment on mechanical behaviour of Inconel 718 processed with tailored microstructure by selective laser melting,” *Mater. Des.*, vol. 131, no. January, pp. 12–22, 2017.
- [24] R. Muñoz-Moreno *et al.*, “Effect of heat treatment on the microstructure, texture and elastic anisotropy of the nickel-based superalloy CM247LC processed by selective laser melting,” *Mater. Sci. Eng. A*, vol. 674, pp. 529–539, 2016.
- [25] A. Formenti, A. Eliasson, A. Mitchell, and H. Fredriksson, “Solidification Sequence and Carbide Precipitation in Ni-Base Superalloys IN718 , IN625 AND IN939,” *High Temp. Mater. Process.*, vol. 24, no. 4, pp. 239–258, 2005.
- [26] EOS GmbH, “Additive Manufacturing, Laser-Sintering and industrial 3D printing - Benefits and

- Functional Principle.” [Online]. Available: https://www.eos.info/additive_manufacturing/for_technology_interested. [Accessed: 11-Dec-2017].
- [27] EOS GmbH, “EOS M100 Datasheet Status 09/2017.” 2017.
- [28] EOS GmbH, “EOS M290 Datasheet Status 09/2017.” 2017.
- [29] EOS GmbH, “EOS M400 Datasheet Status 10/2015.” 2015.
- [30] M. B. Henderson, D. Arrell, M. Heobel, R. Larsson, and G. Marchant, “Nickel-Based Superalloy Welding Practices for Industrial Gas Turbine Applications,” *Sci. Technol. Weld. Join.*, vol. 9, pp. 1–14, 2004.
- [31] J. N. DuPont, J. C. Lippold, and S. D. Kiser, *Welding Metallurgy and Weldability of Nickel-Base Alloys*. Hoboken, New Jersey: John Wiley & Sons, 2009.
- [32] K. E. Easterling, *Introduction to the Physical Metallurgy of Welding*, 2nd ed. Oxford, UK: Butterworths & Co Ltd., 1983.
- [33] J. C. Lippold, *Welding Metallurgy and Weldability*. New Jersey: John Wiley and Sons, 2014.
- [34] M. M. Attallah, R. Jennings, X. Wang, and L. N. Carter, “Additive manufacturing of Ni-based superalloys: The outstanding issues,” *MRS Bull.*, vol. 41, no. 10, pp. 758–764, 2016.
- [35] L. N. Carter, M. M. Attallah, and R. C. Reed, “Laser Powder Bed Fabrication of Nickel-Base Superalloys: Influence of Parameters; Characterisation, Quantification and Mitigation of Cracking,” *Superalloys 2012*, pp. 577–586, 2012.
- [36] P. Kanagarajah, F. Brenne, T. Niendorf, and H. J. Maier, “Inconel 939 processed by selective laser melting: Effect of microstructure and temperature on the mechanical properties under static and cyclic loading,” *Mater. Sci. Eng. A*, vol. 588, pp. 188–195, 2013.
- [37] M. Cloots, P. J. Uggowitzer, and K. Wegener, “Investigations on the microstructure and crack formation of IN738LC samples processed by selective laser melting using Gaussian and doughnut profiles,” *Mater. Des.*, vol. 89, pp. 770–784, 2016.
- [38] E. Chauvet *et al.*, “Hot cracking mechanism affecting a non-weldable Ni-based superalloy produced by Selective Electron Beam Melting,” *Acta Mater.*, vol. 142, no. 17, pp. 82–94, 2017.
- [39] S. A. Sajjadi and S. M. Zebarjad, “Study of fracture mechanisms of a Ni-Base superalloy at different temperatures,” *J. Achiev. Mater. Manuf. Eng.*, vol. 18, no. 1, pp. 227–230, 2006.

- [40] M. R. Jahangiri, S. M. A. Boutorabi, and H. Arabi, "Study on incipient melting in cast Ni base IN939 superalloy during solution annealing and its effect on hot workability," *Mater. Sci. Technol.*, vol. 28, no. 12, pp. 1402–1413, 2012.
- [41] C. H. Lund and H. J. Wagner, "Identification of microconstituents in superalloys," Columbus, Ohio, 1962.
- [42] M. T. Jovanović, Z. Mišković, and B. Lukić, "Microstructure and Stress-Rupture Life of Polycrystal, Directionally Solidified, and Single Crystal Castings of Nickel-Based IN 939 Superalloy," *Mater. Charact.*, vol. 40, no. 4–5, pp. 261–268, 1998.
- [43] K. M. Delargy and G. D. W. Smith, "Phase Composition and Phase Stability of a High-Chromium Nickel-Based Superalloy, IN939," *Metall. Trans. A*, vol. 14A, no. September, pp. 1771–1783, 1983.
- [44] E. A. Jäggle *et al.*, "Precipitation Reactions in Age-Hardenable Alloys During Laser Additive Manufacturing," *Jom*, vol. 68, no. 3, pp. 943–949, 2016.
- [45] T. Keller *et al.*, "Application of finite element, phase-field, and CALPHAD-based methods to additive manufacturing of Ni-based superalloys," *Acta Mater.*, vol. 139, pp. 244–253, 2017.
- [46] A. Formenti, A. Eliasson, and H. Fredriksson, "On the Dendritic Growth and Microsegregation in Ni-Base Superalloys In718, IN625, and IN939," *Cast. Met.*, vol. 24, no. 4, p. 221 to 238, 2005.

8. Appendix 1 – Thermal Analysis Results

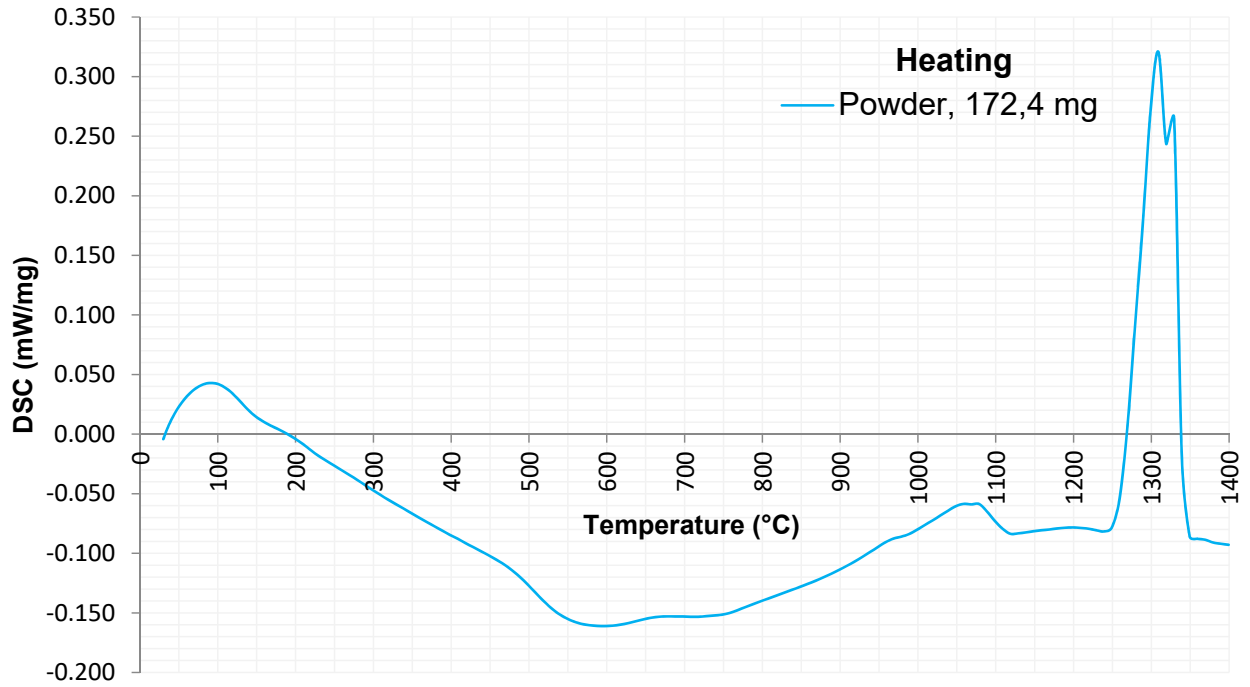


Figure A 1: DSC heating graph of IN939 powder

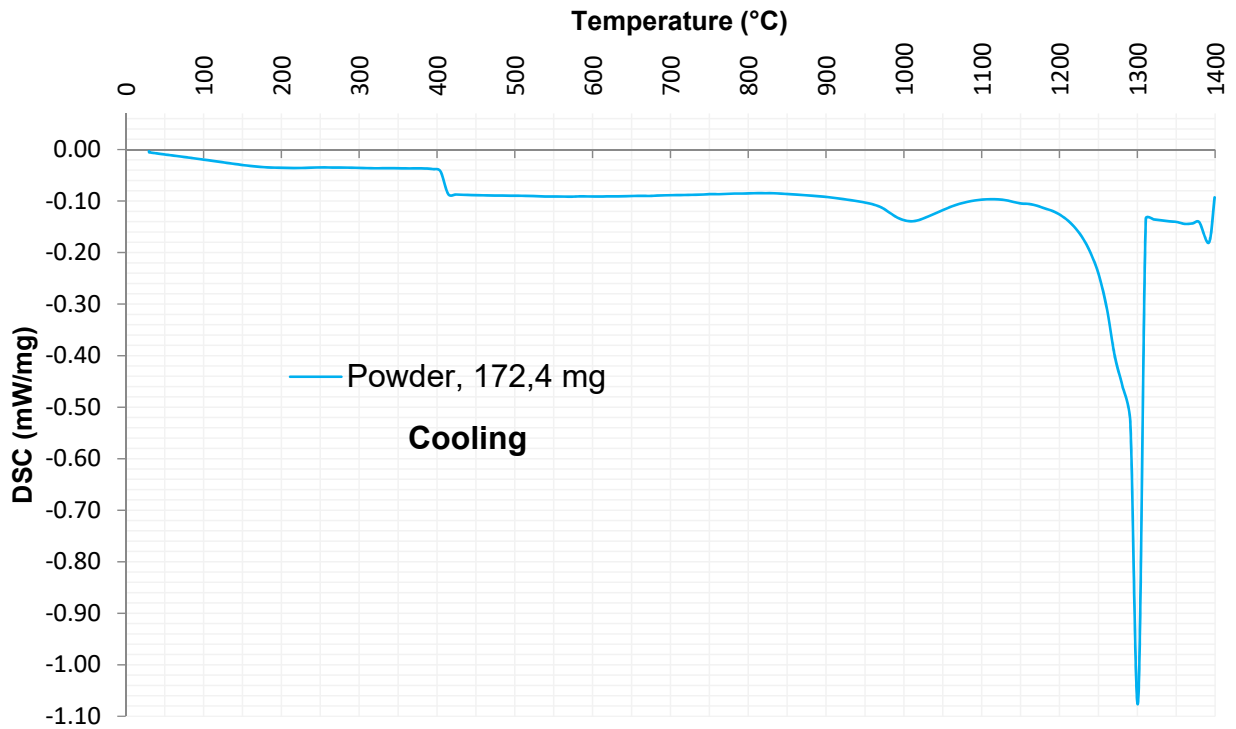


Figure A 2: DSC cooling graph of IN939 powder

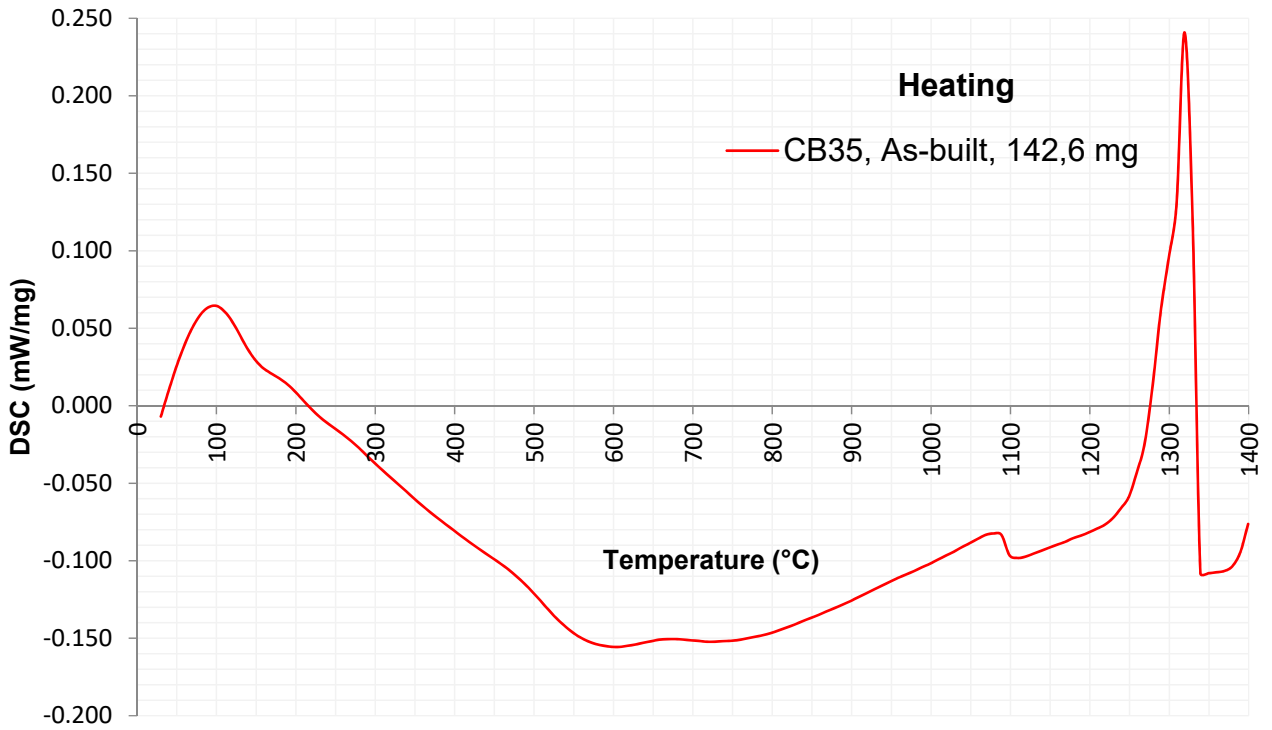


Figure A 3: DSC heating graph of As-Built IN939

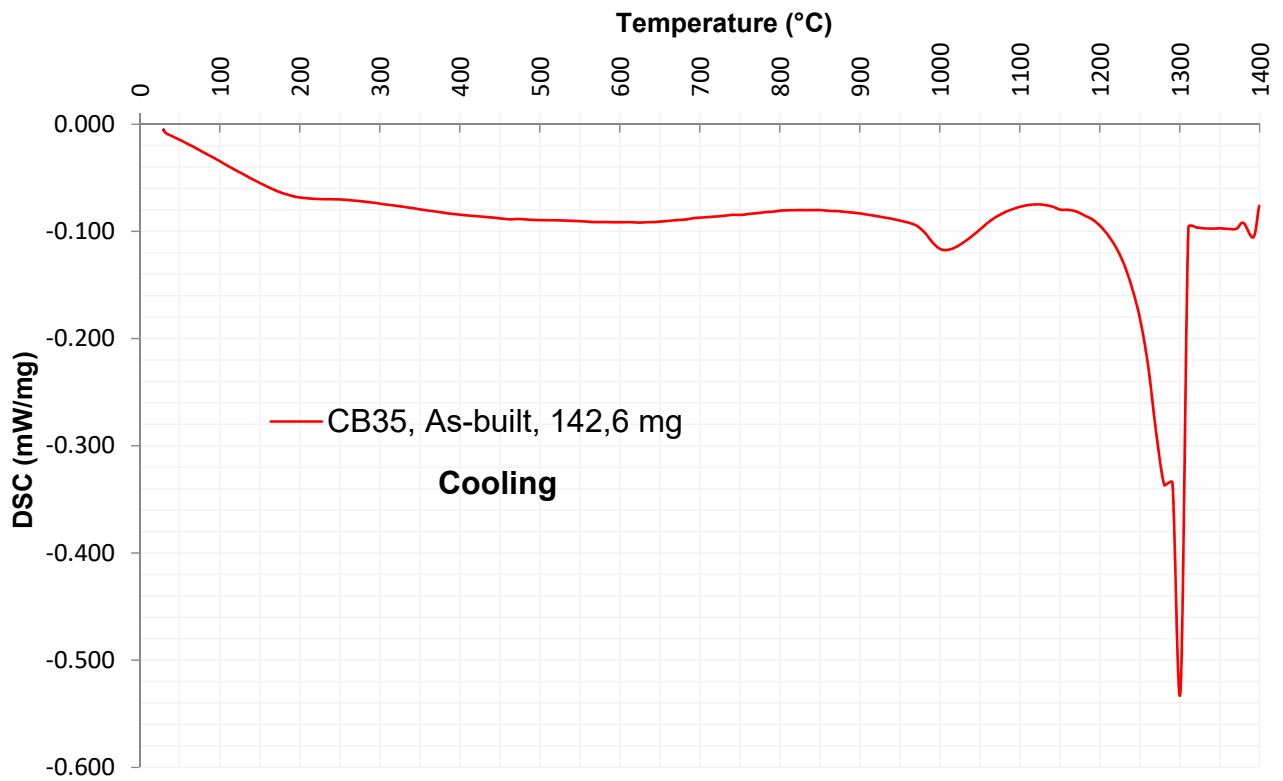


Figure A 4: DSC cooling graph of As-Built IN939

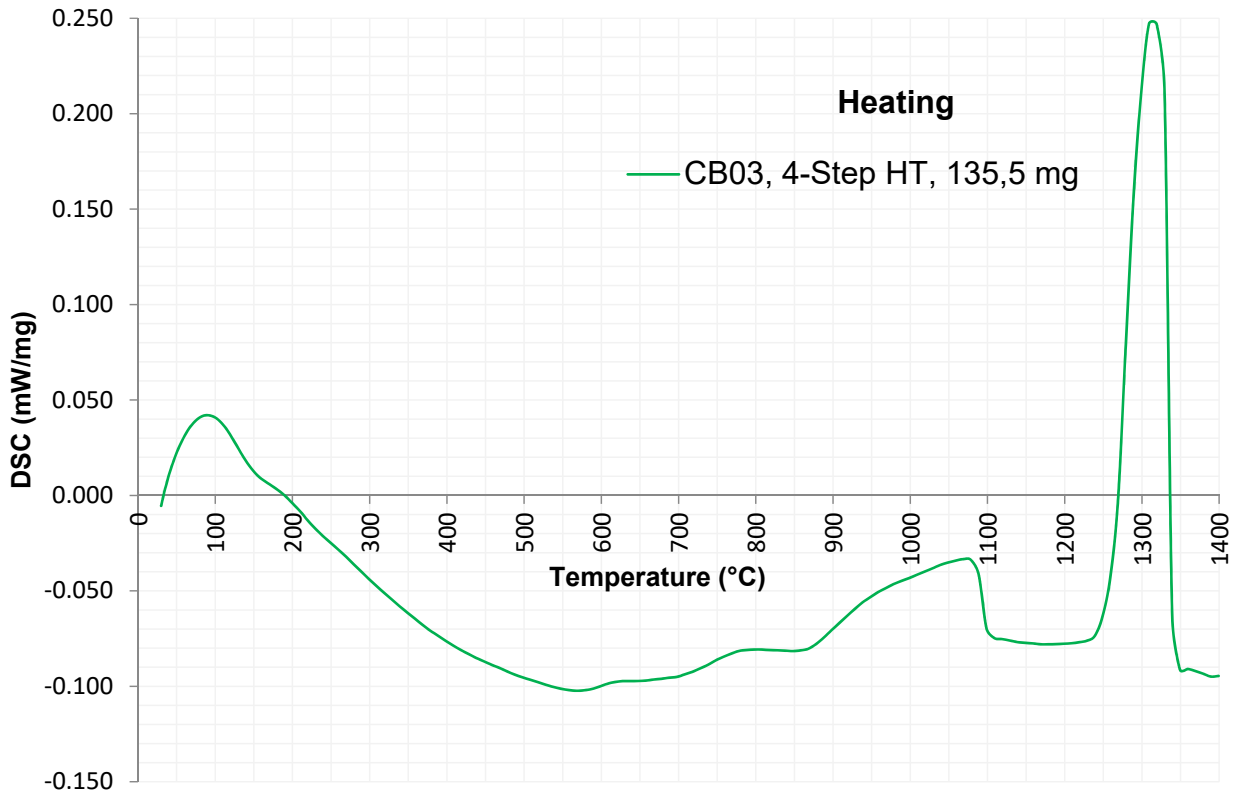


Figure A 5: DSC heating graph after HT-E

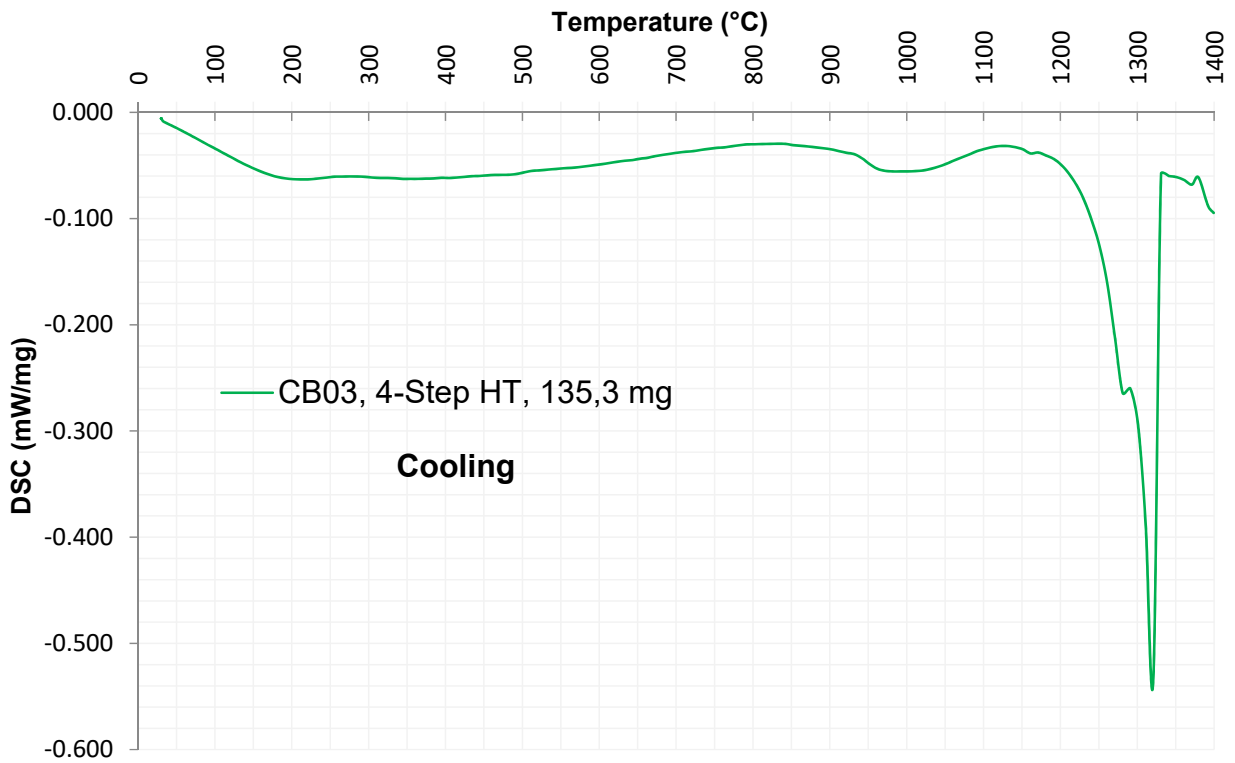


Figure A 6: DSC cooling graph after HT-E

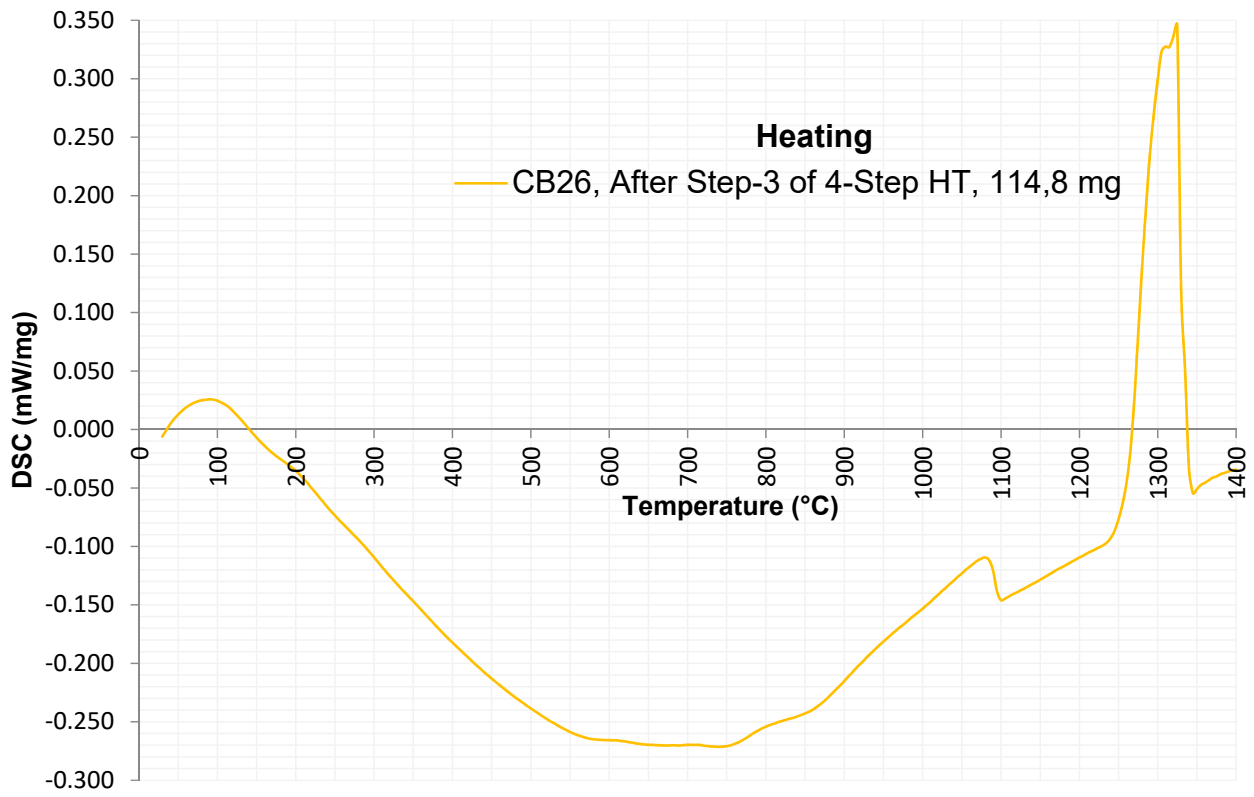


Figure A 7: DSC heating graph after HT-D

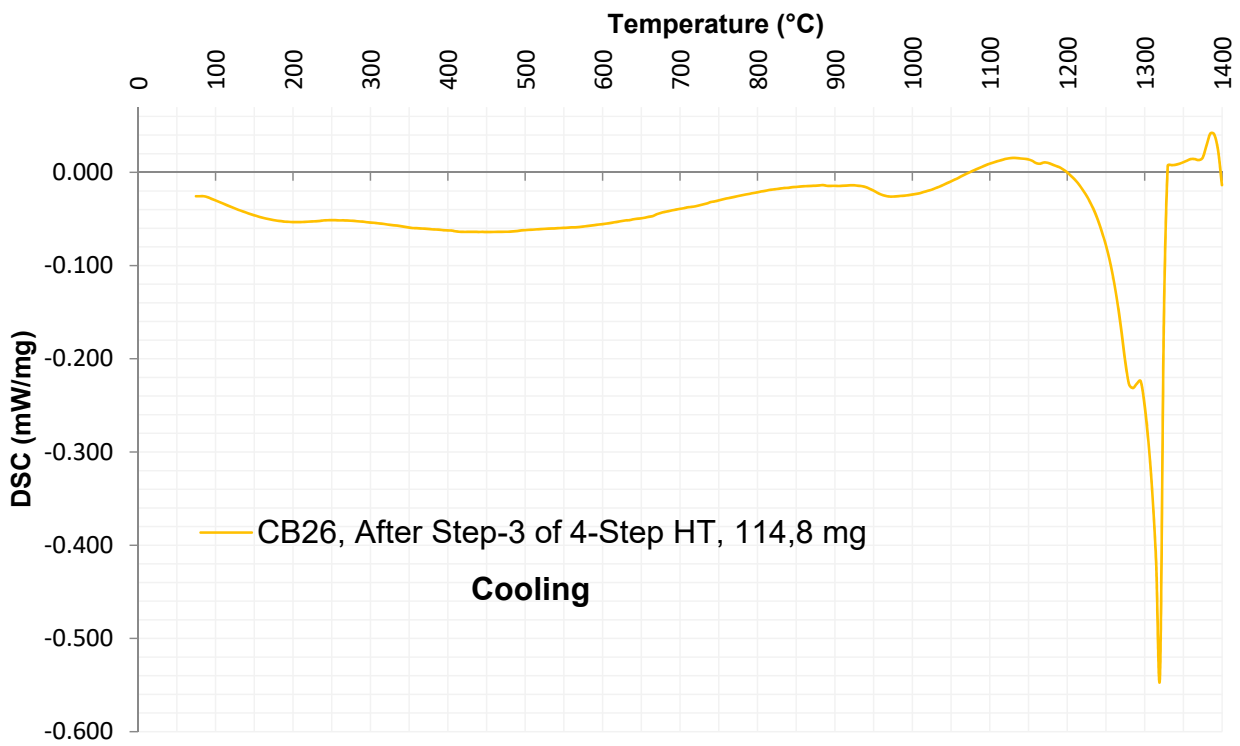


Figure A 8: DSC cooling graph after HT-D

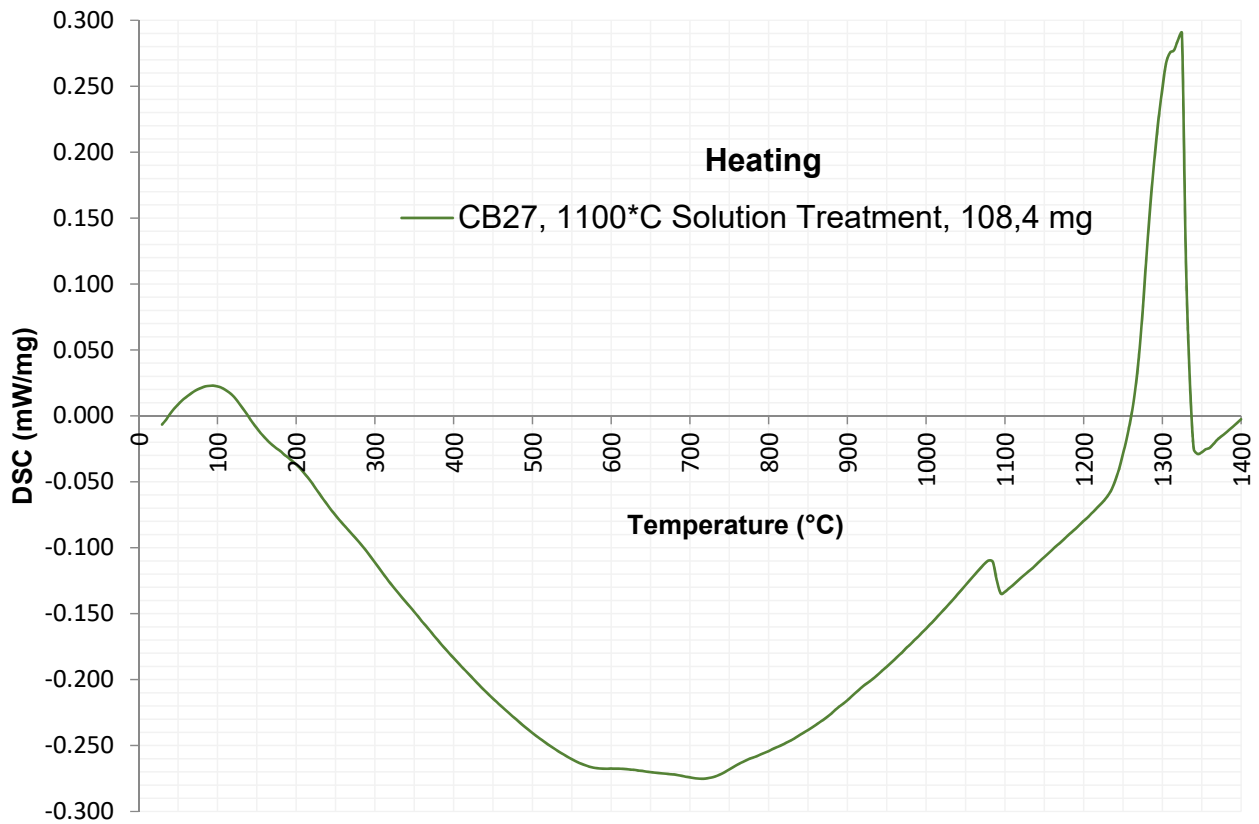


Figure A 9: DSC heating graph after HT-G

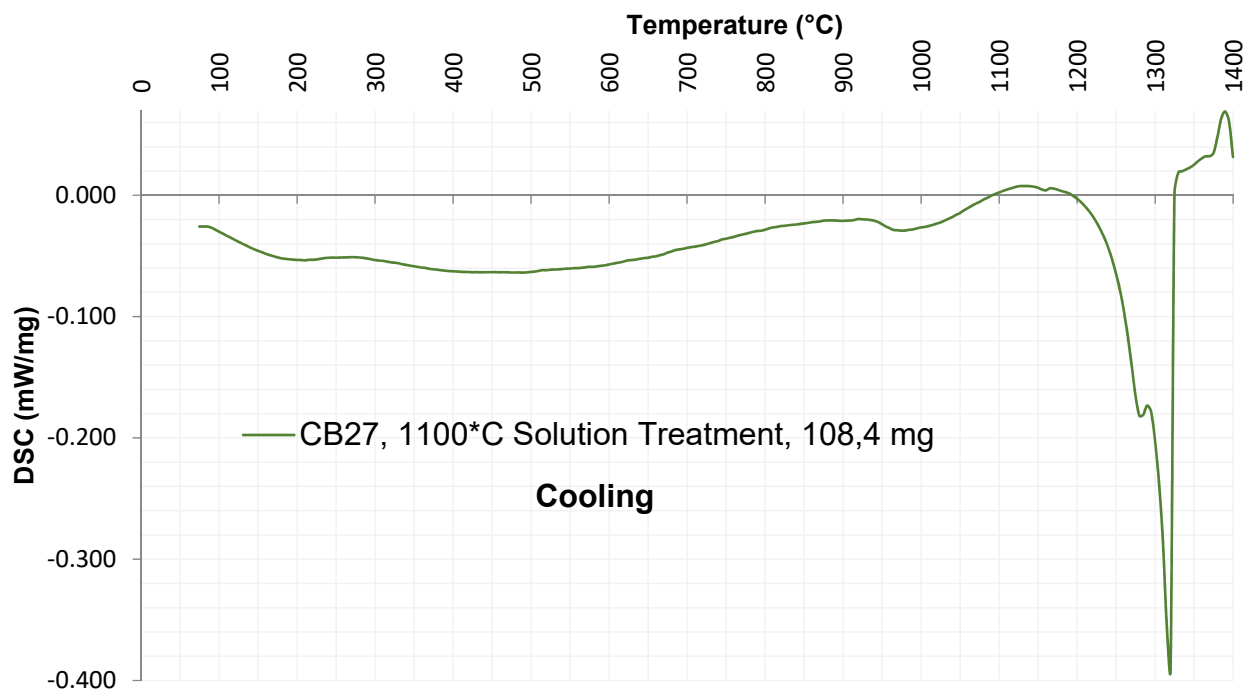


Figure A 10: DSC cooling graph after HT-G

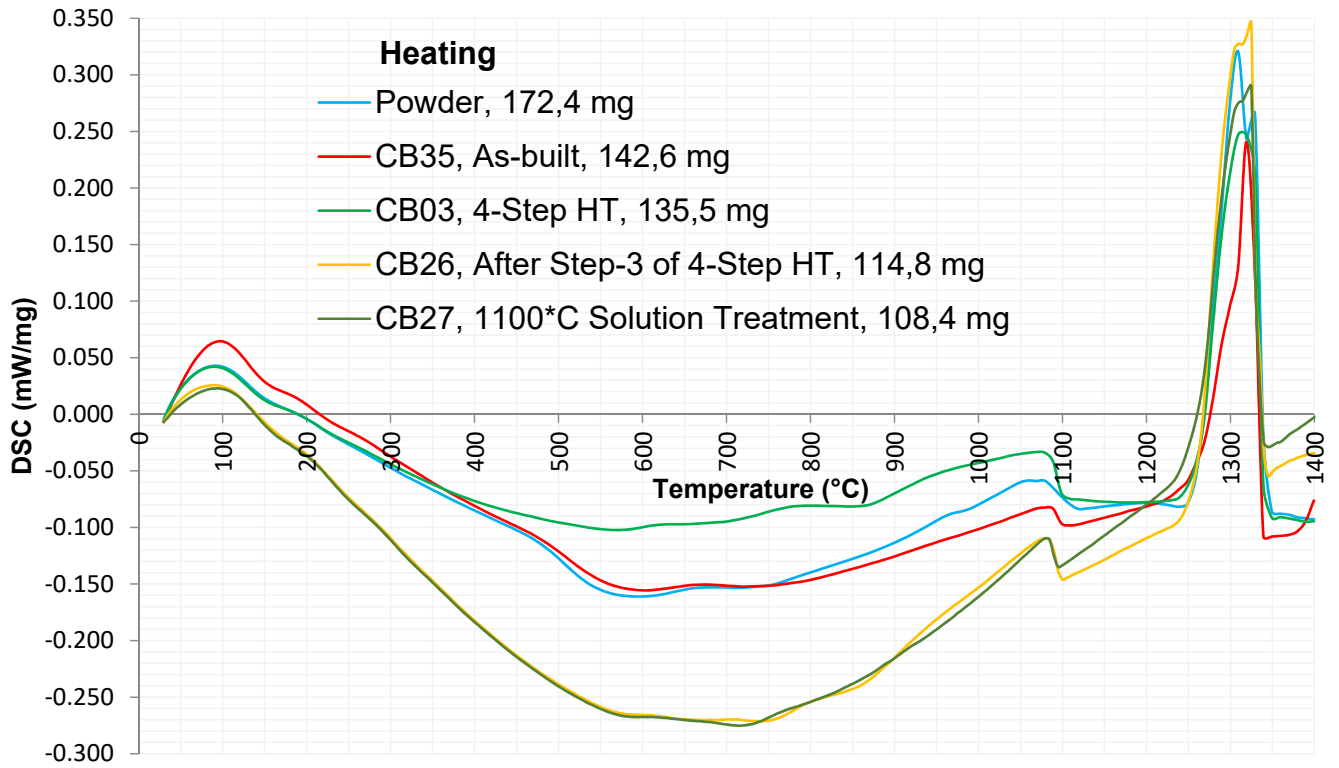


Figure A 11: Consolidated DSC heating graphs

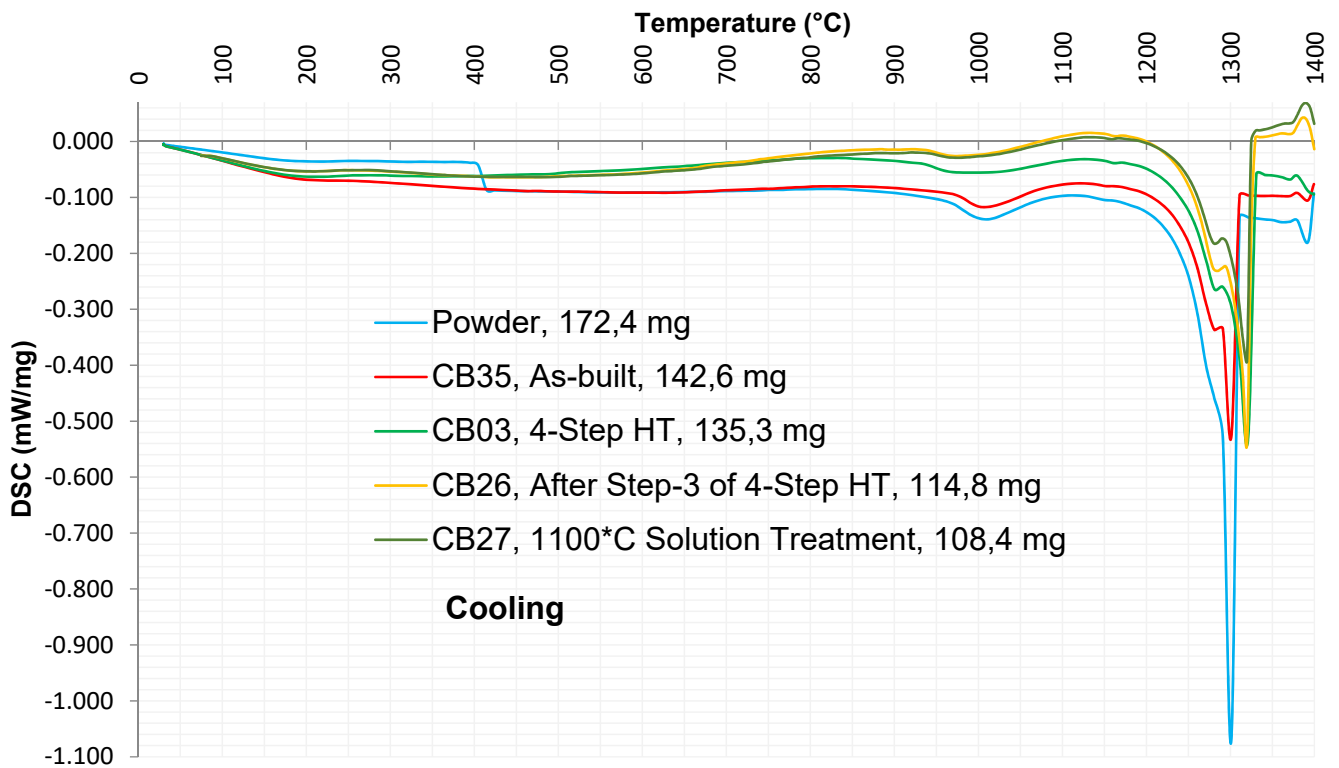


Figure A 12: Consolidated DSC cooling graphs

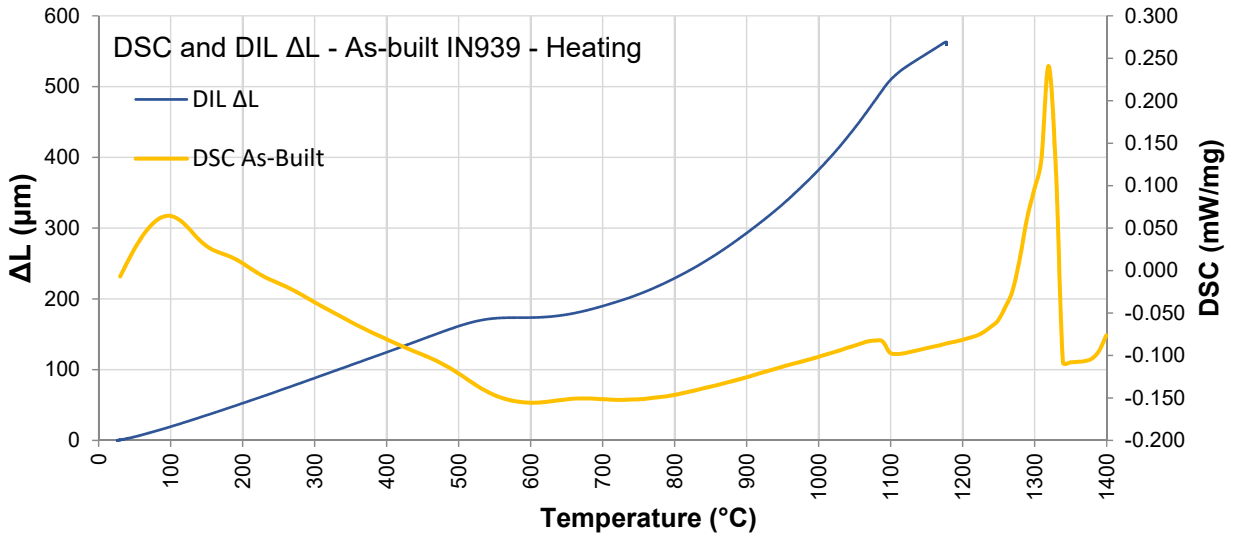


Figure A 13: DSC and DIL heating graphs of As-Built IN939

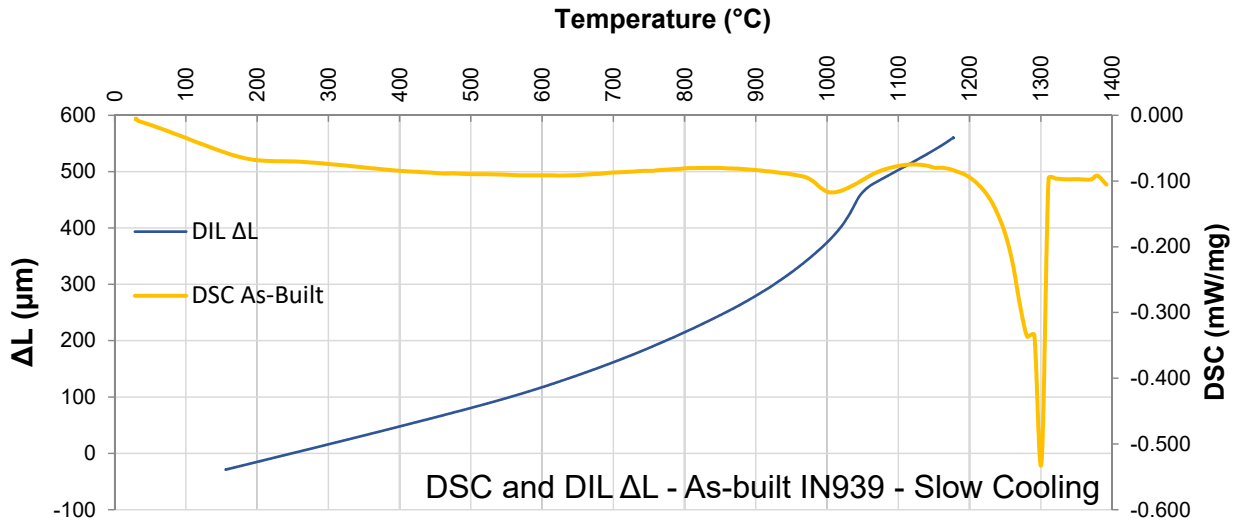


Figure A 14: DSC and DIL cooling graphs of As-Built IN939

9. Appendix 2 – Tensile Testing Results

Heat treatment	Ver / Hor	Sample ID	R _{p0,2}	R _m	Elongation, A	Reduction in Area, Z	
			MPa	MPa	%	%	
As built	A	Vertical	V01	707.8	1102	34.04	38
As built	A	Vertical	V14	752.5	1115.6	30.95	37
As built	A	Vertical	V21	736.3	1118.5	32.5	33
4/1160	B	Vertical	V02	1046.6	1428.4	19.39	23
4/1160	B	Vertical	V16	1103	1456.9	22.23	29
4/1160	B	Vertical	V24	1063.5	1455.4	18.88	20
4/1160+6/1000	C	Vertical	V03	995.4	1414.3	17.39	19
4/1160+6/1000	C	Vertical	V13	983.3	1420.7	18.92	23
4/1160+6/1000	C	Vertical	V20	978.4	1429.7	18.16	19
4/1160+6/1000+24/900	D	Vertical	V04	900.3	1392.8	15.02	18
4/1160+6/1000+24/900	D	Vertical	V15	904.9	1400.1	16.95	18
4/1160+6/1000+24/900	D	Vertical	V23	920.3	1414.5	16.07	25
4/1160+6/1000+24/900+16/700	E	Vertical	V05	1042.6	1486.9	9.25	15
4/1160+6/1000+24/900+16/700	E	Vertical	V10	1039.6	1501.7	10.55	10
4/1160+6/1000+24/900+16/700	E	Vertical	V22	1043.7	1508.5	10.24	10
4/1160+16/845	F	Vertical	V06	1146.7	1531.5	10.24	11
4/1160+16/845	F	Vertical	V17	1161.3	1531.5	12.45	18
4/1160+16/845	F	Vertical	V25	1186.8	1567	13.97	14
4/1100	G	Vertical	V07	1049.4	1423.5	23.16	28
4/1100	G	Vertical	V12	1047.1	1422.2	22.34	27
4/1100	G	Vertical	V18	1061.9	1439.3	24.94	30
4/1100+6/1000	H	Vertical	V08	904.8	1363.8	20.33	27
4/1100+6/1000	H	Vertical	V11	938	1388.9	21.3	36
4/1100+6/1000	H	Vertical	V19	937.4	1391.6	20.5	28
4/1160+6/1000+16/700	J	Vertical	V26	1108.6	1517.3	10.06	5
4/1160+6/1000+16/700	J	Vertical	V34	1092.6	1524.2	11.5	11
4/1160+6/1000+16/700	J	Vertical	V42	1109.5	1541	11.17	9
4/1100+6/1000+16/700	N	Vertical	V27	1126.4	1560.2	12.06	0
4/1100+6/1000+16/700	N	Vertical	V36	1130.1	1571.2	13.67	12
4/1100+6/1000+16/700	N	Vertical	V41	1136.3	1563.3	10.61	13
6/1000+16/700	P	Vertical	V28	1162	1524.1	8.21	-
6/1000+16/700	P	Vertical	V33	1160.6	1575.3	9.17	-
6/1000+16/700	P	Vertical	V39	1181.6	1562.1	8.64	-

Figure A 15: Tensile testing results: all vertical samples

Heat treatment	Ver / Hor	Sample ID	R _{p0,2}	R _m	Elongation, A	Reduction in Area, Z	
			MPa	MPa	%	%	
As built	A	Horizontal	TB01	819.6	1144.4	28.19	33
As built	A	Horizontal	TB06	793	1126.4	33.36	38
As built	A	Horizontal	TB26	793.7	1122	31.86	34
4/1160	B	Horizontal	TB14	1080.6	1464.4	13.42	18
4/1160	B	Horizontal	TB05	1083.8	1409	13.62	17
4/1160	B	Horizontal	TB27	1058.6	1398.6	13.83	15
4/1160+6/1000	C	Horizontal	TB04	1012.8	1423.8	12.89	16
4/1160+6/1000	C	Horizontal	TB11	1017.5	1434.6	13.33	16
4/1160+6/1000	C	Horizontal	TB21	1005.5	1374	15.71	17
4/1160+6/1000+24/900	D	Horizontal	TB07	949.1	1394.8	11.27	14
4/1160+6/1000+24/900	D	Horizontal	TB13	955.4	1426.8	11.94	14
4/1160+6/1000+24/900	D	Horizontal	TB17	952.9	1411.1	10.78	14
4/1160+6/1000+24/900+16/700	E	Horizontal	TB08	1089.1	1406.3	7.14	9
4/1160+6/1000+24/900+16/700	E	Horizontal	TB09	1062.2	1333.2	7.36	12
4/1160+6/1000+24/900+16/700	E	Horizontal	TB16	1073.7	1418.6	6.82	10
4/1160+16/845	F	Horizontal	TB10	1105.8	1408.9	7.66	12
4/1160+16/845	F	Horizontal	TB03	1210.3	1516	6.05	9
4/1160+16/845	F	Horizontal	TB12	1161.7	1510.6	6.57	10
4/1100	G	Horizontal	TB15	1077.3	1465.5	15.39	15
4/1100	G	Horizontal	TB24	1058	1442.4	14.26	15
4/1100	G	Horizontal	TB28	1065.2	1469.9	14.81	16
4/1100+6/1000	H	Horizontal	TB18	964.1	1392.1	13.86	14
4/1100+6/1000	H	Horizontal	TB20	959.9	1339.4	14.52	19
4/1100+6/1000	H	Horizontal	TB23	961.6	1388.7	15.73	21
4/1160+6/1000+16/700	J	Horizontal	TB22	1145.8	1372.4	5.61	9
4/1160+6/1000+16/700	J	Horizontal	TB30	1150.8	1448.3	6.39	5
4/1160+6/1000+16/700	J	Horizontal	TB36	1146.3	1427.4	6.42	10
4/1100+6/1000+16/700	N	Horizontal	TB29	1192.4	1267.9	1.07	7
4/1100+6/1000+16/700	N	Horizontal	TB33	1206.4	1502.1	7.21	10
4/1100+6/1000+16/700	N	Horizontal	TB38	1203.1	1492.5	7.62	9
6/1000+16/700	P	Horizontal	TB32	1220.6	1463.9	5.53	8
6/1000+16/700	P	Horizontal	TB40	1207	1394.8	3.74	8
6/1000+16/700	P	Horizontal	TB40	1218	1514.6	6.52	8

Figure A 16: Tensile testing results: all horizontal samples